DISS. ETH No. 13625

# Design and Control of Sensor-Guided Nanorobots

Dissertation submitted to the
SWISS FEDERAL INSTITUTE OF TECHNOLOGY
ZURICH

for the degree of
Doctor of Technical Sciences

presented by
Markus Brunner
Dipl. Masch.-Ing. ETH
born February 22, 1971
citizen of Laupersdorf, Switzerland

accepted on recommendation of
Prof. Dr. A. Stemmer, examiner
Prof. Dr. H. Bleuler, co-examiner

Zurich, 2000

# *Acknowledgements*

This thesis is a result of my research in the Nanotechnology Group at the Institute of Robotics. It is part of the poly project NANO II that started in fall 1997 at the Swiss Federal Institute of Technology (ETH) in Zurich. During the three years of participating in this project, I have been supported by various people.

First of all I would like to thank my thesis advisor Prof. Dr. Andreas Stemmer for giving me the opportunity to work at the very front of current nanotechnological research. As director of the poly project NANO II he managed to create an inspiring multidisciplinary environment in which new ideas could thrive based on the knowledge of different fields like physics, biology, chemistry or engineering.

Very much appreciation is due towards Prof. Dr. Hannes Bleuler for taking over the co-advisor part of my thesis and for the critical remarks and important suggestions on this manuscript.

During design and construction I was glad to rely on the technical knowledge of Helmut Knapp for questions concerning SPM measurement techniques and video microscopy. I wish to thank him for this assistance and his highly esteemed help in the careful correction of my terrible English.

I appreciated the technical advice and the active help of Serge Müller very much during manufacture of the electronic components. Thanks to his talent and this knowledge of tricks and knacks I got a excellent setup to work with.

I would like to thank Daniel Bächi for the fruitful discussions and his promoting remarks on this thesis. He provided me with lots of micro fabricated samples and also with professional advice in cases I didn't see a solution to the problem. Furthermore, I appreciate the support from Dr. Otte Homan by supplying me with transistor structures as well as test specimen.

The members of the Nanotechnology Group have shared with me the joys and struggles of post graduated life at the ETH. Each of the following has contributed directly to my research: Guy Birrer, Brian Cahill, Jan Frohn, Daniel Häfliger, Heiko Jacobs, Patrick Mesquida, Sao-Jü Woo. They always had the right answers to my questions. I appreciated this very much.

I am very grateful to J. Böhi, M. Vogt, A. Weber and E. Randak for fabricating the necessary components for my setup. They always found a way to manufacture the tiny parts for me.

I owe much to Roland Büchi and Wolfgang Zesch who shared their experience with me and encouraged me to work on my Ph.D.

Thanks also to all the members of the Institute of Robotics and the students who helped me throughout the realization of this thesis. They gave me the feeling of what a Ph.D. study in a stimulating and amicable atmosphere might be.

Last, but not least, I would like to thank my parents Oswald and Seline Brunner as well as my sisters for their love, encouragement and support in everything I have ever done. They always had the right words to set me up when I was struggling with minor or major problems.

Markus Brunner

Zurich, Mai 2000

# *Table of Contents*

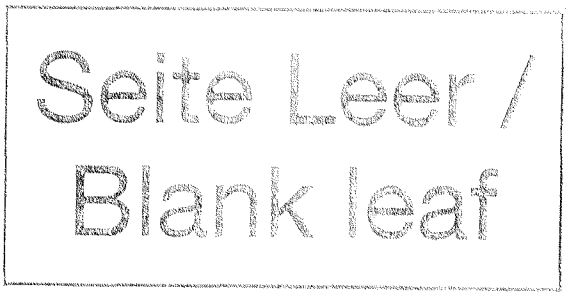
Seite Leer /
Blank leaf

# *Abstract*

Today, many research and development areas experience a tremendous growth due to the use of micro- and nanotechnology. Fields like design of integrated circuits, biology or medicine benefit from technological achievements and methods from micro technique. Current research fields also gain profound knowledge applying new visualization tools that allow a closer look in the nano world. Together with these new methods for analysis a strong demand to enter not only passively but actively in the (sub)micrometer regime is heard. Hence, new ways for manipulation of micro particles are required to form the nano world according to the needs of the application just in hand.

Although nanotechnology offers a lot of possible solutions and methods for a given application, their usage is sometimes rather complicated and needs detailed knowledge. Taking this into account, this thesis starts by picking up known concepts from nanotechnology, robotics and signal processing and bringing them together in a new concept. The presented sensor-guided nanorobot shows a possibility to combine information from the micro and macro world with a-priori knowledge from the user to perform a given task automatically. This task-oriented working principle offers an easier operation and a faster and more flexible data acquisition. This is the first step towards systems that can be integrated in a fully automated environment to work on the small scale.

The presented prototype was designed for the analysis of integrated circuits. For their optimization, data about e.g. the quality of the circuit path or the strength of the electric field along a transistor are required. The sensor-guided nanorobot can acquire such information automatically by letting the user define the properties of the structure under investigation, e.g. its width or the electric potential as well as the approximate point for starting the analysis. After that, the system searches for the exact position of the structure of interest and tracks along it. For this purpose the system uses a tip that is also applied in an atomic force microscope to gather local information like topography or surface potential. These signals contain information about the structure. A control loop processes this information in real-time and decides afterwards where to go next.

Due to the fact that signals from the nano world are sensitive and often noisy compared to information from the macro world, the already found positions of the structure are stored and interpolated to a trajectory. Hence, the control loop gets more stability by considering not only the actual data, but also the past path trajectory. Further, a video camera is used as additional sensor to guide the local probe at critical points like bendings or junctions, at which local information alone often is not sufficient.

The presented concept can be easily expanded and adapted to other applications due to the modular setup. Another field could be e.g. the automatic search of micro objects and their picking afterwards. To do this, a new generation of micro manipulators is presented. The gripper is based on a glass pipette to manipulate objects with sizes >10 µm. An integrated distance sensor allows one to measure the actual spacing between tool tip and environment. With such intelligent tools on the one hand local properties of the sample can be acquired and on the other hand manipulations can be performed, too. Complemented with the presented concept of a sensor-guided nanorobot, this is the first step towards robots that can build up micro structures automatically.

# *Kurzfassung*

Viele Forschungs- und Entwicklungsgebiete erfahren heute durch den Einsatz von Mikro- und Nanotechnologie einen starken Aufschwung. So profitieren z. B. Gebiete wie Schaltungsdesign, Biologie oder Medizin heute von Errungenschaften und Verfahren aus der Mikrotechnik. Auch aktuelle Forschungsgebiete erzielen vertiefte Erkenntnisse durch den Einsatz von neuen Visualisierungswerkzeugen, die den Blick in die Nanowelt ermöglichen. Mit den neuen Analysemöglichkeiten wird auch der Wunsch immer stärker, nicht nur passiv sondern auch aktiv in das Submikrometer Regime einzudringen. Neue Wege für die Manipulation von kleinen Partikel werden gesucht um die Nanowelt nach den Bedürfnissen der gerade vorliegenden Anwendung zu gestalten.

Obwohl die Nanotechnolgie für viele Anwendungen mögliche Lösungen und Methoden zur Verfügung stellt, sind deren Einsatz mitunter noch recht umständlich und benötigen grosses Fachwissen. Hier setzt diese Arbeit an, indem sie bestehende Verfahren aus Nanotechnik, Robotik und Signalverarbeitung aufgreift und sie in einem neuen Konzept zusammenführt. Der vorgestellte sensorgeführte Nanoroboter zeigt eine Möglichkeit, Informationen aus der Mikro- und Makrowelt mit Benutzervorwissen zu kombinieren, um eine gestellte Aufgabe automatisch auszuführen. Dieses aufgabenorientierte Funktionsprinzip ermöglicht eine einfachere Bedienung und eine schnellere und flexiblere Datenerfassung. Dies ist ein erster Schritt in Richtung von Systemen, die integriert in eine vollautomatische Umgebung auf dieser kleinen Grössenskala arbeiten können.

Der präsentierte Prototyp wurde auf die Analyse von integrierten Schaltungen ausgerichtet. Für deren Optimierung werden z. B. Daten über die Qualität von Leiterbahnen oder die elektrische Feldstärke entlang von Transistoren benötigt. Der sensorgeführte Nanoroboter kann solche Informationen automatisch erfassen, indem er den Benutzer über die Eigenschaften wie z. B. Breite oder elektrisches Potential der zu untersuchenden Struktur sowie den ungefähren Startpunkt der Analyse befragt. Danach sucht er automatisch die genaue Position der gewünschten Struktur und tastet sich ihr entlang. Hierzu verwendet das System eine Spitze, wie sie auch in Rasterkraftmikroskopen eingesetzt wird, um lokale Informationen, im vorliegenden Fall Topographie und Oberflächenpotential, zu messen. Diese Signale beinhalten Anhaltspunkte über die Struktur. Ein Regelkreis wertet diese Informationen in Echtzeit aus und entscheidet dann über das weitere Fortschreiten.

Da Signale aus der Nanowelt verglichen zu Informationen aus der Makrowelt sehr störanfällig und oft mit Rauschen behaftet sind, werden die bereits gefundenen Positionen der Struktur gespeichert und zu einer Trajektorie interpoliert. Der Regelkreis wird somit stabiler, da er nicht nur die aktuellen Daten zur Entscheidungsfindung verwenden muss, sondern auch auf den früheren Verlauf der Leiterbahn zurückgreifen kann. Ferner wird eine Videokamera als weiterer Sensor verwendet um die Messsonde an kritischen Stellen wie Knicke oder Verzweigungen, an denen lokale Informationen alleine oft nicht ausreichen, sicher weiterzuführen.

Das vorgestellte Konzept kann dank des modularen Aufbaues leicht auf andere Aufgabenstellungen erweitert und angepasst werden. Eine weitere Anwendung könnte z. B. das automatische Finden von Mikroobjekten und das anschliessende Greifen sein. Hierzu wird eine neue Generation von Mikromanipulator vorgestellt. Der Greifer basiert auf einer Glaspipette um Objekte ab einer Grösse von 10 µm zu manipulieren. Ein integrierter Distanzsensor erlaubt das Messen des aktuellen Abstandes zwischen Werkzeugspitze und Umgebung. Mit solchen intelligenten Werkzeugen kann sowohl auf lokale Probeneigenschaften zugegriffen werden als auch Manipulationen vorgenommen werden. Kombiniert mit dem vorgestellten Konzept des sensorgeführten Nanoroboters ist dies ein erster Schritt in Richtung von Robotern, die automatisch Mikrostrukturen zusammenbauen können.

# *Abbreviations*

| | |
|---|---|
| 2D | Two-Dimensional |
| 3D | Three-Dimensional |
| AC | Alternating Current |
| AD | Analog-Digital (e.g. AD-converter) |
| AFM | Atomic Force Microscope |
| AO | Analog Output |
| CCD | Charge-Coupled Device |
| CD | Compact Disk |
| CPU | Central Processing Unit |
| DA | Digital-Analog (e.g. DA-converter) |
| DC | Direct Current |
| DIO | Digital Input/Output |
| DO | Digital Output |
| DOF | Degree of Freedom |
| DSP | Digital Signal Processor |

| | |
|---|---|
| GUI | Graphical User Interface |
| HEMT | High Electron Mobility Transistor |
| HF | High Frequency |
| HFP | Hexafluoropropene |
| HV | High Voltage |
| IC | Integrated Circuit |
| IO | Input/Output |
| ISA | Industry Standard Architecture (PC bus architecture) |
| MUX | Multiplexer |
| NA | Numerical Aperture |
| PC | Personal Computer |
| PCI | Peripheral Components Interface (PC bus architecture) |
| PE-CVD | Plasma Enhanced Chemical Vapor Deposition |
| PI | Proportional-Integral (e.g. PI-controller) |
| PIB | Polyisobutylene |
| RMS | Root Mean Square |
| SNOM | Scanning Near-Field Optical Microscope |
| STM | Scanning Tunneling Microscope |
| SPM | Scanning Probe Microscope |
| WD | Working Distance |

# 1 Introduction

Today's technological development is inspired by the spirit of Richard Feynman whose vision of a new world at the bottom of our length scale [Feynman59] founded a whole new science discipline. Nanotechnology tries to reach out for the small world of molecules and atoms to visualize them, interact with them and even manipulate them. The reason to do this is clear: with a minimum of energy and material functional structures should be built that will improve our life, e.g. small implants that will support blood circulation of cardiac patients or dispense vital drugs over a long period of time. Whereas micro technology with its silicon-based methods can supply us with functional devices, new tools are required to assemble the micro fabricated parts and to investigate the structures to guarantee performance and reliability. Hence, systems are needed that can measure information on the nanometer scale and can operate in the nano world.

## 1.1 Development of Tools for the Nano World

In our macro world, numerous tools are able to manipulate objects. Without doubt, our hand is the most widely used tool for handling a variety of things. Robot systems try to imitate this powerful tool to perform automated tasks. Approaching the nano scale, one could think of miniaturizing such manipulators to get useful tools for the micro world. This top-down strategy (fig. 1.1) has been

followed resulting in various principles for micro manipulation [Greitmann96, Koyano96, Arai97, Miyazaki97, Salim97, Arai98, Kasaya98, Kim99] (see section 2.1). Reaching object sizes of 100 µm and below we get into the regime of dominating adhesive effects. This leads to the fact that methods that use direct contact to manipulate particles will have problems mainly in releasing the object. These difficulties can be overcome by using non-contact techniques e.g. electrophoretic forces [Mosher92], dielectrophoretic forces [Pohl78], optical traps [Ashkin86, Block92] etc. A different approach originates from chemistry and biology which apply a bottom-up strategy to assemble atoms to molecules and built up functional micro and nano structures.

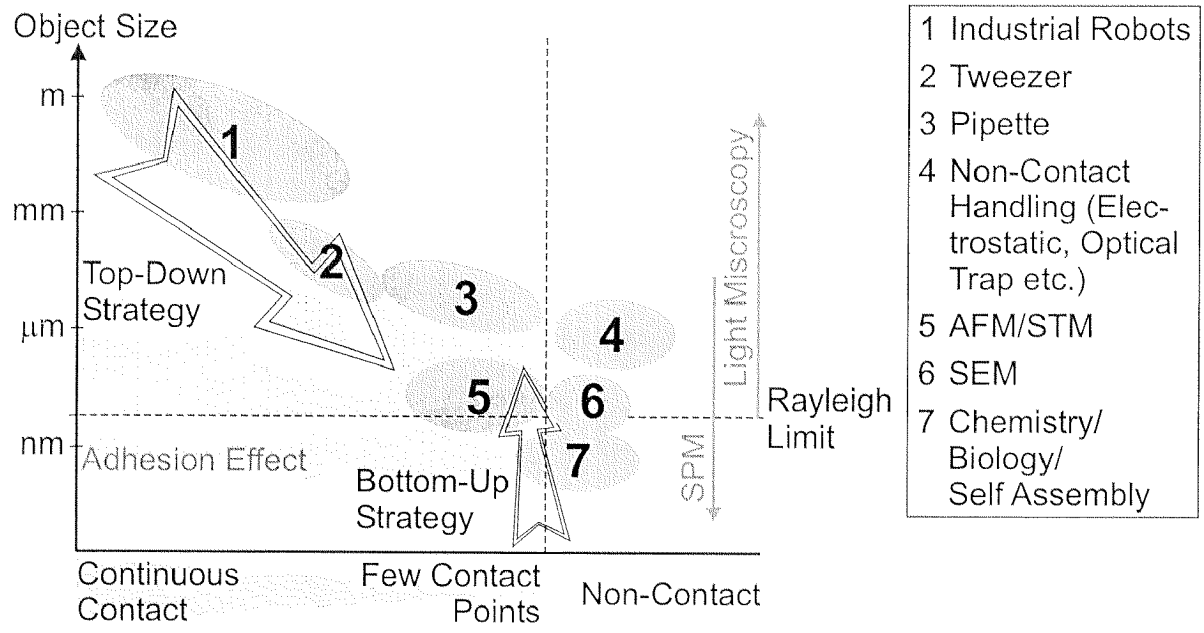


**Fig. 1.1:** *Development of tools working in the micro and nano world*

Besides the manipulation of objects, the visualization of (sub)micro structures is another major problem [Stemmer96]. Whereas light microscopes are well suited for object sizes typically above 200 nm, the Rayleigh limit makes their applicability difficult to particle dimensions below (fig. 1.1). Near-field microscopes like atomic force microscopes (AFM) [Binnig86] or scanning tunneling microscopes (STM) [Binnig82] can overcome this limitation and offer even subnanometer resolution. Furthermore, these systems have also proved themselves as powerful tools to manipulate nano particles (see section 6.2).

Comparing the automatization level of systems working in the macro and micro world (fig. 1.2), it is obvious that engineers developed industrial robots by combining sensing and actuating units with intelligent control strategies. They even made a step further by making these systems autonomous. In contrast to this, the micro manipulators and visualizations tools invented so far for the nano world are still systems with a low level of automatization. As a conclusion it clearly can be seen that the sensors and actuators for the (sub)micro world have to be united with a refined automatization strategy optimized for robots working in the nano world. Such entities, called nanorobots, will work at a highly automated level.

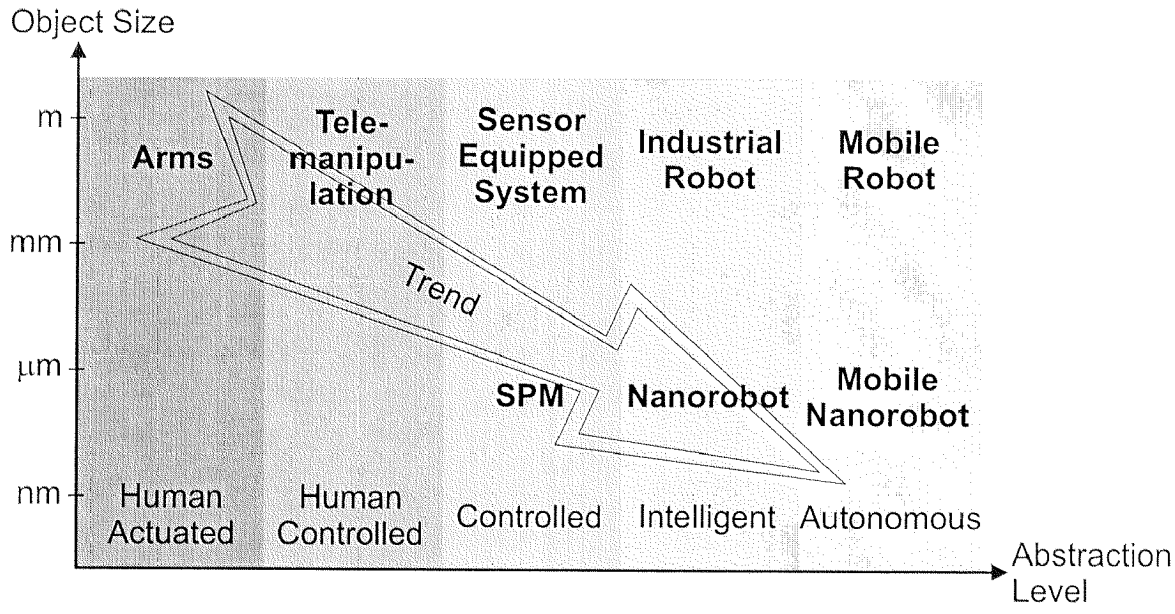


**Fig. 1.2:** *Development of automated systems in the macro and micro world*

## 1.2 Scope of This Thesis

The objective of this thesis is the development of new control strategies and behavior rules for systems working in the nano world. New ideas of how to process near-field sensor information to perform given tasks automatically will be discussed. Hence, a higher level of automation can be achieved that allows us to define tasks that will be executed automatically by the robot. Due to the small point of access to the nano world, such systems have to be equipped with a new generation of micro tools that combine sensing and actuating skills to gain full access to local properties.

Whereas sensors and actuators with nm resolution are available from current scanning probe microscope (SPM) technologies, the idea of autonomous nanorobots [Drexler91], i.e. small systems with their own energy supply, controllers, sensing and actuating units, is not feasible because of the size of current micro processors [Nicoud95]. Therefore, the domain of nanorobotics deals more with the design of systems working in the nano world [Requicha99] and their applications and not with systems with an overall size in the µm range. Consequently, the term *sensor-guided nanorobot* does not describe a system with overall dimensions in the (sub)micro range but a setup that is working on the nm scale by combining suitable sensors and actuators with control strategies to perform automated tasks. The dimensions of such a sensor-guided nanorobot can still be in the macro regime, whereas the resolution of the system is on the atomic scale.

This thesis is part of the NANO II project in which high electron mobility transistors (HEMTs) are developed that will operate at high frequencies. In this application knowledge of the topography and surface potential along the gate finger of the transistor is extremely important to calculate the electric field. These data are used for optimization of the transistor structure. To support this optimization and to show an example of a nanorobot's abilities, the idea of tracking along nano structures [Pohl88] is elaborated to an new working principle. The algorithm allows the operator to define the feature of interest based on his a-priori knowledge and then starts the flexible data acquisition by automatically guiding the local sensor (e.g. an SPM probe) along the feature trajectory. The advantage of such a working principle is, firstly, the fact that only the necessary data are measured and hence data acquisition is speeded up and, secondly, that the system can be automated. A task-oriented working principle can be achieved in which the user is defining a task that the robot automatically performs. This leads to a robot system that operates on a higher level of automatization.

## 1.3 Thesis Outline

In chapter 2, first the working principles of intelligent micro tools are described and a possible realization is presented. We carry on the field of micro particle manipulation and introduce a glass pipette based micro manipulator. The tool is optimized for proper picking and placing of micro objects. An integrated distance sensor allows us to measure the tip-sample separation, which is the first step to

integrate the tool in a robot environment capable of automatically executing user-defined tasks.

In chapter 3, a platform is introduced on which the tasks can be implemented and tested. Because of the multifunctional characteristics of many SPM probes (e.g. an AFM tip can measure topography, surface potential, magnetization, elasticity of the material, etc.) the experimental setup is designed to handle multiple sensor inputs. In order to examine the controller strategies a benchmark test different from micro particle manipulation is needed. Consequently, we work on integrated circuit structures that reveal a variety of possible tasks the sensor-guided nanorobot can perform (e.g. damage analysis of a gate finger, electric field analysis of a transistor, etc.). Due to the rapidly-changing requirements of such an experimental platform, e.g. another application field of the controller strategies is automated micro-object handling, we put special emphasis on a modular concept. This enables us to apply not only SPM probes but also the intelligent micro manipulator in the setup.

In chapter 4, a controller setup is discussed and implemented on the test platform to show how a user-defined task is processed by the robot system. First, the general working principle is presented and afterwards an example is shown to give detailed information about the calculation steps the robot has to perform.

In chapter 5, benchmark tests of the implemented algorithms are shown to demonstrate the nanorobot's abilities and to give an idea of the capabilities of such systems. On the one hand, system stability against short-time break-downs of sensor signals is proved and on the other hand tracking along test structures based on local (e.g. from an SPM probe) as well as global information (e.g. from a light microscope) is demonstrated. Finally, the current implementation is employed on transistor structures.

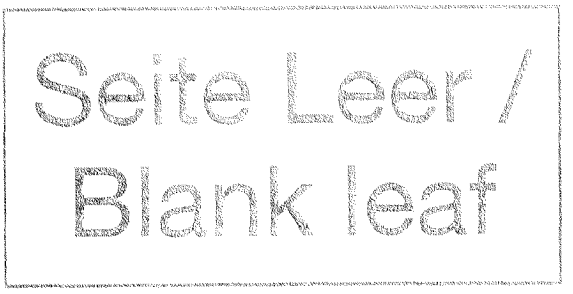
Seite Leer /
Blank leaf

# 2 New Tools with Integrated Sensors and Actuators

In this chapter the working principles of intelligent tools that combine sensing and actuating functions in one unit will be elaborated and a possible implementation will be introduced. The micro manipulator is capable of handling micro objects sized between 40 µm up to 200 µm and can sense the distance to the object which is necessary to realize collision avoidance control loops. This integrated local sensor allows one to implement manipulation tasks in a fully automated environment. It is a first step towards intelligent systems working in the micro and nano world (fig. 1.2).

## 2.1 Overview of Micro Object Manipulation

*Elementary Tasks*

Micro particle manipulation summarizes a sequence of elementary tasks. First, the particle is *picked* up in order to be *moved* to another location. There, the object has to be *placed* at the desired position, e.g. in order to build up microstructures. If such a pick and place operation is not successful the particle has to be *removed* to allow the tool to pick up the next object.

*Overview of Possible Manipulation Techniques*

Various approaches for micro particle handling have been investigated in the last years. To get an overview they will be split up in three major categories. The first class uses two or more fingers to grasp an object. With such a *tweezer-like mechanism*, mostly fabricated with silicon technology, the particles are gripped with the fingers of the tool [Greitmann96, Arai97, Salim97, Arai98, Kim99]. The second class of micro manipulators need only one single finger to pick a particle. With the use of adhesive effects [Koyano96, Miyazaki97, Kasaya98], vacuum [Zesch97a] etc. these *needle-like mechanisms* try to change the force acting between the finger and the particle with suitable handling procedures. The last category applies *non-contact methods* such as electrophoretic forces [Mosher92], dielectrophoretic forces [Pohl78], laser beams [Ashkin86, Block92], aerodynamic effects [Segovia98], etc. to interact with the object without touching it.

Comparing the above mentioned categories one can clearly see that the tweezer-like methods benefit from being able to grip particles of a large range of object sizes. The major disadvantage is the difficulty of releasing the object (see section 2.2). This problem of releasing an object is not existent with non-contact methods because switching off the power will instantaneously free the particle. The usage of such techniques is restricted to small object sizes because larger object dimensions necessitate high power densities that might damage the particle. A good compromise between these two classes of manipulation methods is the needle-like category that affords control over the contact forces and, therefore, improve the release of particles while not being restricted to small object sizes.

## 2.2 Comparison of Relevant Forces

In order to see the differences between macro and micro object handling, we take a closer look at the forces acting on the object. In detail, the surface forces [Israelachvili92] that originate from electrostatic and intermolecular interactions as well as from the condensation of liquids on the surface and gravitation are compared [Arai95, Fearing95] by using a simplified model of a sphere interacting with a plane.

*Gravitation*

Eq. 2.1 describes the gravitation force $F_G$ acting on a sphere with radius $R$ and density $\rho$, where $g$ denotes the acceleration of gravity.

$$F_G = \frac{4}{3}\pi R^3 \rho g \tag{2.1}$$

*Electrostatic Interactions*

The Coulomb force $F_C$ can be written according to eq. 2.2 with $\varepsilon_0$ denoting the permittivity of vacuum, $\varepsilon$ the dielectric constant of the material and $z$ the distance between the sphere and the plane. The voltage $U$ between sphere and plane depends on the charge, the work function of the materials and the possibly applied voltage and can vary strongly between dry and humid conditions.

$$F_C(z) = \pi R \varepsilon \varepsilon_0 \frac{U^2}{z} \tag{2.2}$$

*Intermolecular Interactions*

The Van-der-Waals force (eq. 2.3) is a function of the material-dependent Hamaker constant $H$ which includes dispersion forces, orientation effects between permanent dipole as well as interactions due to induced dipole between permanent dipoles and non-polar molecules [Israelachvili92].

$$F_{vdw}(z) = \frac{HR}{6z^2} \tag{2.3}$$

*Forces due to Capillary Condensation*

Forces resulting from capillary condensation $F_W$ (eq. 2.4) [Israelachvili92] can occur mainly in humid environments. These interactions depend on the surface tension $\gamma$ and the contact angle $\theta$ of the liquid, which is water when working under ambient conditions.

$$F_W = 4\pi R \gamma \cos(\theta) \tag{2.4}$$

*Comparison of Adhesive Effects*

Fig. 2.1 compares all the above listed forces and clearly shows that gravitation can be neglected in the micro world due to the fact that it scales with the volume, i.e. with the third power of the radius, whereas the surface forces are proportional to the square of the radius. Furthermore, in ambient environments the humidity can strongly increase the contact forces and, therefore, has to be considered in the design of micro manipulators.

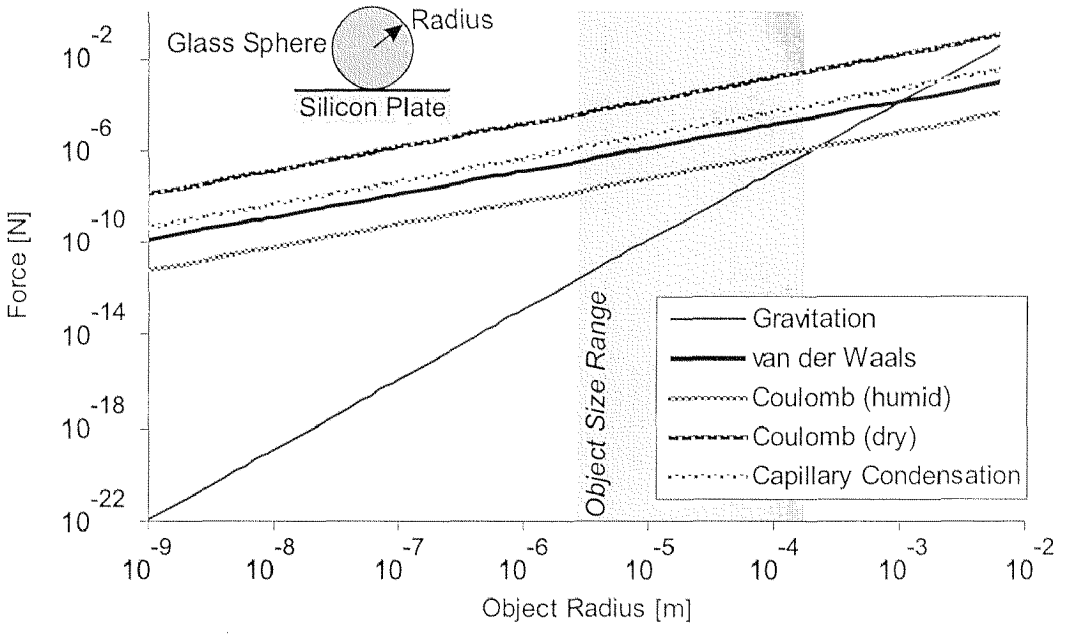


**Fig. 2.1:** *Comparison of forces between a glass sphere and a silicon plate in function of the object size according to eq. 2.1 - eq. 2.4 while following numerical values have been used:* $\rho = 3 \cdot 10^3\ kg/m^3$, $\varepsilon = 1$, $U_{humid} = 10\ mV$, $U_{dry} = 10\ V$, $z = 0.2\ nm$, $H = 40 \cdot 10^{-20}\ J$, $\gamma = 72\ mJ/m^2$, $\cos(\theta) \cong 1$

## 2.3 Glass Pipettes as Micro Manipulators

As already pointed out in section 2.1, a promising solution for micro manipulators is based on a needle-like design and the fact that the contact force between tool and particle can be varied. For this reason, the micro tool discussed in this section relies on the known capabilities of glass pipettes that are widely used in microbiology to manipulate cells [Brown86]. Besides the fact that the pipettes

have already proved their applicability in cell handling, further facts like easy production, low price and simple handling favor their usage in micro object handling. Based on these advantages we develop basic tasks for manipulating micro objects [Zesch97a] namely pick and place operations.

*Glass Pipette Manufacturing*

Micro pipettes are made of commercially available glass tubes. By heating the middle part of the tube and pulling both sides apart the tube is tapered to form a micro tip (fig. 2.2 a). By changing heating temperature and pulling velocity the pipette's geometry, i.e. length, diameter and shape, can be adjusted [Brown86]. After that the pipette has to be processed by cutting the front part of the tip (fig. 2.2 b) to enlarge the hole and get the optimal tip diameter for a given object size (fig. 2.6 b). In the subsequent experiments, the outer tip diameter is used to specify the glass pipette due to the fact that it easily can be determined under a light microscope. The inner tip diameter can be calculated as the quotient of inner and outer diameter of a glass pipette remains constant over the whole length [Brown86].

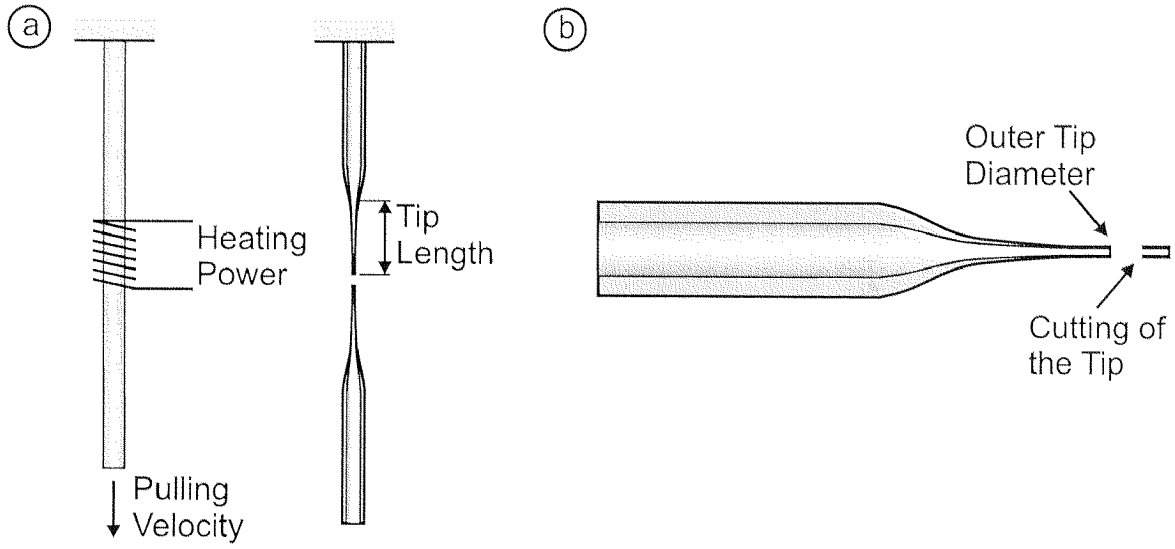


**Fig. 2.2:** *Pulling of glass pipettes (a) and postprocessing of tip geometry (b)*

*Basis Manipulation Tasks for Micro Object Handling*

These pipettes are then connected to a vacuum supply allowing us to apply and release vacuum to the tip. In order to derive possible manipulation strategies for micro particle handling, the necessary conditions to implement pick and place

operations must be analyzed by comparing the forces acting on the objects (fig. 2.3). Basically, four major forces act on the micro object while it is in contact with both the surface and the pipette: gravity $F_g$, adhesion to the surface $F_x$ (tangential) and $F_z$ (normal), adhesion to the pipette $F_n$ (normal) and $F_t$ (tangential) and the force due to the pressure difference from the applied vacuum $F_{vac}$.

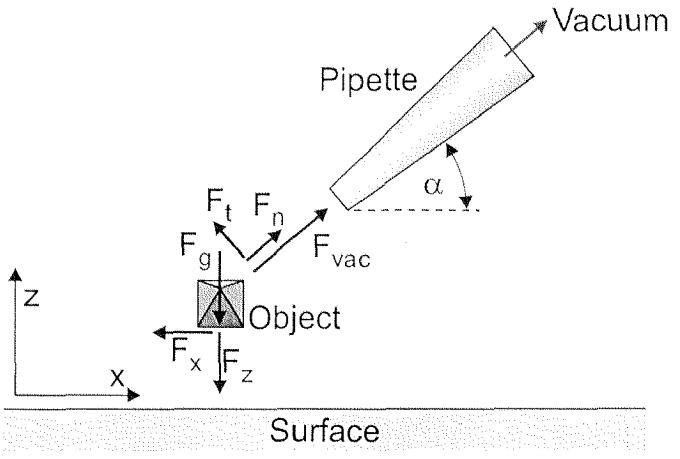


**Fig. 2.3:** *Forces during pick and place operations*

As mentioned above, gravity can be neglected in the micro and nano world. Hence, for the *pick operation*, eq. 2.5 has to be fulfilled while the tool withdraws from the surface. The force resulting from the applied vacuum must be strong enough to overcome the surface forces.

$$F_{vac} > \sin(\alpha)F_z - \cos(\alpha)F_x - F_n \tag{2.5}$$

The *move phase* is not critical, as for a large distance between object and surface the components $F_x$ and $F_z$ disappear. Moreover it is possible to switch off the vacuum as long as eq. 2.6 and eq. 2.7 are satisfied.

$$F_n > \sin(\alpha)F_g \tag{2.6}$$

$$F_t > \cos(\alpha)F_g \tag{2.7}$$

During the *place sequence* the limit for the pipette adhesion neglecting gravity is given by eq. 2.8.

$$F_n < \sin(\alpha)F_z + \cos(\alpha)F_x \qquad (2.8)$$

Analyzing these results, antagonistic demands for the pick and place conditions can be seen. The pick operation requires a large tip diameter because the force resulting from the applied vacuum scales with the cross-section of the pipette (eq. 2.5). On the other hand, a successful place operation works better with smaller tool diameters, because the adhesive effects are proportional to the contact area (eq. 2.8). To find the optimum, pick and place operations with 100 µm sized objects have been made and the success rate is calculated as a function of the tip diameter. Fig. 2.4 (b) shows that an optimal tool diameter is about one third of the object size.

To summarize, before the micro tool can pick an object, it must be positioned adjacent to the object of interest, then by applying a vacuum the object is grabbed and can then be lifted off and transported (fig. 2.4 a). In order to place it, the vacuum is released and the micro object is brought into contact with the surface.

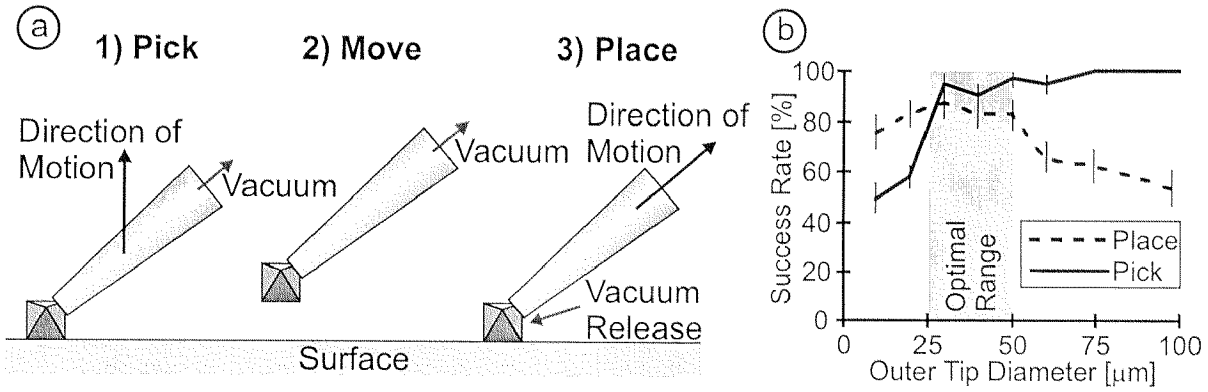


**Fig. 2.4:** *Principle tasks for micro object manipulation (a) and success rates in function of the tip diameter (b) measured at ambient conditions and an inclination angle of* $\alpha = 45°$ *based on approximately 1000 pick and place operations*

The new micro manipulator is capable of correctly placing a micro particle with a success rate of more that 75 %. In case of an unsuccessful place operation (i.e. the object could not be placed) first a second attempt should be made by withdrawing the object from the surface and reengage it. If the object can still not be released, it has to be *removed* from the pipette (fig. 2.5). One possibility is to strip off the particle at an edge or groove (a). The difficulty here is not to damage the tool while moving it close to a surface. To reduce such possible damages the object can be pushed off with a second tip (b). In situations with limited space

there is often not enough room for additional utilities. Thus, the object can also be blown away by applying pressure to the pipette. All mentioned removing methods have a success rate of 100 %, but it is not possible to release the particle at a defined position.

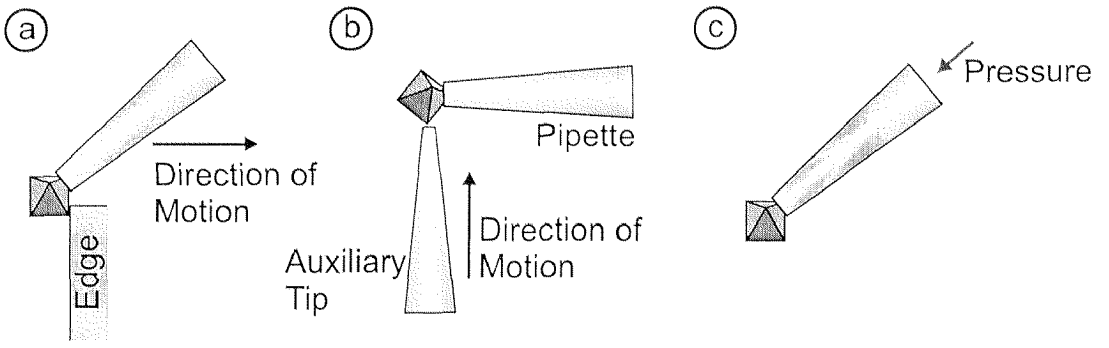


**Fig. 2.5:** *Possible strategies for removing a sticking particle*

*Tool Improvements with Coatings*

To minimize situations in which removal methods have to be applied, the success rate of the place operation must be increased. As already pointed out above, the adhesive forces $F_n$ and $F_t$ between tool and object can be very strong in ambient environment. According to eq. 2.8 the place operation can be improved by minimizing these adhesive effects. To reduce these adhesive interactions resulting mainly from the capillary condensation we coated the tool with a hydrophobic film [Knapp98a]. To find a coating that is sufficiently hydrophobic (to suppress capillary condensation), resistant to abrasion (to guarantee a stable tool), homogenous (to ensure an even coating) and easily applicable (to facilitate preparation and reduce costs) different types of coatings, namely gold and Teflon-like layers, have been compared.

For a quantitative comparison of these types AFM tips where coated [Knapp99] with either gold via a sputtering process (MED 010 by Balzers, Liechtenstein) or hexafluoropropene (HFP) using a plasma enhanced chemical vapor deposition (PE-CVD) process [Knapp98b]. In order to compare the adhesive force and the abrasion, measured data of the contact forces between the AFM tip and surface as well as SEM images of the tips after scanning them over the surface have been analyzed. Furthermore, pipettes were coated with each coating type and pick and place operations have been performed to determine the success rates.

Fig. 2.6 (a) shows the result of this analysis. Although coated and uncoated pipettes have excellent success rates in the place operation in environments with low humidity, the sputtered gold coatings and the Teflon-like layers obtained through HFP plasma treatment still show good behavior at high humidity, while the cleaned pipettes lose reliability. With both coatings a reduction of adhesion between two surfaces has been achieved and pick and place operations at ambient conditions were much improved. Depending on the micro particle to manipulate the kind of coating has to be selected. A gold coated tool should be preferred in case high electrostatic forces arise due to charged objects. Working at ambient conditions our experience has shown that the major part of adhesive effects results from capillary condensation. For this reason, we have chosen Teflon-like coated pipettes in the following experiments because of their good abrasion properties.

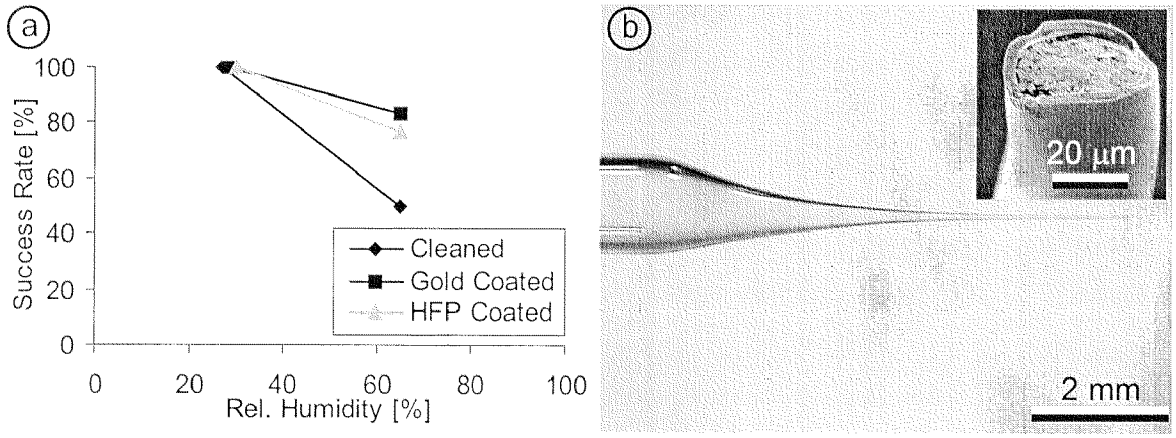


**Fig. 2.6:** *Success rate of the place operation in function of the humidity of different tool coatings based on approximately 250 trials (a) and tool geometry (b)*

## 2.4 Integration of Distance Sensor

The glass pipette based micro manipulator will be used in an automated robot environment. The implementation of collision avoidance tasks in order to prevent tool damage or automated local navigation for particle manipulation necessitate the integration of a distance sensor. Special emphasis is laid on a sensor system with fast response time and the capability of accessing the local dimension around the pipette tip.

In scanning near-field optical microscopes (SNOM) a widely applied principle to measure distances and control the tip-sample separation is based on shear force detection [Betzig92]. To this end, the tip oscillates at its resonance frequency. During approach to a surface the damping influence of the surface-tool interactions changes the resonance frequency which can be measured and used for distance control. Different setups have been suggested based on a tuning fork [Karrai95], a segmented piezo tube [Hsu95, Barenz96, Ruiter98] or a single piezo element [Hollricher98]. As sensor output the amplitude of the modulated system response signal [Salvi98], the phase signal [Wei98] or a combination of both [Lippitz99] can be used. Another approach calculates the root-mean-square (RMS) value of the vibration response to obtain the sensor signal [Hsu97].

*Simulation of Distance Sensor*

To simulate the sensor behavior the pipette is modeled. An analytical model can be found in [Vohnsen95]. To get the necessary information about the sensor behavior, a simple discrete model is sufficient. For this reason, the pipette is approximated by two tubes of different diameter ($d_{a1}$, $d_{a2}$) and length ($L_1$, $L_2$) and modeled as spring-mass system where several masses $m_i$ ($i = 0 \ldots n$) are connected by flexible beams of length $s_i$ with individual beam elasticity $EJ_i$ (fig. 2.7).

After separation of the mass elements from the beam and insertion of the contact forces $f_i$, the deflection $x_{i+1}$ of the flexible beam due to an applied force $f_i$ (i.e. the inertia of the mass element) can be calculated with a linear model as a sum of deflections according to eq. 2.9 - eq. 2.11 [Dubbel90].

$$x_{i+1} = x_i + x'_i s_{i+1} \tag{2.9}$$

$$x_i = \frac{s_i^3}{3 \cdot EJ_i} f_i \tag{2.10}$$

$$x'_i = \frac{dx_i}{dz} = \frac{s_i^2}{2 \cdot EJ_i} f_i \tag{2.11}$$

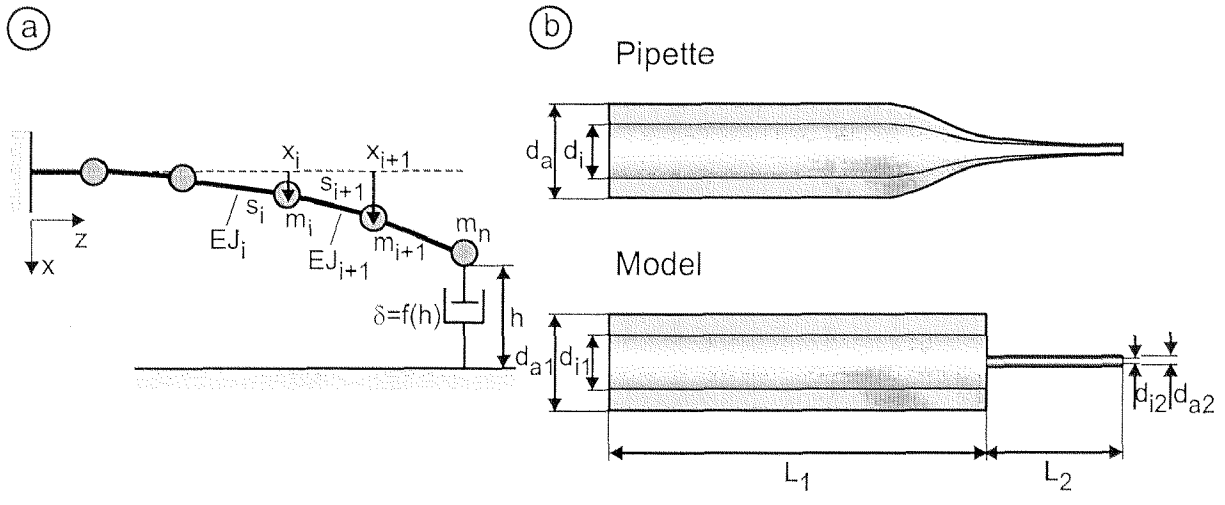


**Fig. 2.7:** *Spring-mass model of the pipette (a) as well as shape approximation used for the model (b)*

The total deflection due to all applied forces can be found as the superposition of individual deflections of each force $f_i$. Hence, the relationship between deflection and applied force can be written as a symmetric stiffness matrix $\underline{K}$ (eq. 2.12).

$$\begin{bmatrix} x_0 \\ \cdots \\ x_i \\ \cdots \\ x_n \end{bmatrix} = \underline{x} = \underline{K}^{-1}\underline{f} = \underline{K}^{-1}\begin{bmatrix} f_0 \\ \cdots \\ f_i \\ \cdots \\ f_n \end{bmatrix} \tag{2.12}$$

To analyze the dynamics of the system, we set up the differential equation (eq. 2.13) where $\underline{M}$ represents the diagonal matrix of mass elements and $\underline{D}$ the damping matrix in which the tip-surface distance depending damping $\delta$ is considered.

$$\underline{M}\ddot{\underline{x}} + \underline{D}\dot{\underline{x}} + \underline{K}\underline{x} = 0 \tag{2.13}$$

Solving for the eigenvalues and eigenvectors results in the resonance frequencies and oscillation modes of the system.

The calculated oscillation modes of the pipette using the numerical values in table 2.1 can be split up into two groups: in the modes of the first group the whole pipette is oscillating whereas in the second group mainly the tip is oscillating (fig. 2.8). Especially the second group of modes is of interest for the local force sensor, because high sensitivity to the damping influence of a nearby surface is achieved due to the fact that all oscillation energy is in the tip. Hence, the distance sensor is preferentially realized with such an oscillation mode.

| Symbol | Value Used for Simulation | Possible Value Range |
|---|---|---|
| Young's Modulus $E$ | $70 \cdot 10^9$ N/m$^2$ | |
| Density $\rho$ | 2200 kg/m$^3$ | |
| Outer Tube Diameter $d_{a1}$ | 1 mm | 1 - 1.5 mm |
| Inner Tube Diameter $d_{i1}$ | 0.58 mm | 0.3 - 0.8 mm |
| Outer Tip Diameter $d_{a2}$ | 20 µm | 10 - 50 µm |
| Tube Length $l_1$ | 5 mm | 5 - 30 mm |
| Tip Length $l_2$ | 3 mm | 0 - 5 mm |
| Number of Tube Elements $n_1$ | 25 | 10 - 100 |
| Number of Tip Elements $n_2$ | 15 | 10 - 100 |
| Damping $\delta$ | $10^{-7}$ Ns/m | $10^{-7}$ - $10^{-2}$ Ns/m |

**Tab. 2.1:** *Numerical values of the glass pipette used for the numerical simulation*

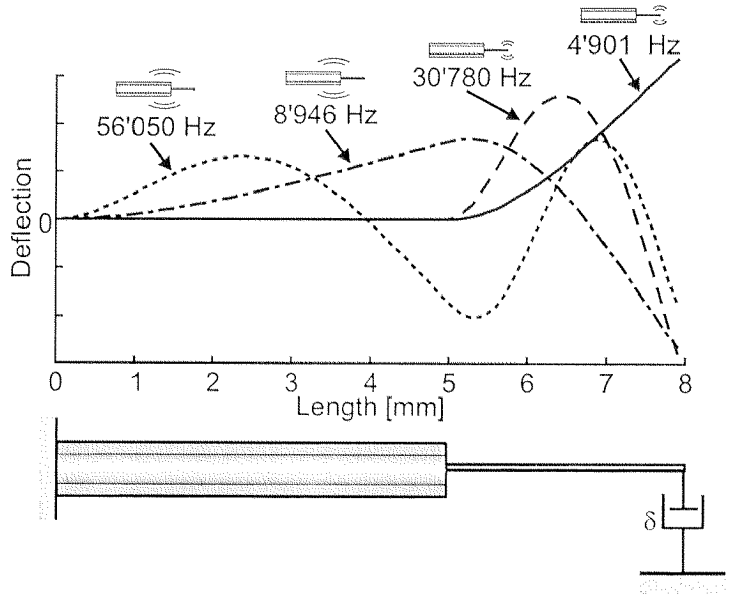


**Fig. 2.8:** *Simulation results of the discrete model with oscillating modes of the pipette*

*Experimental Verification of Distance Sensor*

To verify the simulation results, the micro tool is attached a four-segmented piezo tube using polyisobutylene (PIB) [Barenz96] to couple the pipette and the tube (fig. 2.9).This piezo tube is used to vibrate the micro tool. PIB is a viscous polymer that can easily be filled in the gap between pipette and piezo tube. At frequencies above 10 kHz the Young's modulus increases resulting in a more rigid coupling during excitation.

The excitation voltage is applied to one electrode (i.e. actuator 1 or 2 in fig. 2.9 b) whereas the system response is measured at the opposite side. With this setup both oscillation directions, normal and parallel to the surface, can be investigated. The actuator electrode is connected to a sine generator (Model 188, Wavetek) which is controlled by a PC. The response signal is processed by a lock-in amplifier (SR530, Standford Research Systems) to get the amplitude and phase signal for data acquisition with a computer. Finally, a mica surface that can be approached to the tip by a stack-piezo actuator is used as test target because of its atomically flat surface.

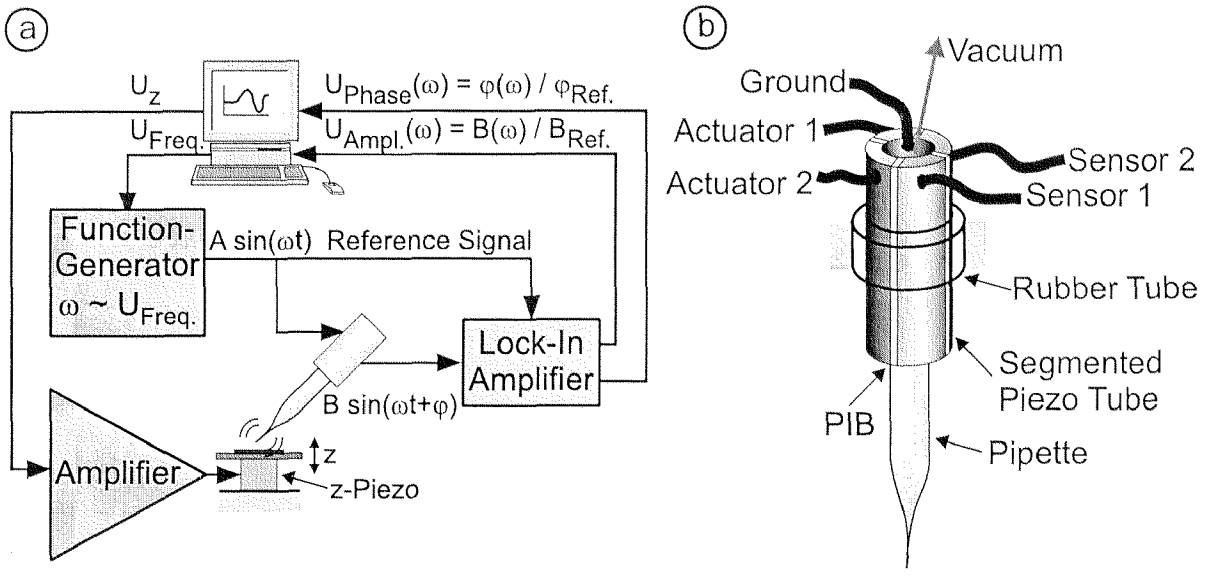


**Fig. 2.9:** *Schematic overview of experimental setup (a) and pipette fixture consisting of a piezo tube used as sensor and actuator unit (b)*

First, the amplitude signal is recorded as a function of the excitation frequency (fig. 2.10) for pipettes of different lengths $L_1$. The experiment clearly shows two types of oscillation modes as already found in the simulation. The first group is changing its resonance frequency with changing tool length, whereas in the second group mainly the tip is vibrating and, therefore, the resonance peak at 42 kHz is not varying with length $L_1$. This behavior depends on the tip geometry and hence not all tools show both types of oscillation modes. Furthermore, the damping influence of the approaching surface can be experimentally verified [Brunner97].

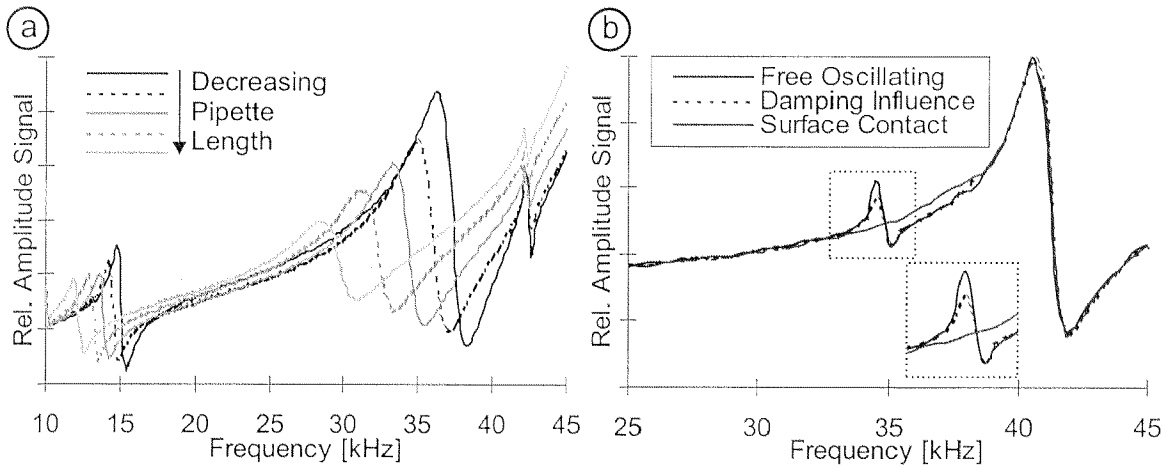


**Fig. 2.10:** *Amplitude response of pipettes of different tool lengths (a) and damping influence during approach to surface (b)*

*Investigation of Sensor Characteristics*

In the next step, the amplitude signal of the system during the approach to a surface is explored (fig. 2.11). Both oscillation directions parallel and normal to the surface are investigated, each with and without coating of the tool. All curves show a hysteresis between approach and withdrawal of the surface. On the one hand, this is due to adhesive effects between the pipette tip and the surface similar to the force curve behavior measured with AFM tips during engage and pull-off from the surface. On the other hand, the fixture of the pipette to the piezo with PIB seems not stiff enough to hold the forces acting on the tip. Furthermore, the influence of the liquid film can result in a strong non-linear decrease of the amplitude signal with uncoated pipette tips [Gheber98]. This is due to the immersion of the tip into the water film. With Teflon-like coated tools, this effect is much reduced and the distance sensor shows a relatively linear behavior.

The oscillation direction parallel to the surface shows a much stronger decrease than in the direction normal to the sample. For this reason, long sensor working ranges should be preferably realized with an oscillation direction normal to the surface, whereas for short distances the parallel direction is also a feasible solution.

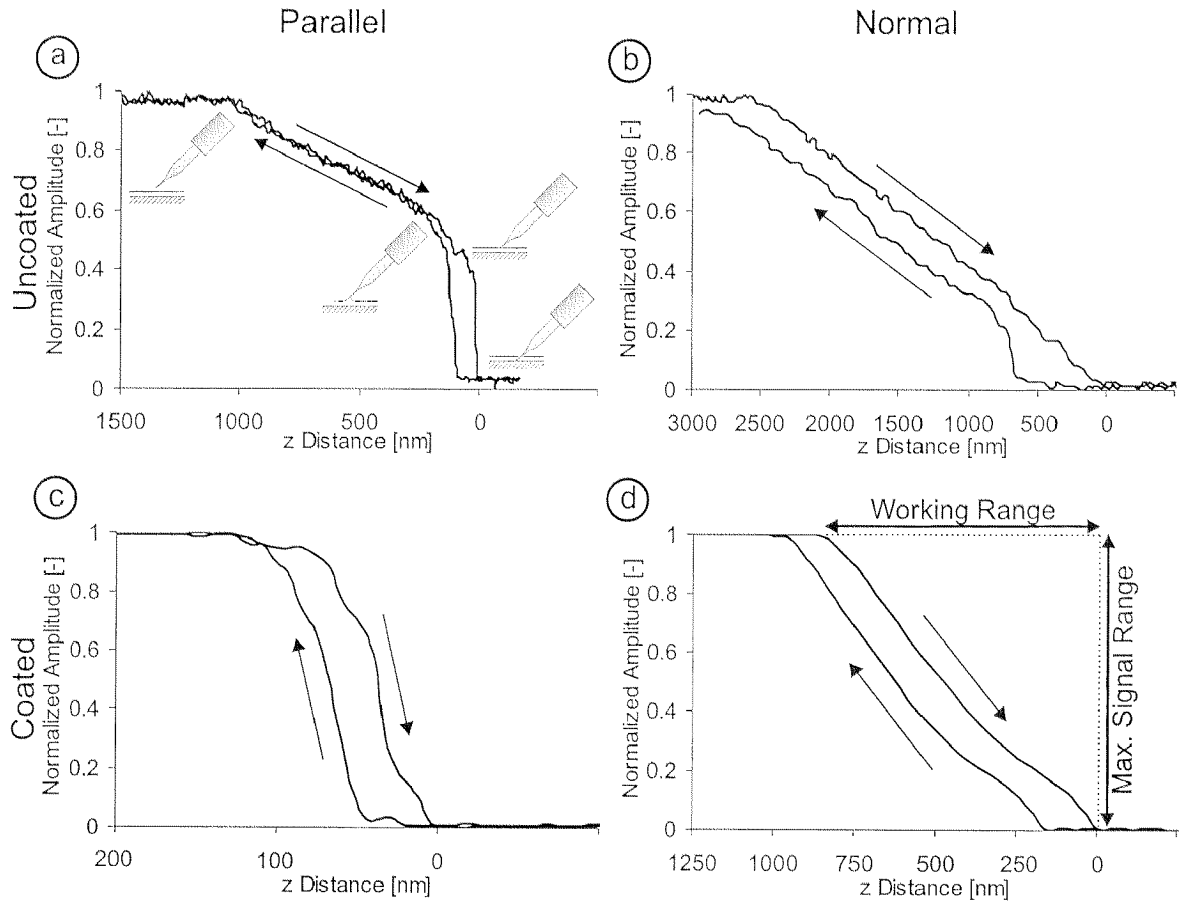


**Fig. 2.11:** *Amplitude response during approach to surface with oscillation direction parallel (a, c) and normal (b, d) to the surface for uncoated (a, b) and coated pipettes (c, d). All curves are measured with different excitation voltages while the coating curves are taken at a relative humidity of 55 % and the resonance frequency of the tip is 33,4 kHz*

For the manipulation of object sizes between 40 and 200 µm at ambient conditions, a large sensor distance range is recommended. Consequently, we use Teflon-like coated glass pipettes and operate the local distance sensor in the oscillation mode normal to the surface. The maximum sensor signal range (i.e. the maximal difference in the sensor signal that is available to the electronics) as well as the working range (i.e. the largest distance that can be acquired) of the sensor during approach to the surface are measured as a function of the excitation voltage. Both working range and maximum sensor output signal depend linearly [Chen94, Bugacov99] on the excitation voltage (fig. 2.12).

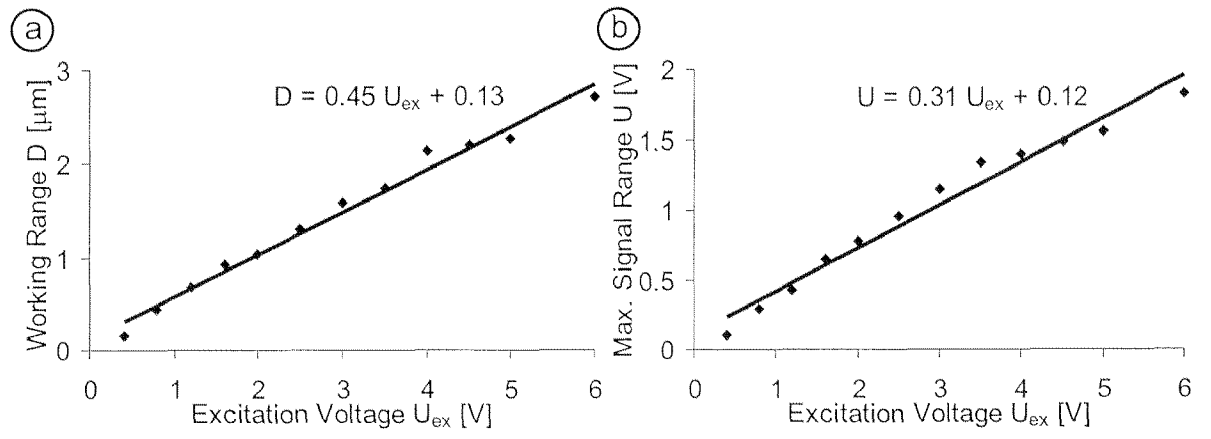


**Fig. 2.12:** *Sensor working range (a) and max. sensor signal output (b) (see fig. 2.11 d) of tapping direction in function of peak-to-peak excitation voltage at ambient conditions of a Teflon-like coated pipette*

## 2.5 Benchmarks

To prove the capabilities of the micro pipette with integrated local distance sensor different object types have been manipulated. A hydrophobic coating (i.e. a Teflon-like layer) reduces adhesive effects with the objects. The new micro tool combines sensor and actuator functions in one single point which is essential to enable access to small dimensions. Fig. 2.13 shows the result of 2D and 3D structures built of 200 µm sized metal beads as well as 40 - 50 µm sized glass beads placed on a silicon wafer and manipulated at ambient conditions.

The glass beads (fig. 2.13 b, c) were first picked up by approaching them with the distance sensor turned on. At a distance of some tens of nm in front of the object the vacuum is turned on and the object is picked. Then, it is moved to its appropriate new position and placed. Compared to manipulations without distance feed back (fig. 2.13 a), the pick operation is vastly improved because the object can precisely be approached without touching it. Without a distance sensor, the object is either approached until it moves and hence the tool is in contact with the object or the distance is set to several µm and the particle is picked with high vacuum forces that can lead to a grabbing of multiple objects at the same time. The hydrophobic coating of the tools improves the handling of small objects because the proper placement is enhanced (fig. 2.13 c).

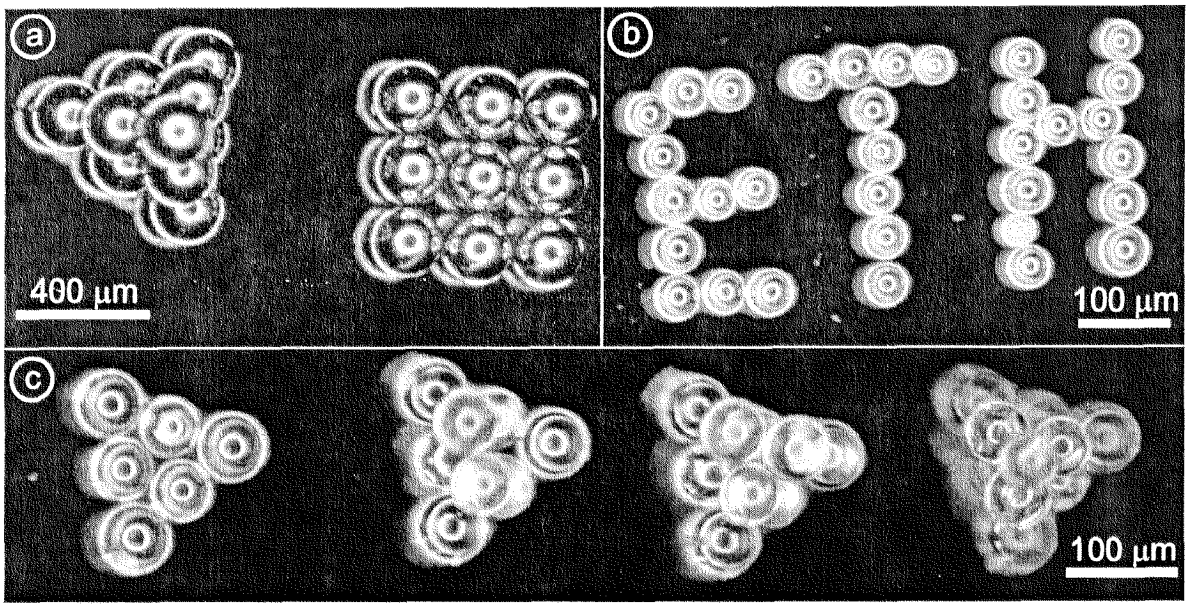


**Fig. 2.13:** *2D and 3D manipulation examples of 200 µm sized metal beads (a) as well as 40 - 50 µm sized glass beads (b, c)*

## 2.6 Tool Improvements and System Integration

The introduced micro pipette with integrated distance sensor has proved its applicability as a micro tool. In the future, some improvements in the setup could enhance the handling abilities.

*Mechanical Improvements of the Micro Manipulator*

First, PIB as a coupling medium between glass pipette and piezo tube can be replaced by a mechanical fixture (fig. 2.14 a). This would facilitate the exchange of a pipette by simply pressing the backside of the clamp towards the piezo to release the tool. After insertion of a new pipette the clamp can be freed to fix the manipulator at a defined position. Furthermore, the signal transfer characteristics will be improved due to the stiffer coupling between the pipette and the piezo while disturbances from the environment will be decoupled by the rubber fixture. In addition, this mechanical fixture allows an application of the sensor setup in a vacuum environment because there is no PIB that could degas.

Second, a more precise control of the vacuum force can be achieved by using glass tubes with multiple channels. This allows one to apply the vacuum in each tube individually enabling smoother force characteristics. Additionally, mechanical adhesion is decreased because the objects can not get stuck in the tube channels (fig. 2.14 b).

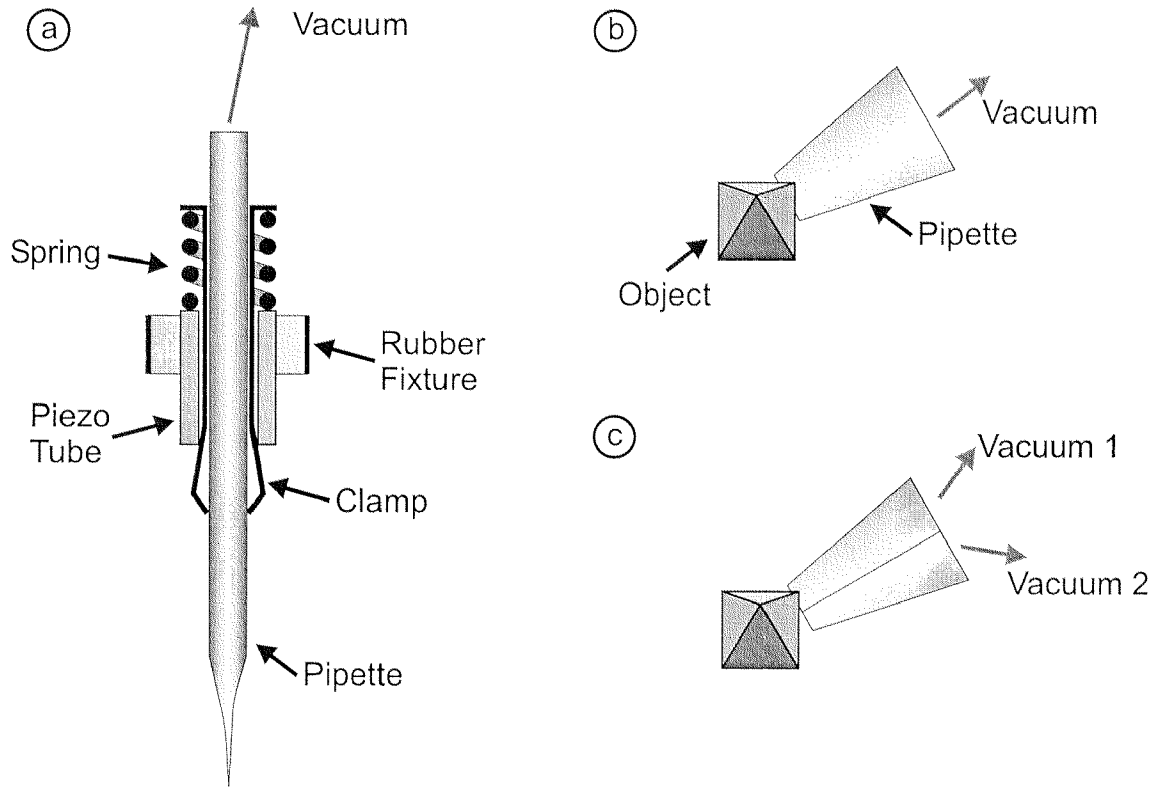


**Fig. 2.14:** *Improvements of the micro manipulator setup with a new clamp system (a), mechanical adhesion (b) and its prevention using a pipette with multiple tubes (c)*

*Integration into an Automated Environment*

The response time of the local distance sensor is faster than other measuring methods, e.g. vision based algorithms [Danuser97]. This favors the integration of this new concept of a tool combined with a local sensor in a fully automated robot environment. On a low automation level, collision avoidance is a basic task that prevents tool damage during execution of automated tasks. Further algorithms that are capable of finding the micro particles automatically or that are able to perform pick and place tasks without any user interactions would be of great value. Such a sensor-guided robot will be able to automatically perform

user-defined tasks by working on a higher automation level than simple teleoperation systems.

In order to implement behavior rules for a system working on the nanometer scale, an experimental setup has to be designed that allows us to test the algorithms. Such algorithms have to be capable to work with any information from the nano world. Due to the multifunctional character of nano probes a test platform is needed on which multiple sample properties can be measured at the same time. Furthermore, the algorithms have to be tested on much smaller structure than the manipulated micro objects. For these reasons, a test platform is presented in the next chapter on which control strategies based on multiple sensor signals can be implemented and evaluated. Special emphasis is laid on a modular concept that allows the platform to be accommodated to the use of different local tools.

# 3 A Test Platform for Evaluation of Control Strategies

In this chapter, the theoretical approach to sensor-guided nanorobots, which was introduced in section 1.1, will be carried on to a concrete realization. Several possible setups will be discussed and the final implementation will be introduced. The discussed system will be used as a test platform on which behavior rules and control strategies can easily be designed and evaluated on the nm-scale and, therefore, will be the base for implementing new concepts for interaction with the nano world.

## 3.1 Requirements for a Test Platform

The design of a test platform must be flexible enough to adapt it to different needs. Possible fields of application can be the investigation of integrated circuit structures (see section 1.2) to derive critical parameters for optimization or the automated particle manipulation with a new generation of tools (see chapter 2). Thus, special emphasis is laid on a modular concept and an open design of the arrangement which is motivated by the fast changes in requirements for such test platforms.

The aforementioned requirement necessitate that a micro tool can be positioned in a large working range (e.g. to handle the IC structures on a silicon wafer or build 3D structures with a micro manipulator) with nm resolution (e.g. to allow

data acquisition on (sub)micro structures or precise alignment of micro fabricated parts). A sensor subsystem has to provide us with all necessary information to perform the defined task. On the one hand, these are near-field data from the tool (e.g. topography, surface potential, local distance to the surface, etc.) and, on the other hand, far-field information (e.g. from a CCD camera). All sensor signals are processed in a controller that generates the necessary actuator commands to perform the tasks.

In addition, the controller part must permit a flexible implementation of behavior rules and allow time-critical tasks to be run under real-time conditions. Furthermore, an open architecture will allow components (e.g. the tool or the actuator type) to be exchanged, added and removed as well as all required signals to be accessed. Last but not least, the robot system will be employed in industrial environments by users who often are not familiar with data acquisition techniques. Hence, an easy-to-understand user interface with software functions for automated system setup are needed. In the following sections, the mechanical setup will be introduced. Then, the necessary electronic components and the software structure are discussed in detail.

## 3.2 Mechanical Setup

### 3.2.1 General Overview

A schematic overview of our current setup is shown in fig. 3.1. The system consists of a sensor, an actuator and a controller part. The sensor-guided nanorobot will primarily work on IC structures and thus a local sensor is needed which can acquire properties of interest of such samples. Both STM and AFM are possible solutions to acquire local information in ambient environment. An AFM tip has been chosen to supply us with near-field inputs like topography, surface potential, etc., because the sample does not have to be conductive as compared to STM samples. Furthermore, a light microscope is integrated to extend the robot's field of view beyond the tip's range and to allow wide-range observation of the specimen.

Owing to the fact that the sensor-guided nanorobot will be mainly used on integrated circuits, the whole system should be capable of working on 6-inch wafers, which are widely used as substrates for fabrication of micro electronics. Thus,

the actuator part must be able to position the sample within a working range of 150 x 150 x 30 mm with nm resolution [Zesch97b]. These requirements can be realized either by using stepping mechanisms based on stick-slip principles [Besocke87, Higuchi90, Büchi95, Zesch95] or by splitting up the actuator task into a fine and a coarse positioning part. In the current system, we have chosen the second strategy with 3 degrees of freedom (DOF). Nevertheless, this limitation can easily be overcome by adding modules for rotational DOFs. In the following sections each component of the setup will be discussed in detail.

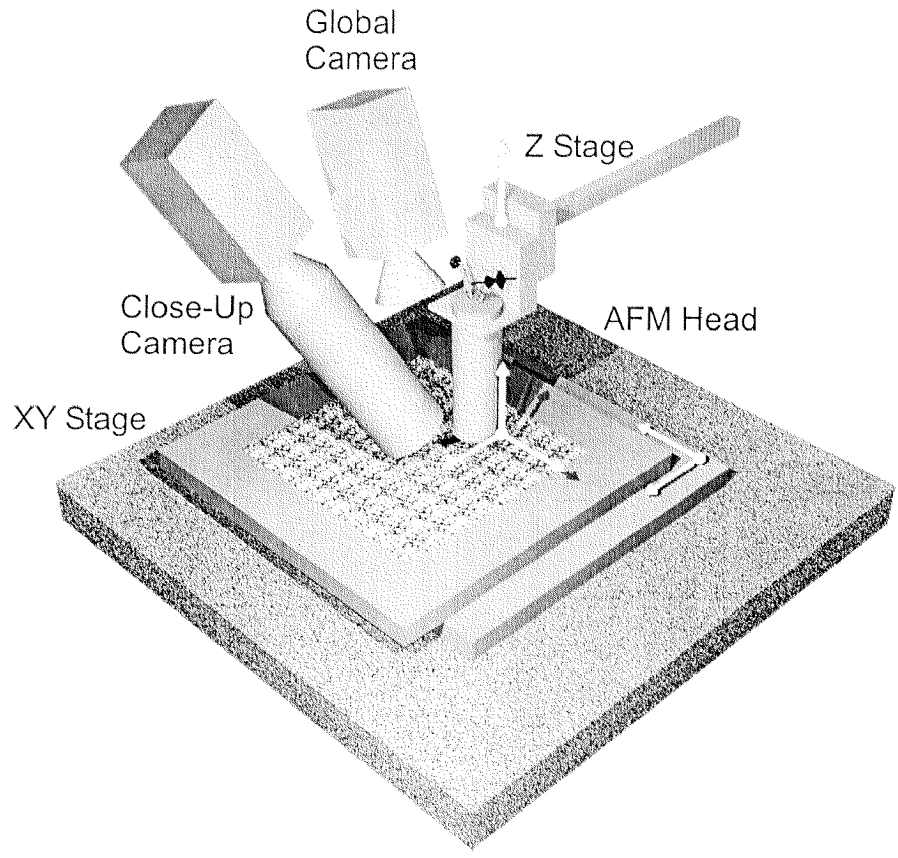


**Fig. 3.1:** *Principle setup of the sensor-guided nanorobot*

### 3.2.2 Actuators

*Fine Positioning Device*

The fine positioning device is realized by a piezo tube. Two different concepts are possible: the first one is using a single tube with 4 electrodes (fig. 3.2 a) while the second uses two tubes (fig. 3.2 b).

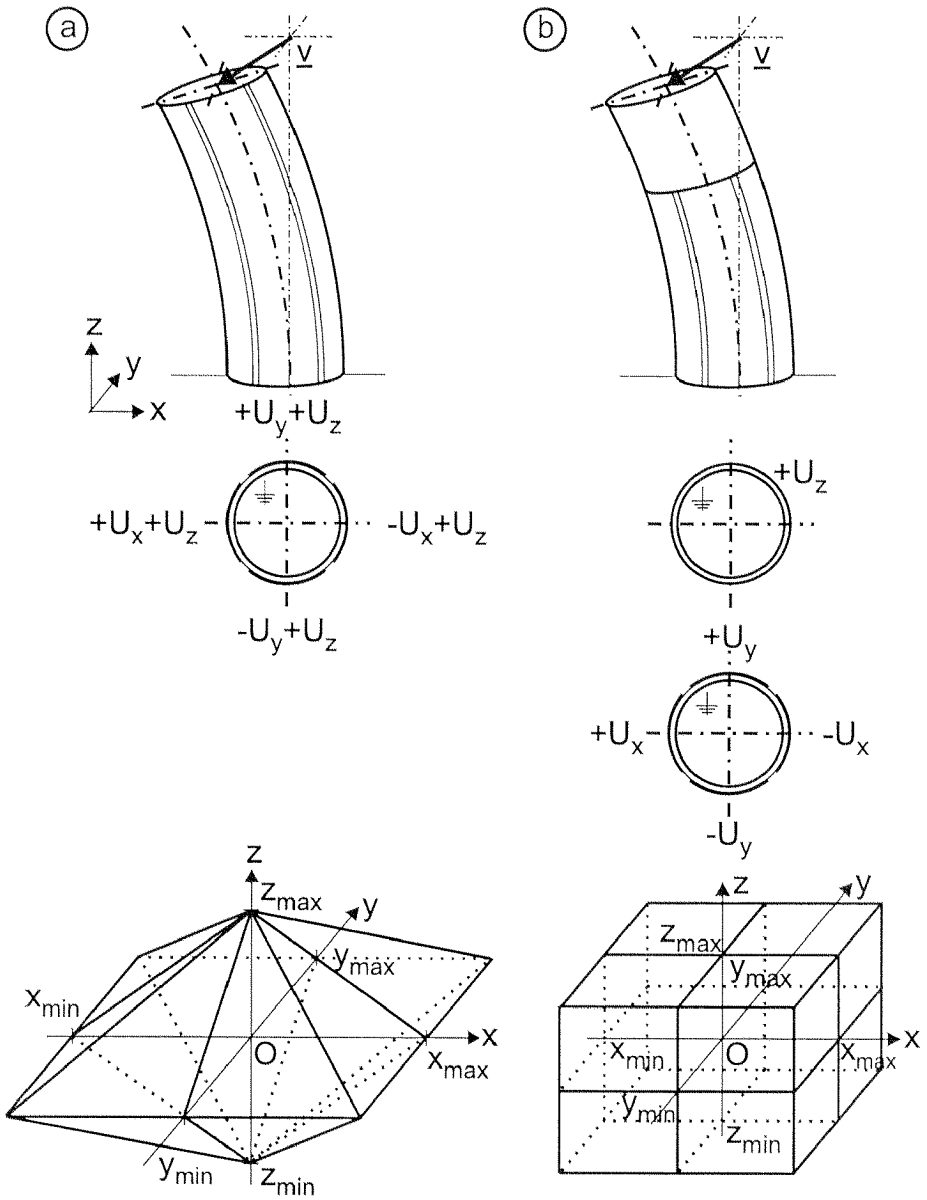


**Fig. 3.2:** *Actuation principles and resulting work space for 3 DOF fine positioning device*

The 3-dimensional displacement $\underline{v}$ is split up into two components: the xy-movement is realized by applying a position proportional voltage ($U_x$, $U_y$) to one electrode-segment and the inverse value to the opposite. The z-movement is performed by adding the z-voltage ($U_z$) to all 4 electrodes. In the second solution the xy-voltages are applied to one piezo whereas the z-value is fed to a separate piezo. This results in a cubic work space compared to a bipyramidal one in the first principle where the base xy-plane is larger due to the larger length of the

segmented piezo tube. The z-value depends on the actual xy-position, because the maximum permissible voltage that can be applied is limited by the amplifier and the piezo ceramics.

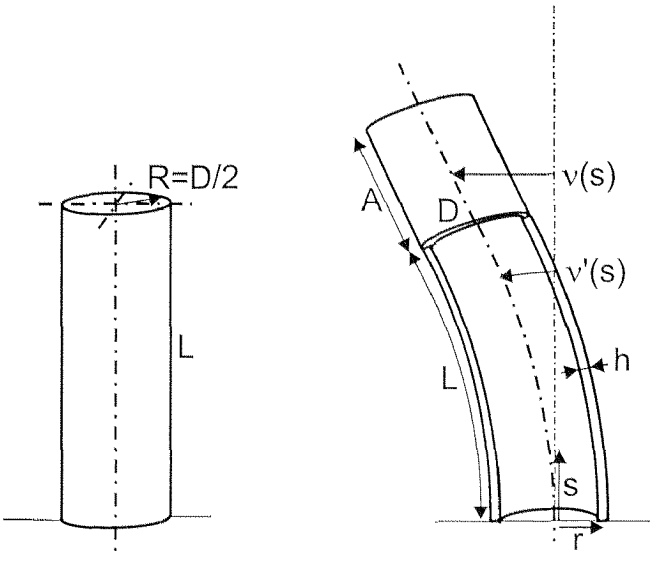


**Fig. 3.3:** *Model for piezo displacement calculation*

To calculate the working space of the fine positioning device, we model the tube with diameter $D$, length $L$, wall thickness $h$ and bending rigidity $EI_z$ as a beam (fig. 3.3). Solving eq. 3.1 that describes the strain $\varepsilon$ under the bending torque $M_b$ with the boundary conditions eq. 3.2 and eq. 3.3 yields the deflection line $v(s)$ of the beam (eq. 3.4).

$$\varepsilon = \frac{M_b}{EI_z} r = r \frac{\partial^2}{\partial s^2} v(s) \tag{3.1}$$

$$\frac{\partial}{\partial s} v(0) = v'(0) = 0 \tag{3.2}$$

$$v(0) = 0 \tag{3.3}$$

$$v(s) = \frac{\varepsilon s^2}{2r} \tag{3.4}$$

Substituting the variables $r$ and $s$ by the geometric parameters of the tube and considering the piezo expansion characteristic $d_{31}$ under the applied voltage $V$

results in the calculated displacement $x_{th}$ of the beam (eq. 3.5). This theoretical value has to be corrected with the factor $k$ [Chen92] due to the fact that we have a round cross-section (eq. 3.6).

$$x_{th}(V) = v(L)\Big|_{r=\frac{D}{2},\varepsilon=\frac{\Delta L}{L},\Delta L=\frac{d_{31}VL}{h}} = \frac{L\Delta L}{D} = \frac{d_{31}VL^2}{hD} \tag{3.5}$$

$$x(V) = kx_{th}(V) = \frac{2\sqrt{2}}{\pi}x_{th}(V) \tag{3.6}$$

To enlarge the working range in xy-direction the scanner can be prolonged by a passive extension of length $A$. The resulting displacement is then calculated with eq. 3.7.

$$v(L+A) = v(L) + \frac{\partial}{\partial s}v(L)A \tag{3.7}$$

$$x(V) = k\frac{\Delta L(V)}{D}(L+2A) = \frac{2\sqrt{2}}{\pi}\frac{d_{31}VL}{hD}(L+2A) \tag{3.8}$$

The displacement in xy-direction can then be obtained with eq. 3.8. The displacement in z-direction is calculated according to eq. 3.9.

$$z(V) = \frac{d_{31}VL}{h} \tag{3.9}$$

In the current setup, a single piezo tube with 4 electrodes and properties summarized in table 3.1 is used (lead zirconate titanate tube EBL#3 from Staveley Sensors Inc., East Hartford, USA). We obtain a measured scanner working range of 88 x 92 µm in xy-direction, whereas the maximum z-displacement is 11.5 µm. The theoretical range is 110.8 x 110,8 µm in xy-direction and 7.7 µm in z-direction. The difference between measured and calculated values are due to aging of the piezo ceramics resulting in a decrease of the parameter $d_{31}$.

| Symbol | Value |
|---|---|
| Piezo Tube Length L | 50.8 mm |
| Extension Length A | 50.8 mm |
| Tube Wall Thickness h | 0.762 mm |
| Tube Diameter D | 19.05 mm |
| Piezo Constant $d_{31}$ | $-262 \cdot 10^{-12}$ m/V |
| Max. Applied Voltage $V_{Max}$ | ±220 V |

**Tab. 3.1:** *Numerical values of the scanner*

The fine positioning device is combined with a coarse positioning stage to extend the nanorobot's working range. To match both coordinate systems the coordinate transformation has to be calculated (see section 4.2.1). Due to creep and non-linearities of piezo ceramics, namely hysteresis, this step is preceded by a linearization of the piezo scanner. Preisach [Preisach35] proposed a hysteresis model in which the whole hysteresis behavior is approximated by an integration over elementary hysteresis operators with different weights.

In detail, Preisach defined a hysteresis operator $\gamma_{\alpha\beta}$ with the behavior of switching at the voltage position $\alpha$ to an output value of +1 and to -1 at a position $\beta$ ($\beta \leq \alpha$) [Mayergoyz91, Ge97, Hughes97]. By weighting this operator with a factor $\mu(\alpha, \beta)$, the compensated output voltage $f(t)$ can be calculated by integrating the input $u(t)$ over the interesting range (eq. 3.10). During the compensation calculation, the previous local maximum and minimum voltage values are stored and considered in the boundaries of the integration.

$$f(t) = \iint_{\alpha \geq \beta} \mu(\alpha, \beta)\gamma_{\alpha\beta}u(t)d\alpha d\beta \qquad (3.10)$$

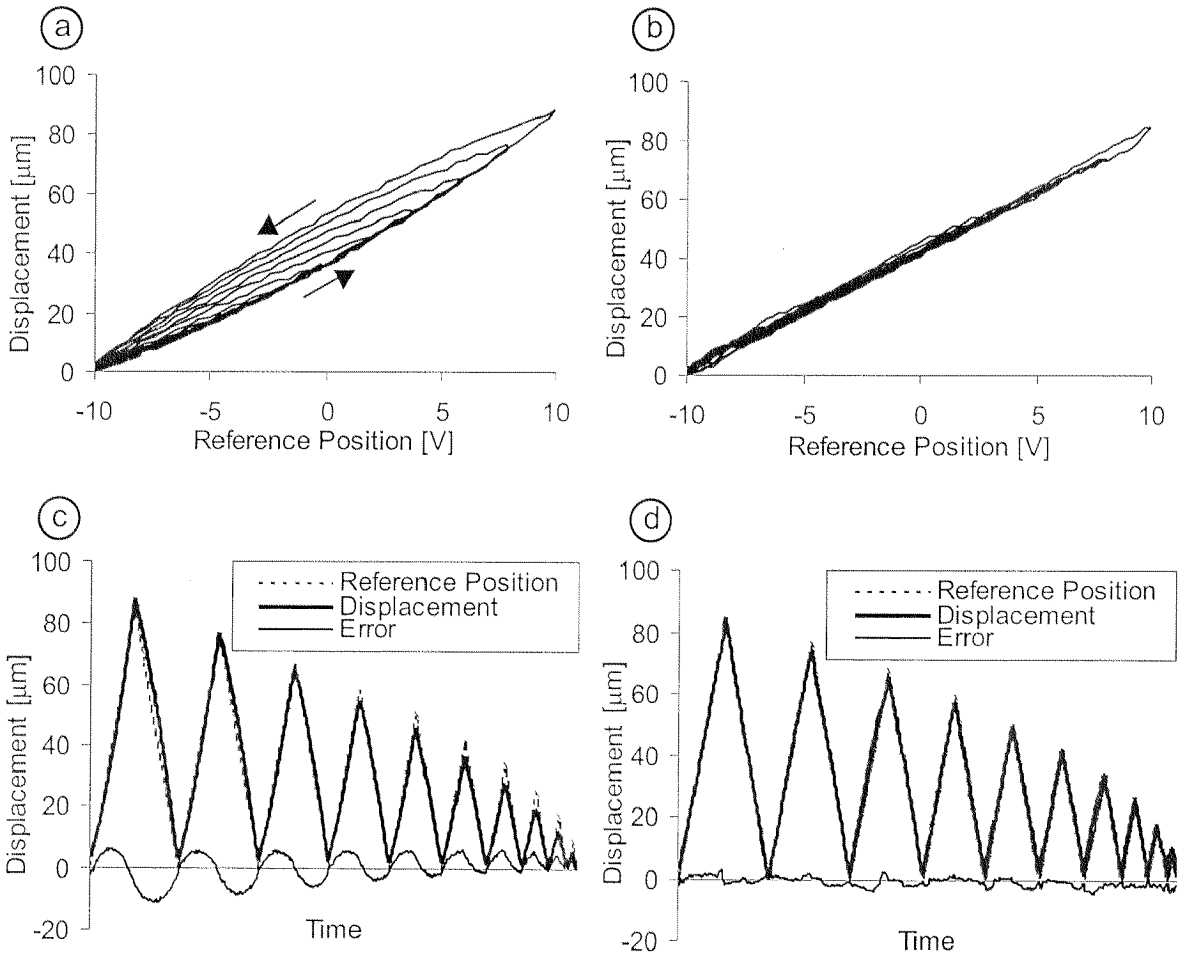


**Fig. 3.4:** *Measured displacement of x-axis without (a) and with (b) hysteresis compensation. Positioning error of x-axis without (c) and with (d) compensation*

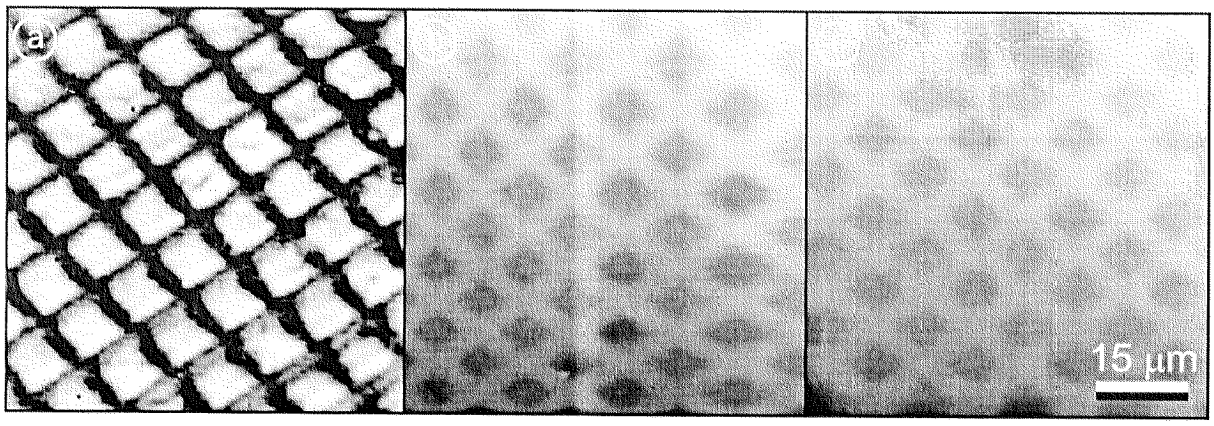


**Fig. 3.5:** *CCD image of test sample (a) and AFM image without hysteresis compensation (b) as well as with compensation (c)*

This hysteresis compensation linearizes the xy-motions. Fig. 3.4 shows the measured displacement with and without the compensation for different voltages as well as the errors of the model. Fig. 3.5 demonstrates the advantage of the scanner linearization algorithm by comparing of 2D images acquired with and without it.

*Coarse Positioning Device*

The coarse positioning device is realized by translation stages operated by stepping motors in an open-loop mode (Erlic 85 from Owis GmbH, Staufen, Germany). These stepper motors can run either in full-step, half-step or micro-step mode [Kuo74, Kuo79, Prautzsch88]. In the first two modes a square-wave voltage is applied to the poles of the motor. In the micro-step mode a sinusoidal signal is used so that a full-step can be interpolated with 64 micro-steps, in the following text simply called steps. We use the stages in micro-step mode which affords a resolution of <2 µm. This is sufficient to position the sample inside the working space of the fine positioning device, i.e. the piezo scanner. In practice, steps smaller than 1.5 µm should be avoided due to friction and sticking effects.

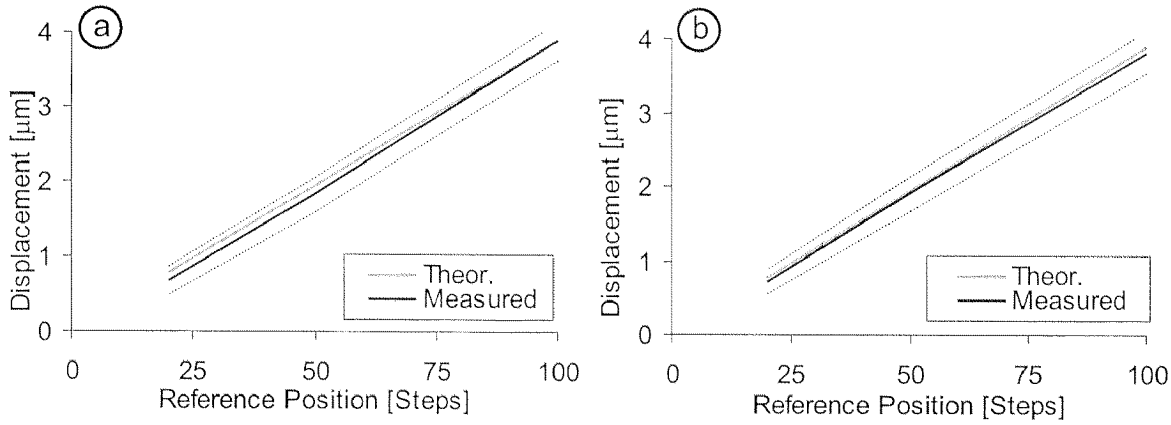


**Fig. 3.6:** *Comparison of theoretical and measured position along the x-axis (a) and y-axis (b) with standard deviation boundaries*

*Control Strategy for Positioning Devices*

Both coarse and fine positioning device operate in an open-loop mode. Consequently, the resolution for positioning is worse compared to a closed-loop mode. Nevertheless, the linearity of the devices is sufficient (fig. 3.6) to position the sample inside the working range of the AFM sensor. The whole subsystem could

very well be extended with sensors and controllers for closed-loop mode. But we intended to take a different approach. Instead of integrating many sensors, which are still limited in resolution, and other components into the system to linearize the positioning movements, we implemented intelligent control algorithms that are capable of compensating for such imperfections of the actuators. This approach is similar to nature's behavior where a human arm is not only linearized in the joints, but the whole motion is also controlled by vision and tactile information.

### 3.2.3 Sensors

*AFM Probe as Local Sensor*

The AFM sensor is mounted on the fine positioning device and integrated in one compact AFM head. Hence, all necessary parts for AFM measurements are united in an universal module that can be used in various setups, e.g. with different coarse positioning devices. Fig. 3.7 shows the components and the working principle.

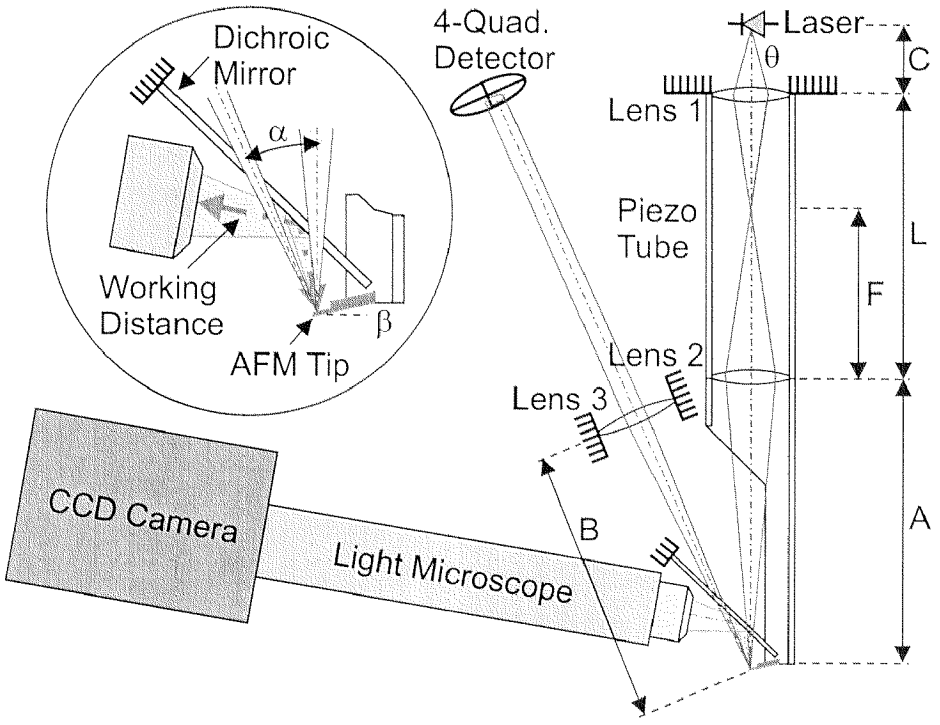


**Fig. 3.7:** *Schematic overview of sensors including an AFM tip for local data acquisition and a light microscope for global information*

A laser beam is focussed on the cantilever and reflected onto a detector. Upon bringing the AFM tip in contact with a surface, the force between probe and sample causes the cantilever to bend. This vertical displacement of the tip can be measured with the detector and is used as sensor signal characterizing the local nature of the sample. Due to the fact that the AFM sensor is scanning over the surface, the laser beam has to follow the tip movements. Hansma *et al.* [Hansma94, Stemmer95] proposed a setup in which lenses are used to track the focus point of the laser beam along the tip motion. A first lens focusses the beam into the piezo tube. The second lens moves together with the scanner and projects the focus point onto the cantilever. The third lens collimates the reflected beam onto the detector.

To specify the focal distance of the lenses, Gaussian beam optics are used [Self83, Hecht90, Saleh91]. The intensity of laser beams with a radius $r$ and an intensity $I_0$ has a Gaussian distribution as described by eq. 3.11. We can define the angular divergence $\theta$ of such a beam (eq. 3.12) which is a function of the wavelength $\lambda$ and the minimum beam waist $w_0$.

$$I(r) = I_0 e^{\frac{-2r^2}{w_0^2}} \tag{3.11}$$

$$\theta = \frac{\lambda}{\pi w_0} \tag{3.12}$$

If a lens with a focal length $f$ is placed in the path of a Gaussian beam, the beam waist after the lens, $w_f$, can be calculated according to eq. 3.13.

$$w_f^2 = w_0^2 \frac{f^2}{z^2 + \left(\frac{\pi w_0^2}{\lambda}\right)^2} \tag{3.13}$$

The variable $z$ represents the distance of the beam waist to the focus point before the lens. The location of the beam waist after the lens, $z_f$, can be calculated according to eq. 3.14.

$$z_f = \frac{zf^2}{z^2 + \left(\frac{\pi w_0^2}{\lambda}\right)^2} \tag{3.14}$$

A laser with a wavelength $\lambda$ of 670 nm and a divergence $\theta$ of 1 mrad is used. With these laser properties and the geometrical values (table 3.1), the lens parameters can be calculated (table 3.2) as well as the distances and beam waists in the focal points (table 3.3).

| Lens Number | Focal Length |
|---|---|
| 1 | 30 mm |
| 2 | 15 mm |
| 3 | 80 mm |

**Tab. 3.2:** *Lens parameters (fig. 3.7)*

| Symbol | Value |
|---|---|
| B | 72.08 mm |
| C | 21.68 mm |
| F | 21.28 mm |
| Beam Waist after Lens 1 | 2.56 µm |
| Beam Waist after Lens 2 | 5.99 µm |

**Tab. 3.3:** *Geometrical values of sensors system (fig. 3.7)*

The inclination angle $\beta$ of the AFM sensor was set to 12° which leads to an angle $\alpha$ of 24°. To show the lateral and vertical resolution of the AFM sensor head, the pits on a CD with a depth of approximately 200 nm are imaged (fig. 3.8). This proves the applicability of this AFM head as local sensor for the observation of IC structures. Further tests have shown that the z resolution is about 0.5 - 1 nm.

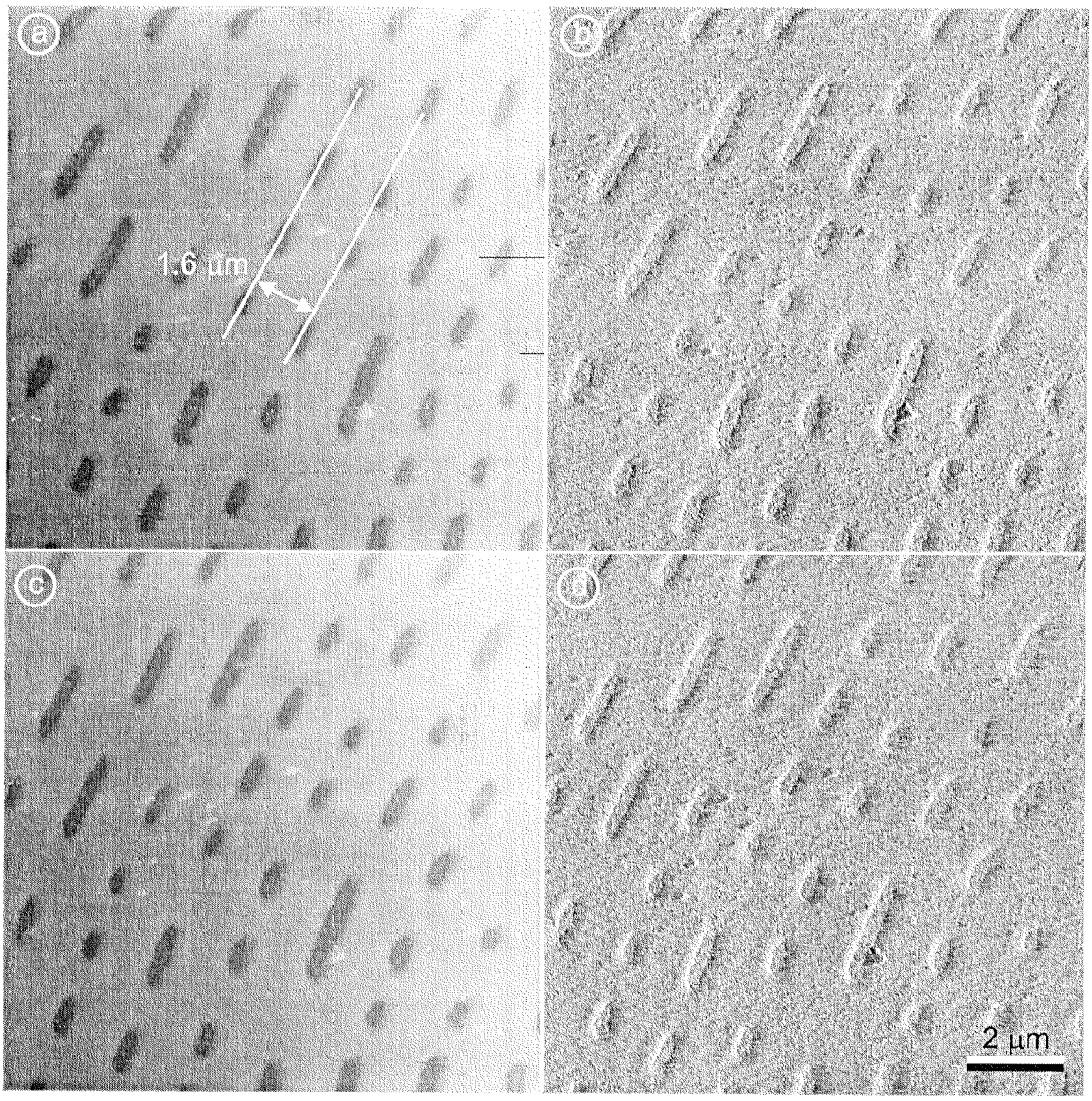


**Fig. 3.8:** *AFM image of CD pits with topography data of forward (a) and backward scan (c) as well as PI controller error signal of forward (b) and backward scan (d)*

*Video Microscope as Far-Field Sensor*

In addition to the AFM sensor, a second data acquisition device was integrated to gather far-field information. In detail, a light microscope (Nikon CM10 with CF Plan EPI SLWD objective and Köhler illumination) with properties as listed in table 3.4 is used. The angle $\delta$ is calculated using eq. 3.15 for ambient conditions

namely a refraction index $n$ of 1 for air as surrounding medium and denotes an important value for dimensioning the minimum size of the dichroic mirror.

| Symbol | Value |
|---|---|
| Working Distance WD | 20.5 mm |
| Numerical Aperture NA | 0.35 |
| Magnification | 20x |
| Angle $\delta$ | 20.48° |

**Tab. 3.4:** *Numerical properties of light microscope*

$$NA = n\sin(\delta) \tag{3.15}$$

To use the light microscope as a sensor, we added a CCD camera (LV-8500 from Leutron Vision, Glattbrugg, Switzerland). The resolution $r$ of such a sensor design can be calculated according to the well known Rayleigh criterion (eq. 3.16) [Inoué97].

$$r = 0.61\frac{\lambda}{NA} \tag{3.16}$$

With a typical wavelength $\lambda$ of 550 nm, a resolution of 958 nm can be achieved. This resolution must be digitized by the CCD camera. According to Shannon [Dubbel90, Geering90] the spatial sampling frequency of the camera must be at least twice the highest spatial frequency of the microscope system, i.e. the reciprocal of the calculated resolution. Considering that the calculated resolution of 958 nm is magnified by a factor of 20 while passing trough the microscope, the resulting image on the CCD chip has a size of 19.16 µm which is more than twice the pixel size of 8.3 µm. Comparing the calculated resolution limit with measurements (fig. 3.9) proves the calculation. Hence, the sensor is very well suited to an environment where integrated circuits will be examined.

To combine both local and global sensors and to get a top view of the scene with the optical microscope a dichroic mirror has to be integrated which allows the laser beam at 670 nm to pass through the mirror whereas the optical path of the

light microscope will be reflected. Therefore, a dichroic mirror with a cut-off wavelength close to 670 nm is chosen that transmits light above this wavelength.

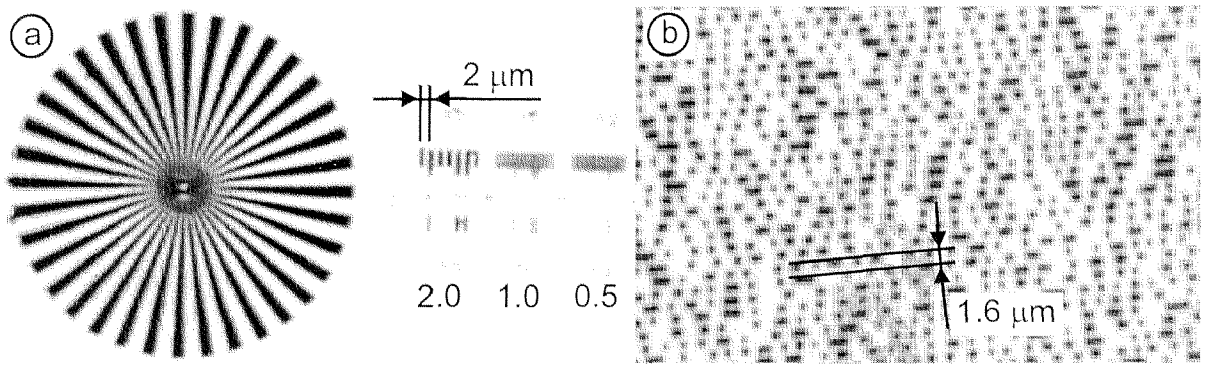


**Fig. 3.9:** *Standard Test target [Oldenburg96] (a) and CD-ROM pits (b) to determine the resolution of global sensor*

### 3.2.4 Materials and Design

A mechanical construction brings both sensor and actuator units together. In detail, the light microscope and the AFM head are mounted on the z coarse positioning stage. A light and stiff construction of these parts is absolutely necessary to keep the resonance frequencies of the structure high and thus guarantee the proper functioning of the whole system. Additionally, the xy-stage has to be integrated into the system.

One possibility would be a special construction made of Invar steel with a fixed assembly of all the components. We decided to choose a different approach. Our system must have a modular concept, meaning that we can easily exchange the type of xy-positioning device or the kind of local sensor while keeping the other elements. Furthermore, the whole system is designed to inspect integrated circuits in an industrial environment. Therefore, a framework made out of standard aluminium profiles (Lagerprofil 80 x 80 from Item, Solingen, Germany) was chosen. This framework can easily be adapted to different purposes and yields enough stiffness to resolve the topographical and electrical surface properties of integrated circuits (fig. 3.10).

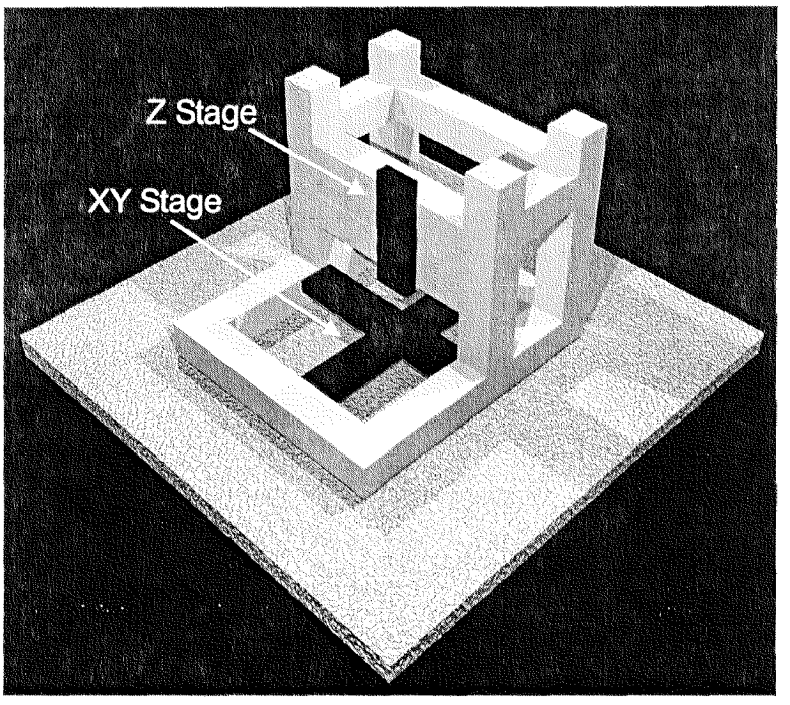


**Fig. 3.10:** *Schematic view of the aluminium framework*

All parts of the setup (fig. 3.11) are either made of aluminium or Macor (table 3.5). Both materials are ideal for light constructions. Macor is preferred in parts that must be insulators or must have a low thermal expansion. For this reason the AFM scanner is manufactured out of Macor.

| Property | Aluminium | Macor |
|---|---|---|
| Density | 2.7 g/cm$^3$ | 2.52 g/cm$^3$ |
| Young's Modulus | 71 000 N/mm$^2$ | 64 000 N/mm$^2$ |
| Thermal Conductivity | 221.5 W/mK | 1.46 W/mK |
| Coefficient of Expansion | 23.8 $10^{-6}$ K$^{-1}$ | 9.3 · $10^{-6}$ K$^{-1}$ |

**Tab. 3.5:** *Mechanical properties of the chosen materials at room temperature*

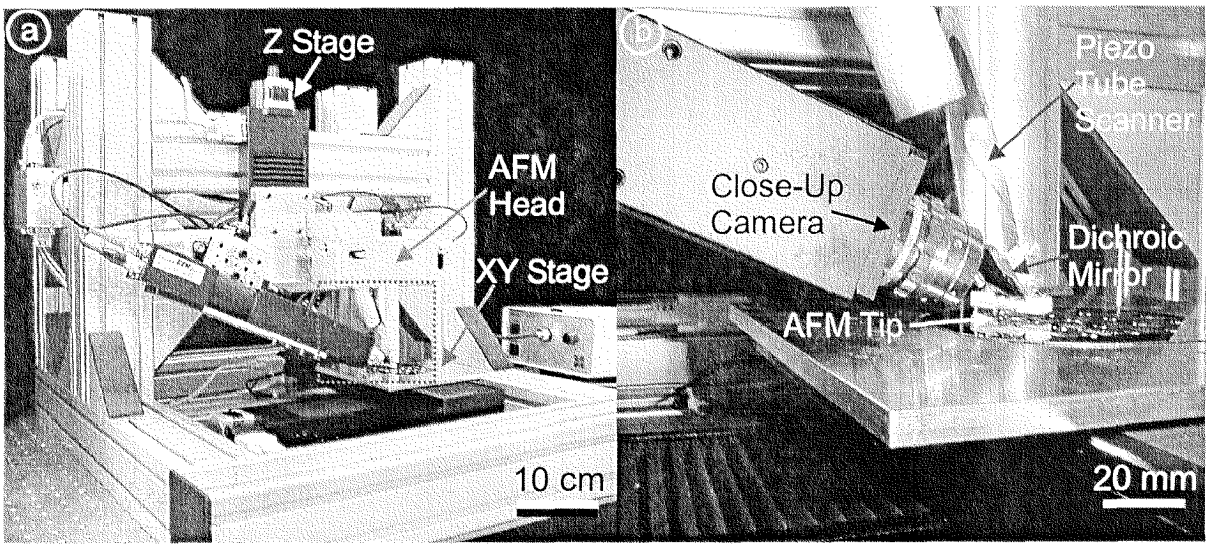


**Fig. 3.11:** *Final structure of the sensor-guided nanorobot (a) and close view on measuring point (b)*

## 3.3 Electronic Components

### 3.3.1 General Overview

The mechanical setup discussed in section 3.2 is completed with an electronic subsystem to obtain the necessary functions. In general, we decided to build the components ourselves for reasons of flexibility, to gain easy access to all signals, to enable quick modification of components and to permit expansion of the system with further functions. All electronic parts are designed as slot-cards fitting to a self-designed bus system. This bus is split up in a digital and an analog section which prevents interferences between digital and analog signals. The advantage of such a concept is the simplicity of extending the system for operation with other functions and modules that use existing signals.

Fig. 3.12 shows an overview of the integrated cards. The entire system is connected to a computer. We decided to use a standard personal computer (PC) owing to the fact that it is inexpensive and that there is a variety of available slot-cards. Furthermore, a standard operating system provides a graphical user interface. Several slot-cards are added for data input/output. A frame grabber card is used to connect up to 4 CCD cameras. A stepping motor card can drive up to 3

motors in either full-step, half-step or micro-step mode. A general input/output (IO) card with digital-analog (DA), analog-digital (AD) and digital input/output (DIO) channels is attached. A digital signal processor (DSP) board is integrated with its own micro processor and IO channels. This solution allows time-critical tasks to be run under a real-time operating system independent of the host computer.

The high voltage (HV) amplifier boosts the fine positioning signals from the DSP card and applies them to the piezo tube scanner. The DSP interface card includes a signal multiplexer (MUX) and DA-converters. The controller card hosts 3 PI-controllers for closed-loop control needed for AFM measurement techniques. Furthermore, the card includes an RMS element for signal conditioning and 2 lock-in amplifiers for signal filtering. Finally, a synthesizer card with 4 independent channels is available. Detailed information about all mentioned components can be found in the following sections.

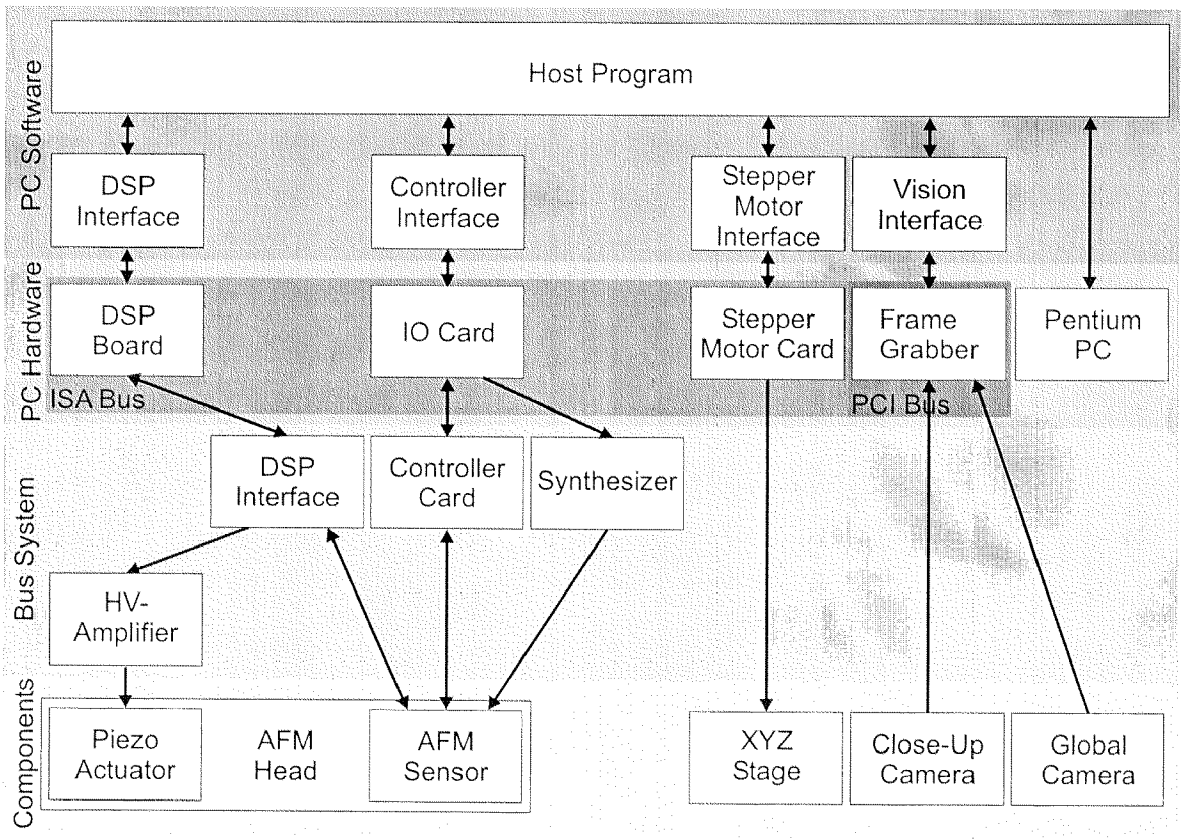


**Fig. 3.12:** *Modular concept of the hard- and software*

### 3.3.2 HV-Amplifiers

The HV-amplifier is used to boost the positioning signals from the DSP board in the range of ±10 Volt to the high voltage of ±220 Volt. We use operational amplifiers (PA88 from Apex) to achieve the required gain. In the interest of flexibility the circuit can handle both types of fine positioning devices, i.e. with separate piezo tubes for xy- and z-movement or with a single tube for all movements (fig. 3.2). Depending on the type of piezo scanner a jumper is used to add the z-positioning signal to the x- and y-component [Kraus91] or supplying the signal to an individual channel (fig. 3.13).

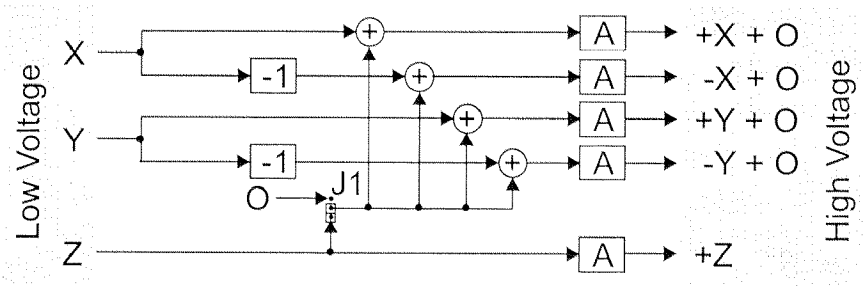


**Fig. 3.13:** *Schematics of the high voltage amplifier. Jumper J1 can toggle between O=Z and O=0 V*

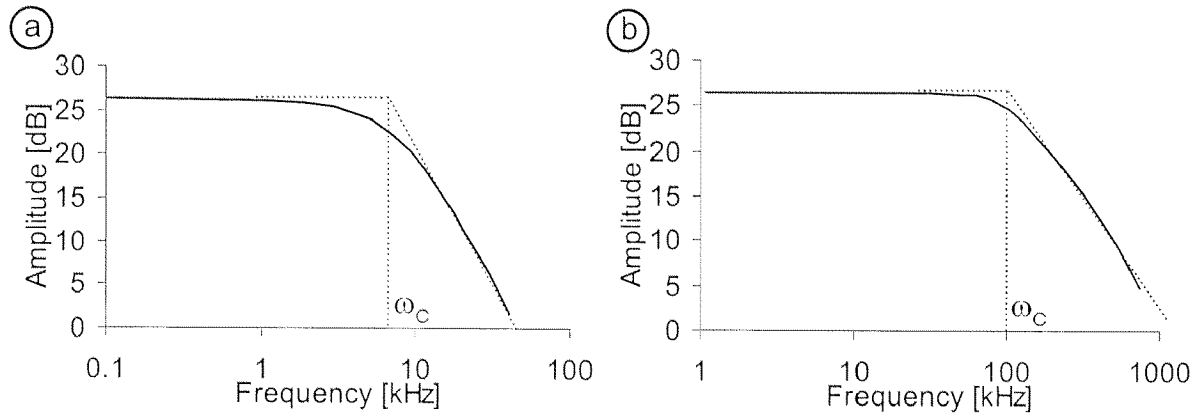


**Fig. 3.14:** *Measured gain response of HV amplifier on x/y-channels (a) and z-channel (b)*

The x/y-channels have a cut-off frequency $\omega_c$ of 5 kHz which is chosen to get enough bandwidth and low noise on the slow positioning signals. The z-channel has a higher bandwidth with a cut-off frequency of 100 kHz. This allows the sys-

tem to be extended to use with other tip-sample distance controllers (e.g. $H_\infty$-controller [Morari89] instead of PID-controller) which need higher dynamics to enable faster scanning movements (fig. 3.14).

### 3.3.3 Synthesizer Card

SPM measurement techniques often require oscillating signals. One example is the tapping mode in which the AFM tip is excited at its resonance frequency. In this application the exact adjustment of the frequency $\omega$ and the amplitude $\tilde{A}$ is important for good measurement results. Also in the Kelvin mode (see section 3.4.2), oscillating signals are needed to modulate the potential applied to the tip as well as to run the lock-in amplifier. In this operation, the exact setting of the phase $\varphi$ is important. The synthesizer card includes 4 oscillators which can be programmed to output signals according to eq. 3.17.

$$f(t) = \tilde{A}\sin(\omega t + \varphi) \tag{3.17}$$

An oscillator chip (AD9850 from Analog Devices) is running with a clock frequency of 32 MHz. The output frequency can be programmed with 32 bit precision allowing us to change it in steps of $7.5 \cdot 10^{-3}$ Hz. To get better signal shapes, frequency was limited to the range of 0 - 2.5 MHz. The phase can be varied with 5 bit resolution, enabling a minimal phase step of 11.5° in the range of 0 - 360°. The remaining parameters of each channel are summarized in table 3.6.

| Channel No. | 0 | 1 | 2 | 3 |
|---|---|---|---|---|
| Amplitude Range | 0 - 16 Vpp | 0 - 16 Vpp | 0 - 2 Vpp | 0 - 16 Vpp |
| Min. Amplitude Step | $3.9 \cdot 10^{-3}$ Vpp | $3.9 \cdot 10^{-3}$ Vpp | $4.9 \cdot 10^{-4}$ Vpp | $3.9 \cdot 10^{-3}$ Vpp |
| Usage | Lock-In 1 Reference | Lock-In 2 Reference | Tapping Excitation | Kelvin Modulation |

**Tab. 3.6:** *Numerical properties of the oscillator channels*

### 3.3.4 DSP Interface Card

The DSP interface card connects the DSP slot card inside the host computer with the bus system. Due to the limited number of analog output channels on the DSP slot card, the interface card also hosts a multiplexer (74ALS138 from Texas Intruments) to split one analog output channels into 4 independent channels and adds further analog output channels over a 16 bit DA converter (DAC712P from Burr-Brown). The whole multiplexer setup can be configured according to user needs (fig. 3.15). For example, the system can have one fast (without MUX) channel for the z-position and two slower (with MUX) channels for the xy-positioning signals.

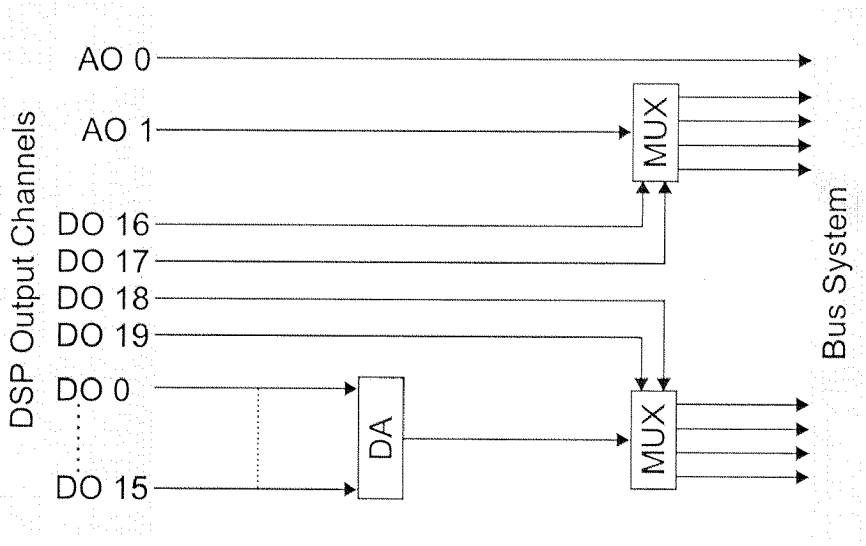


**Fig. 3.15:** *Schematics of the programmable multiplexer where DO 16 - 19 are used to select the output channel*

### 3.3.5 Controller Card

The controller card is used for the different measurement methods of the AFM sensor (see section 3.4.2). In principle the modulated measurement signal from the quadrant detector is processed and fed into a controller. In the tapping mode, the oscillating deflection signal of the tip vibrating at its resonance frequency is measured and the RMS value is determined. The controller adjusts the z-position output according to a defined amplitude reduction and hence acquires the topography information of the surface. In Kelvin mode, an AC potential plus DC offset is applied to the tip and the detector signal is fed into a lock-in amplifier to get

the response at the modulation frequency. This signal is then used by the controller to adjust the tip's DC potential to zero the potential difference between tip and surface. In this way the surface potential is measured.

3 PI controllers were implemented on the controller card. The first is provided with an RMS signal preprocessing unit and used for the topography measurement. The others are furnished with lock-in amplifiers of which one is used for surface potential measurements and the other is free for future applications. Fig. 3.16 shows the basic working mechanism of a lock-in amplifier. The input signal that is a superposition of signals with different frequencies is multiplied with a reference signal. After low-pass filtering, the signal component of interest at the reference frequency is output. The result of a lock-in amplifier is similar to a very thin band-pass filter. With this technique, the signal of interest can very well be separated from other signal components such as noise and power-line hum.

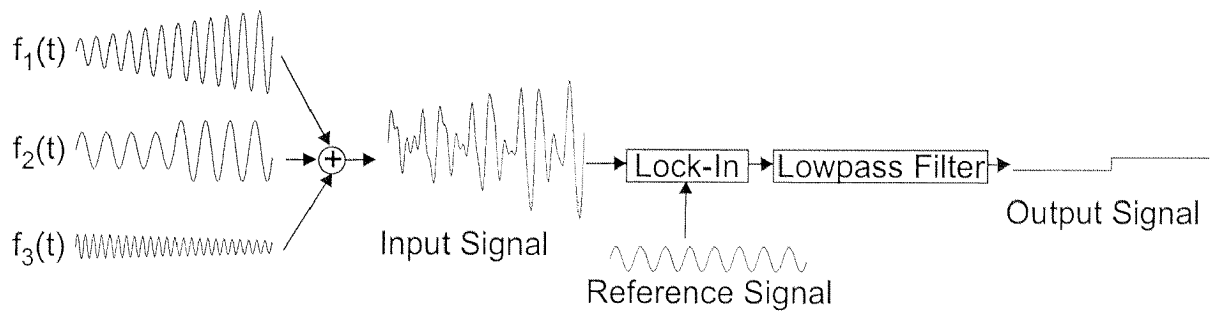


**Fig. 3.16:** *Working principle of lock-in amplifier: the input signal, which is a superposition of several modulated signal, is processed and the component to a given reference signal is output*

### 3.3.6 Computer System and Installed Slot Cards

The electronic setup is completed with a computer system. The host computer runs with a standard central processing unit (CPU) (Intel Pentium at 200 MHz) and is extended with different slot cards connected to the ISA or the PCI bus.

To drive the coarse positioning stages a stepper motor card (SM30 from Owis GmbH, Staufen, Germany) is installed on the ISA bus. This card can drive up to 3 stepper motors in open loop mode and is able to interpolate a full-step of the motor in 64 micro-steps. The stepper motor card hosts its own processor enabling the system to position with individual acceleration and velocity for each channel

without any further interactions with the host processor after receiving a command.

In addition, a IO-Card (ADIODA-12 extended from Messcomp GmbH, Wasserburg, Germany) is connected to the ISA bus. The card features 32 AD, 4 DA and 24 DIO channels and is used for general, non-critical control tasks like controller set point definition or programming of the synthesizer card.

To run time-critical tasks independently of the host computer a DSP board (Fulcrum DT3808 from Data Translation) is plugged to the ISA bus. DSP programs can be loaded on the board and run under a real-time operating system (SPOX from Data Translation). Furthermore, the board is equipped with 16 AD, 2 DA and 20 DIO channels and used to control the whole AFM head.

Finally, a frame grabber card (Picport Stereo H4D from Leutron Vision, Glattbrugg, Switzerland) is plugged to the PCI bus that allows to connect up to 4 CCD cameras. This card enables the cameras to be run in different modes, i.e. normal video mode with 50 interlaced frames per second or full frame mode with 25 or 50 non-interlaced frames per second. In addition, the frame grabber features special operation modes e.g. a pixel synchronous mode to prevent pixel jitter or long integration time for low intensity images.

## 3.4 Software

### 3.4.1 General Overview

Fig. 3.17 displays the hierarchical structure of the software components. In detail, the DSP software is responsible for the control of the AFM head as well as for processing the local sensor signals. Over a communication channel both DSP program and host program can exchange data. At the top of the whole structure the user can interact with the system via the graphical user interface (GUI) of the host computer.

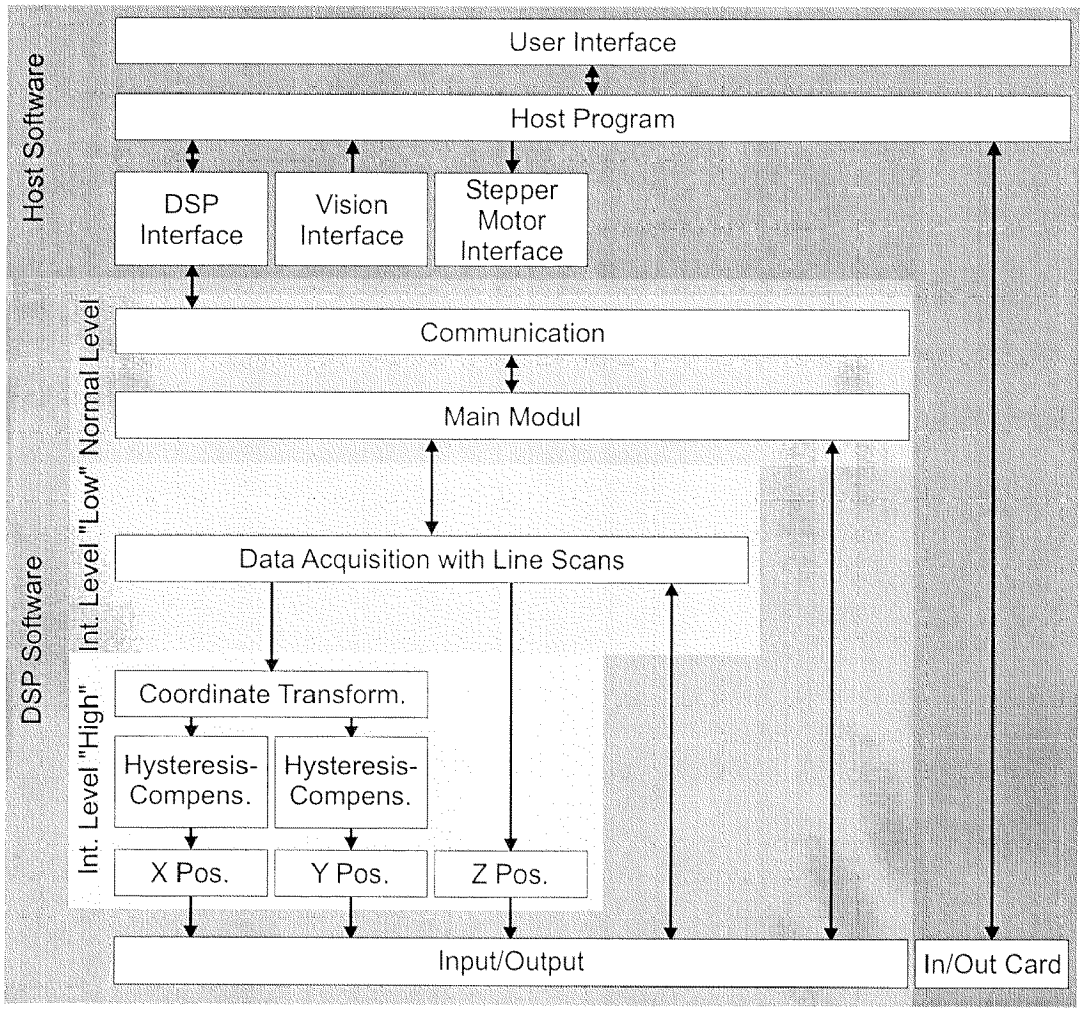


**Fig. 3.17:** *Software component overview and information flow between them*

*DSP Software*

The DSP board can be programmed with the standard C language syntax (DSP Lab from Data Translation). The program is run in different priority levels, namely two interrupt levels and the normal level, to enable quasi-parallel processing of multiple tasks. The lowest interrupt level is running with the highest frequency and is responsible for the fine position calculation. This includes the coordinate transformation, the hysteresis compensation for the x- and y- axis as well as the voltage output.

The other interrupt task makes use of the underlying position calculation to generate line scans for data acquisition. A sequence of point coordinates representing a line scan is calculated and passed to the underlying level that moves the local

sensor to each position to acquire the local sensor information at this point. This working principle is different from commercially available systems which generate the position information by calculating a voltage slope and directly output this value to the high voltage amplifier. Our approach is more suitable for a robot system because we get the full flexibility to freely position the local sensor tip.

The normal program level is responsible for the communication between host and DSP program as well as to process the commands from the user. This is done by splitting up the commands (e.g. acquisition of an AFM image or tracking along a user-defined structure) into single scan lines that will be processed in the underlying interrupt levels.

*Host Software*

The host program on the other hand is implemented in the object-oriented language C++ (Visual C++ from Microsoft) applying standard libraries for programming of the graphical interface (Microsoft Foundation Class MFC from Microsoft). The mechanical and electronic components (e.g. the coarse positioning stage, the video sensor, the AFM head, etc.) are represented in individual C++ objects to guarantee a modular design on the software side as well. Based on these objects, further software modules are implemented in which necessary functions are at the programmer's disposal. A detailed discussion of these functions can be found in the next section. The software concept allows one to easily expand the system with new functions and operational modes as well as to exchange certain software objects by different ones.

### 3.4.2 Necessary Functions for AFM Measurement Modes

*Implementation of AFM Data Acquisition Modes*

To acquire local sample properties software modules with the necessary AFM measurement techniques [Binnig86, Colton98] have to be implemented. On the one hand, the tapping mode [Zhong93, Burnham97] is applied to gain the topological information of the surface (fig. 3.18 a). The AFM cantilever is excited at its resonance frequency $\omega_c$ (typically 250 to 350 kHz). Near the surface the oscillation amplitude is decreased due to surface interactions. A quadrant-detector measures the vertical deflection signal of the cantilever. An RMS element transforms this sensor output to the effective value that is then used to control the z-position of the tip mounted on a fine positioning device. On the other hand, the

Kelvin mode [Jacobs97, Jacobs99] is implemented to obtain the surface potential of the sample (fig. 3.18 b). The tip is positioned at a set distance to the surface (typically 15 to 150 nm) and the force due to the electrostatic interactions is measured with the detector. A lock-in amplifier (see section 3.3.5) processes the modulated signal to extract the actual cantilever deflection which is then used to control the DC voltage applied to the tip.

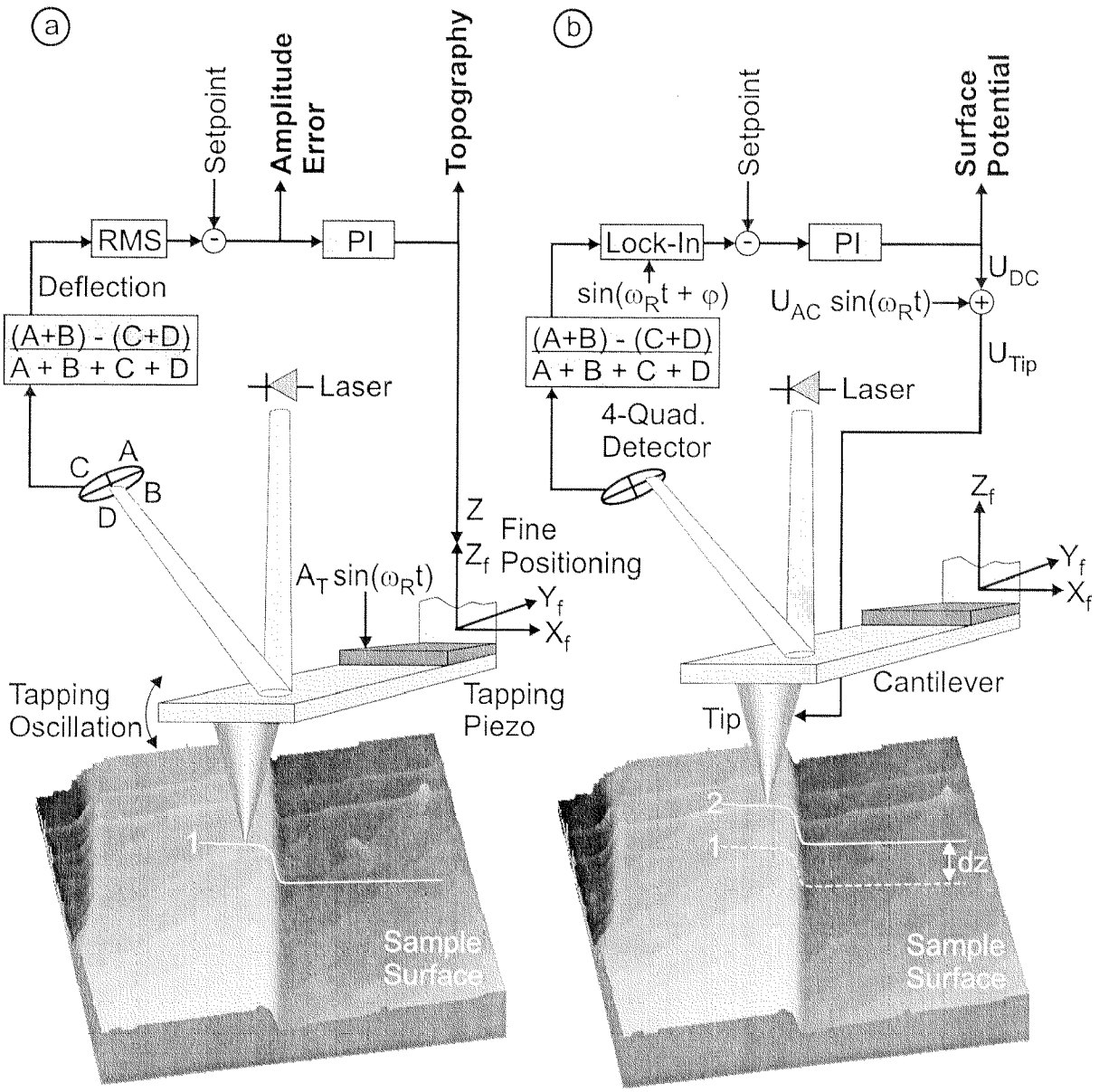


**Fig. 3.18:** *Schematic overview of AFM measurement techniques to acquire the sample topography (a) and the surface potential (b)*

*User Interface*

A graphical interface supports the operator, who often is not that familiar with AFM techniques, to interact with the system (fig. 3.19). Via this interface the operator can obtain information on the local and global sensor inputs, control the coarse and fine positioning devices, and get graphical help while e.g. adjusting the 4-quadrant detector or aligning the laser to the AFM cantilever.

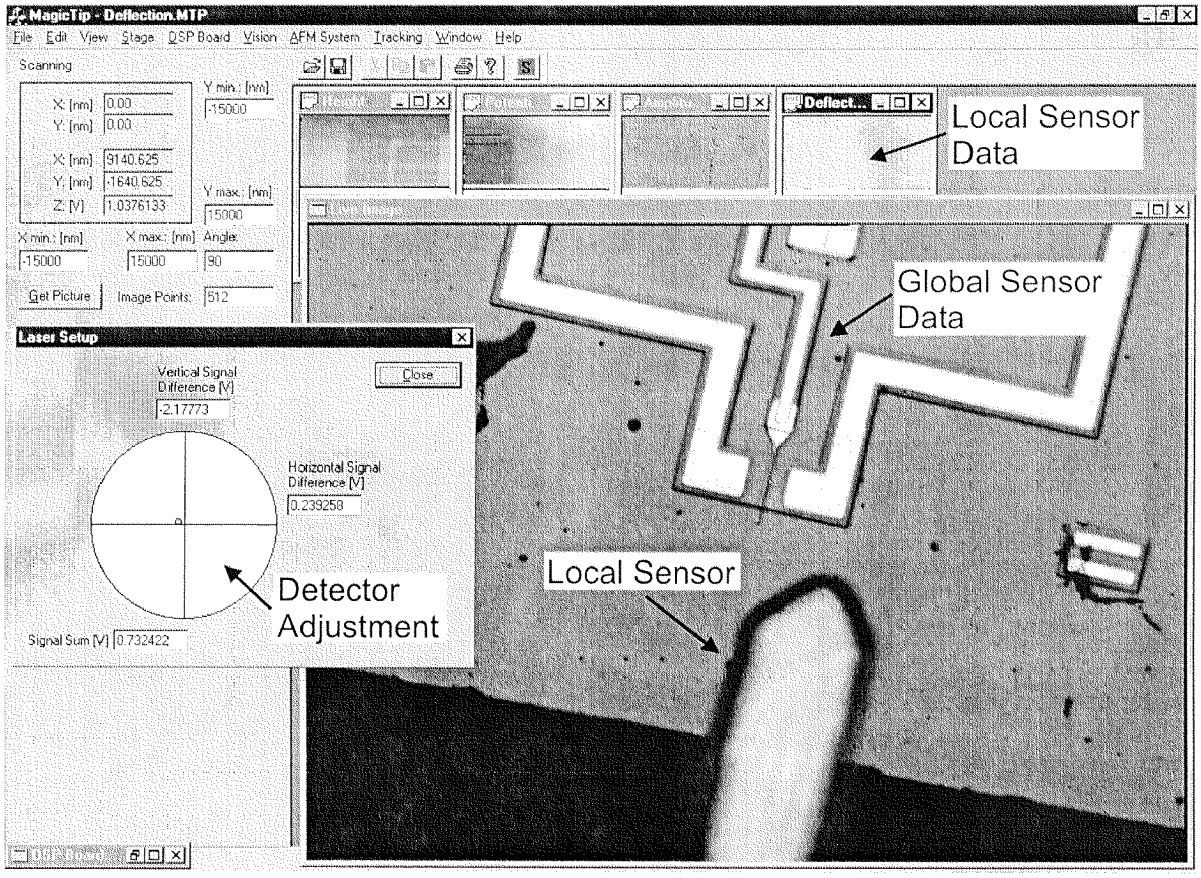


**Fig. 3.19:** *Graphical user interface with windows displaying different sensor output as well as adjustment of quadrant detector*

*Automated Setup of Topography Acquisition*

In addition, some basic preparations and settings have to be made to run the local sensor in AFM mode. First, the tip has to be tuned to find the resonance frequency with which the measurement is performed. The nanorobot can find such a resonance peak automatically by sweeping through a user-defined frequency range (fig. 3.20) and acquiring the tip response. Finding the maximum value

yields the frequency of interest. The system also allows the operator to set the frequency manually or to make changes after the automatic tuning.

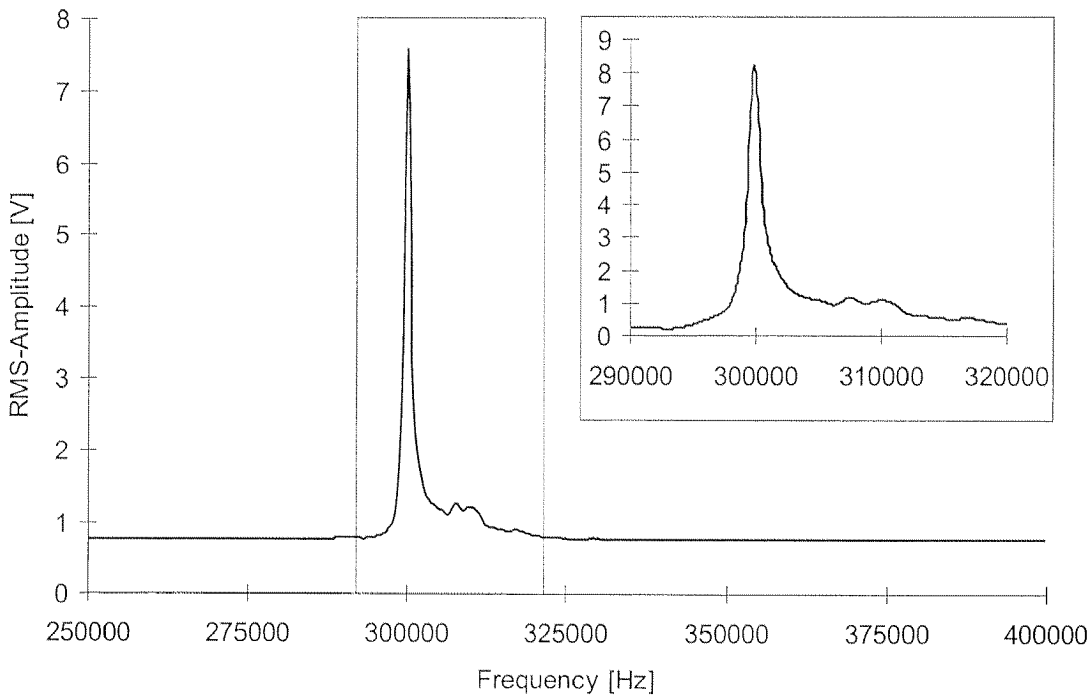


**Fig. 3.20:** *Measured sensor tip response to find its resonance frequency*

*Automatic Tip Approach*

Due to the fact that the xy coarse positioning stage cannot be mounted precisely enough to keep the AFM tip inside its z fine positioning range over the whole xy working range of 150 x 150 mm, the local sensor has to be withdrawn and reengaged from time to time. The nanorobot performs this task automatically by adjusting the z coarse positioning device in such a way that the fine positioning device reaches a middle position. Fig. 3.21 shows the voltage applied to the z-piezo during automatic approach. In a first step the tip is coarsely approached to the surface. After having reached it, the robot moves the stepper motor in fine steps maintaining a constant cantilever deflection until the piezo tube gets inside its target range.

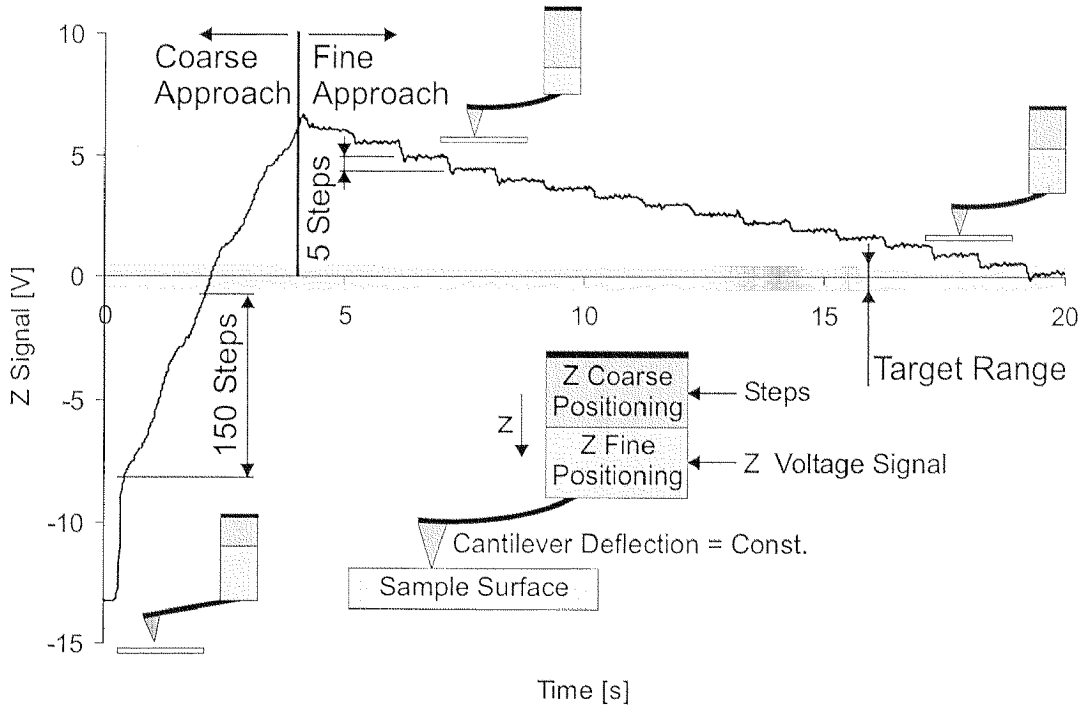


**Fig. 3.21:** *Applied voltage of z-piezo during automatic approach of AFM tip to sample surface*

*Automated Setup of Surface Potential Acquisition*

To acquire the surface potential, some further adjustments of parameters are required. Fig. 3.22 (a) displays the measurement setup for Kelvin mode where the tip is held at a set distance from the sample and a rectangular voltage (b) is applied as test signal to the surface. Depending on the phase offset φ of the reference signal at the lock-in amplifier (fig. 3.18 b), the test signal can be reproduced by the Kelvin mode controller. Hence, the precise setting of this phase is necessary to measure the electric characteristics of a sample. Jacobs discussed the optimization of surface potential measurement [Jacobs98] and summarizes that the output characteristics of the Kelvin mode controller $O_{KM}$ is described according to eq. 3.18 with ϑ denoting the phase shift of the plant. The phase φ can be defined by the user and influences the quality of the measurement (fig. 3.22 c - f).

$$O_{KM} \sim \cos(\vartheta - \varphi) \tag{3.18}$$

The nanorobot measures the signal output in function of the phase φ (fig. 3.23) to find the optimal parameter setting. After finding the maximum in the signal shape the optimal phase value can be found by adding 90° offset. This tuning function allows the operator to set up the Kelvin mode automatically without any further knowledge of this measurement technique.

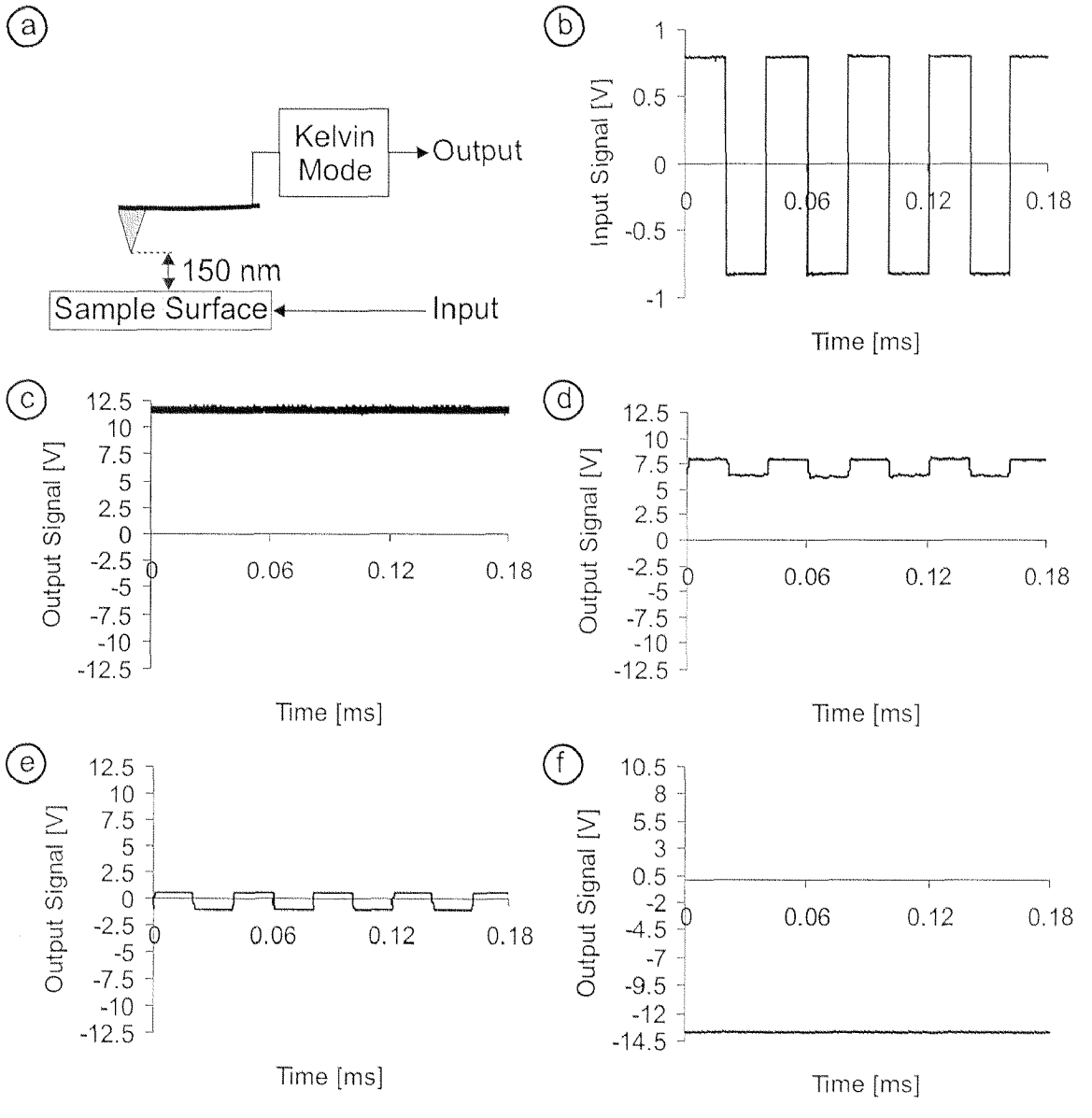


**Fig. 3.22:** *Potential measurement with Kelvin mode at different phase offsets φ with test signal (b) as input and output response at 0° (c), at 90° (d), at 180° (e) and at 270° (f)*

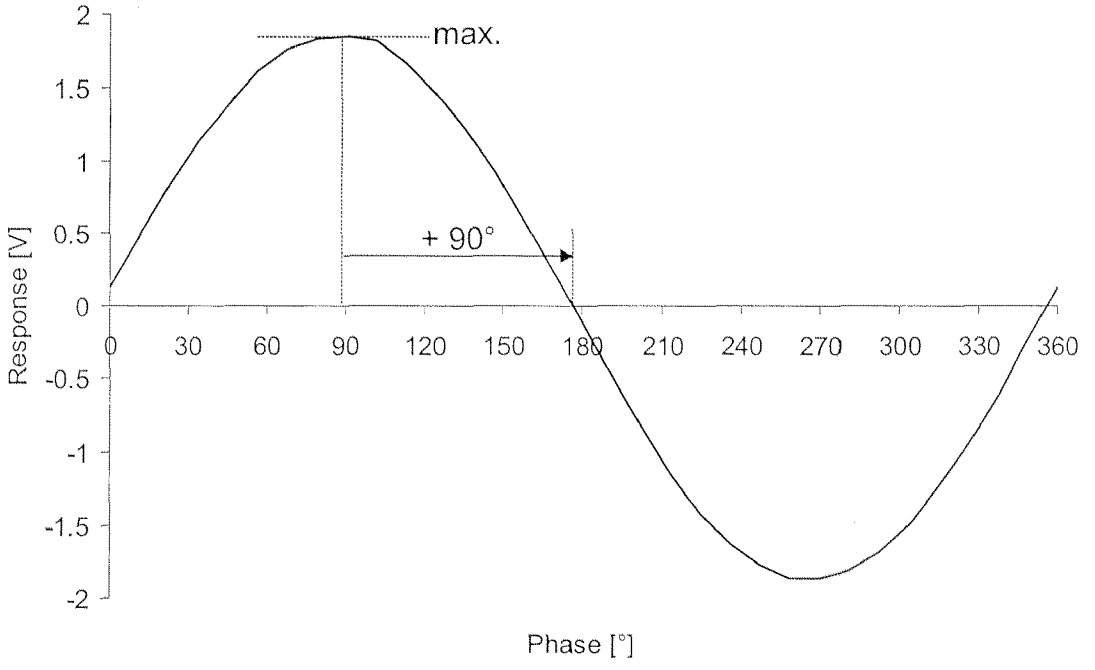


**Fig. 3.23:** *Measured output characteristics of Kelvin mode controller and finding of the optimal phase offset* $\varphi$

*Test of Implemented Functions*

When the AFM measurement modes (i.e. tapping mode for topography measurement and Kelvin mode for surface potential acquisition) are set up properly, the user can start working with the system.

First, the operator can acquire AFM images. Fig. 3.24 displays as an example the topography, the surface potential and the amplitude error of a test sample. The sample consists of a glass plate on which salt crystals are spread. After that a 4 nm thick aluminium coating is vapor-deposited, the salt crystals are washed away leaving a structure with aluminum and glass speckles. These glass spots have a different surface potential that can be seen in the dark regions in the potential image (c). Furthermore, the topography images (b) show that not all salt crystals have been washed away. All AFM images (a - c) exhibit the nature of SPM measurement techniques using a raster motion to acquire data. Such sensor signal can have short-time break-downs and sudden changes resulting in disturbance lines in the images. Hence, such variations in the sensor performance have to be considered when using these signals as controller inputs.

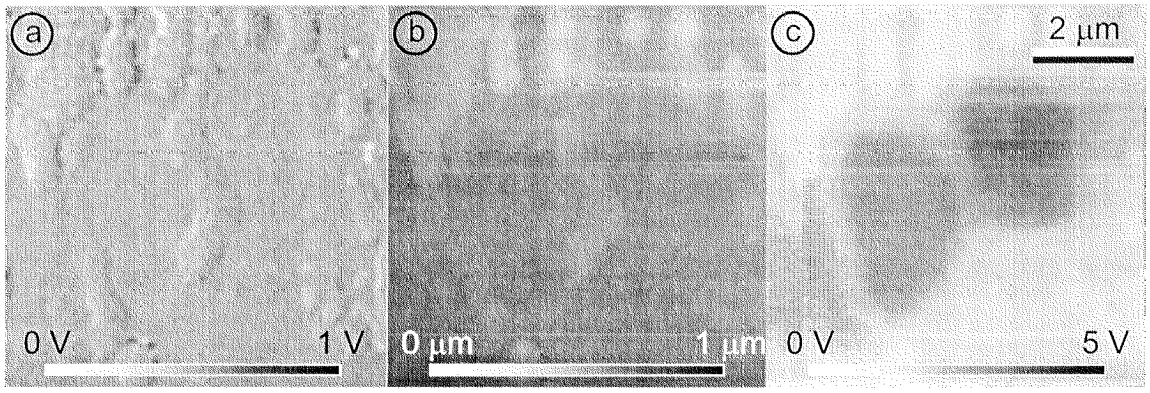


**Fig. 3.24:** *AFM image of test sample including amplitude error signals (fig. 3.18) (a), topography (b) as well as surface potential (c)*

Second, the operator can start the automatic feature tracking mode described in chapter 4 by calling the necessary dialog (fig. 3.25). Along this GUI the user defines the sample feature e.g. the gate finger of a transistor device and some other tracking parameters to start the automatic data acquisition.

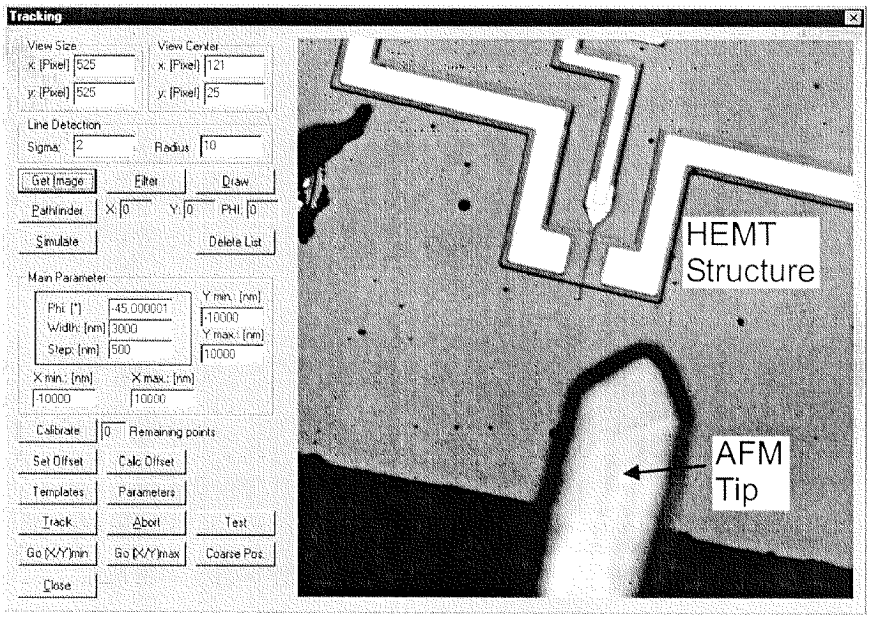


**Fig. 3.25:** *Graphical interface for tracking of user-defined structures e.g. guiding the local sensor (AFM tip) along a gate finger of a HEMT device*

# 4 Controller Structure

Based on the setup introduced in chapter 3, a controller strategy is presented in this chapter allowing the operator to define tasks which will be executed automatically by the nanorobot. To show an example of a possible implementation, the tracking of IC structures is discussed in details. The user defines the feature of interest according to his a-priori knowledge about the geometry and the system searches for the feature to track by comparing the actually measured sensor signals with the user specified structure properties. During tracking, the feature characteristics, i.e. topography and surface potential, are recorded for further analysis, e.g. to find regions that must be redesigned.

## 4.1 General Controller Strategy

### 4.1.1 Overview

To achieve a higher level of automation the controller strategy must support a task-oriented working principle. Such tasks (e.g. tracking along the gate finger on a transistor for analysis) will be defined by the operator and then automatically executed by the robot system. This approach enables us, on the one hand, to split up complex tasks in a sequence of elementary tasks and, on the other hand, to use

already implemented elementary tasks in order to combine them for different analysis problems.

Based on a general architecture in which input signals are processed in a controller to generate an output (fig. 4.1), a new controller strategy will be designed. First, we have to consider that a nanorobot has multiple sensors that measure on different length scales. Local sensor data have nm resolution but a limited field of view due to their proximity to the substrate. Global sensors provide far-field information over a broad range but with low resolution. Consequently, the controller will use both sensor types to gain high resolution and far-field information. Then, the actuators may be split in a coarse and fine positioning device which necessitates to coordinate them in order to position the sample under investigation.

As user-defined tasks mostly are related to a structure (e.g. a transistor or a circuit path), the sensor inputs must first be processed to extract the feature properties. These may be the kind of feature (e.g. path, edge, etc.), its position, its orientation, etc. Based on these properties, a behavior algorithm can be implemented. In a subsequent step, the parameters of the tracking algorithm (e.g. the actual positioning, the tracking direction, the step size, etc.) have to be transformed to a positioning command.

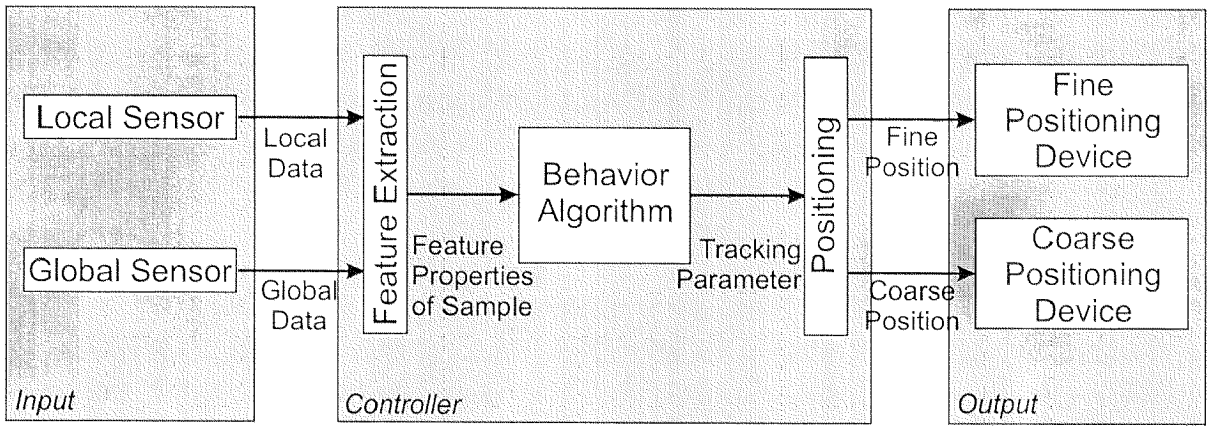


**Fig. 4.1:** *General controller strategy. The user-defined features are located in the sensor inputs. The behavior algorithm uses these properties to calculate a set of new tracking parameters which are then transformed to a positioning command*

In the design of a controller strategy it also has to be considered that signals from local sensors measuring in the nano world are not comparable to data from the

macro world. Local sensors can exhibit short-time break-down of the signal and lose adsorbates can deteriorate the signal quality. In addition, the controller should be capable to handle imperfections of the setup such as drift effects, small errors of positioning devices and localization errors of the feature detection.

### 4.1.2 Implemented Tracking Controller

The controller structure has a cascaded structure: a local signal processing loop running under real-time conditions on the DSP board processes the local information of the AFM tip. An overlaid global signal processing unit, running on the host computer, analyzes the output of the vision sensor and supports the local loop (fig. 4.2).

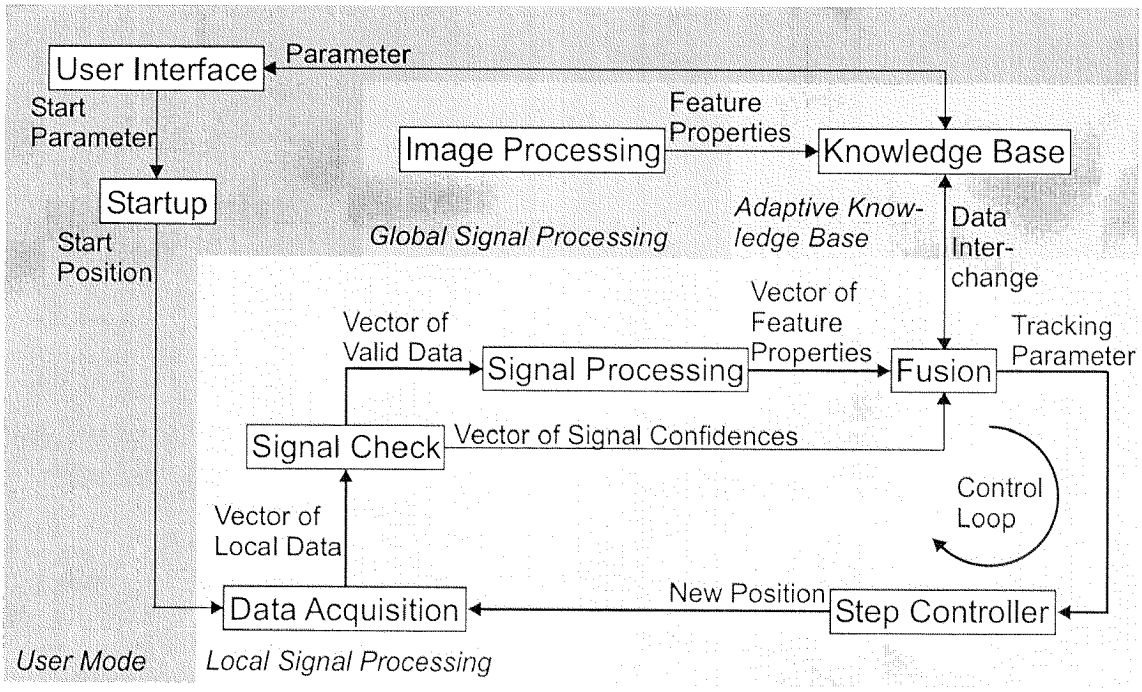


**Fig. 4.2:** *General overview of control structure. In the local signal processing loop the SPM sensor data are processed to extract the feature characteristics and subsequent positioning commands are generated to guide the SPM probe along the structure under investigation. The global image processing supports this local loop by providing additional far-field information. The operator can interact with the controller in user mode by feeding in a-priori knowledge of the structure or changing parameters during tracking*

Through a GUI, the user defines the necessary parameters of the task the system has to perform, e.g. the geometric shape of an IC path to be tracked or the surface potential distribution of a transistor to be analyzed. In the startup phase, the system then locates the feature resulting in a start point for the local signal processing loop. After that data acquisition is started in the local control loop. These data are processed to locate of the user-specified structure within the data set. The step controller calculates the next movement for data acquisition. The acquired information is needed in two ways: on the one hand, the local control loop uses it as sensor input to track the feature and, on the other hand, it is stored for later evaluation of the structure. To support this local loop, a knowledge base stores the previously detected feature positions and interpolates the trajectory. Furthermore, the vision sensor provides additional information about the path trajectory laying ahead.

The control structure can operate in three different modes. In the *local control* mode, the system simply evaluates the local sensor information. In a *semi-automated* mode, the user can interact with the local control loop and change parameters during tracking, e.g. the actual tracking direction or the step size. In the *automatic* mode, the vision sensor replaces the user interactions and the tracking algorithm considers local (from the AFM tip) as well as global information (from the video microscope) to guide the probe along the structure.

## 4.2 One Example of a Tracking Algorithm

In this section, the general approach to a controller strategy for sensor-guided nanorobots will be discussed in detail on the basis of an example. The introduced algorithm allows the user to define a feature to be tracked. Based on geometric data of the structure, the nanorobot can locate it and guide the local probe along the trajectory to acquire topography and surface potential. The discussion is preceded by an overview of necessary coordinate system transformations.

### 4.2.1 Necessary Coordinate System Transformations

In order to combine multiple inputs and outputs, the necessary transformations between the different coordinate systems of the sensor and actuator devices have to be found. The goal is to determine a transformation that compensates possible errors due to non-orthogonal assembly of the test platform, further rotational

errors due to tolerances in the system mounting as well as the scaling between the different measurement units (an overview of possible error sources can be found in [Zesch97b]). In the end, the fine positioning device (index *f*), the coarse positioning mechanism (index *c*) and the vision system (index *p*) are addressed in the same units (fig. 4.3).

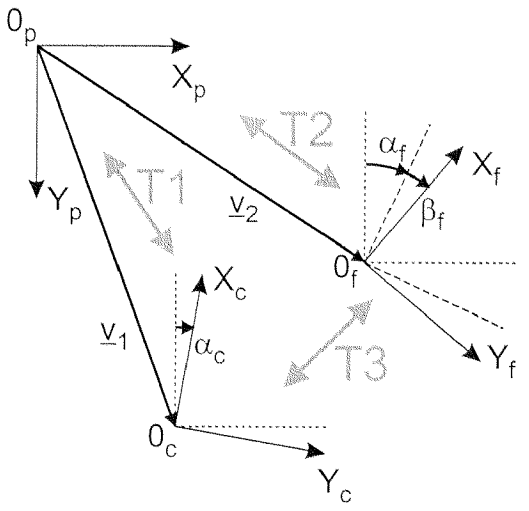


**Fig. 4.3:** *Top view of coordinate systems in the sample plane and their transformations where index p denotes the vision sensor, index f the fine and index c the coarse positioning device*

*Translatory and Rotatory Transformations*

We first discuss the problem of errors due to non-orthogonal coordinate axes of the robot due to imperfection of device assembly or unequal behavior of power electronics for different axes. Assuming that two axes ($x_3$, $y_3$) of a coordinate system are misaligned by the angles $\xi$ and $\chi$ (fig. 4.4) in relation to an orthogonal system ($x_2$, $y_2$), eq. 4.1 transforms the coordinates to an orthogonal system.

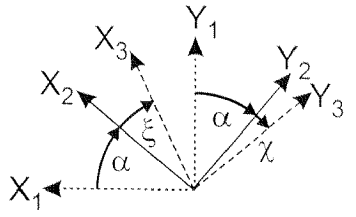


**Fig. 4.4:** *Overview of coordinate system transformations in a plane*

$$\begin{pmatrix} x_2 \\ y_2 \end{pmatrix} = \begin{bmatrix} \cos\xi & -\sin\chi \\ \sin\xi & \cos\chi \end{bmatrix} \begin{pmatrix} x_3 \\ y_3 \end{pmatrix} \tag{4.1}$$

Rotational error between two different orthogonal coordinate systems arise due to imperfect assembly. These angles can be measured and are constant. Eq. 4.2 describes the rotation of a coordinate system with the angle $\alpha$.

$$\begin{pmatrix} x_1 \\ y_1 \end{pmatrix} = \begin{bmatrix} \cos\alpha & -\sin\alpha \\ \sin\alpha & \cos\alpha \end{bmatrix} \begin{pmatrix} x_2 \\ y_2 \end{pmatrix} \tag{4.2}$$

Due to the fact that the manufacturing tolerances are small for a video camera, the vision sensor is used to measure the displacements of the fine (fig. 4.5) and the coarse positioning device (fig. 4.6). These measured positions are interpolated to derive the angles for the transformation matrices.

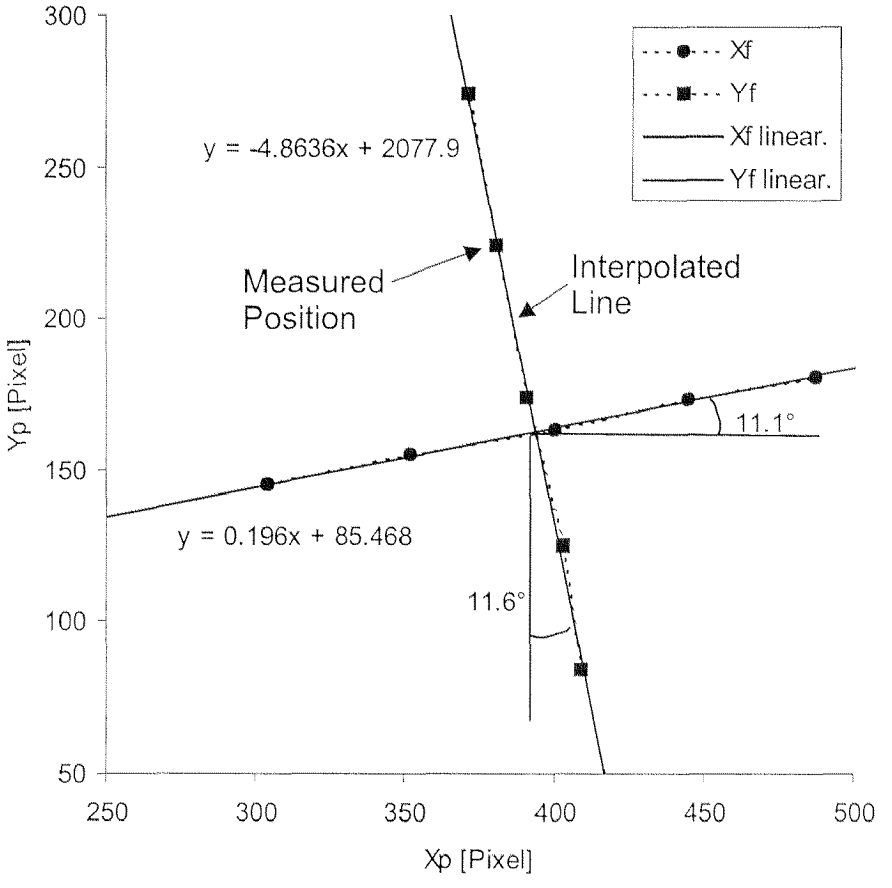


**Fig. 4.5:** *Displacement characteristic of fine positioning device*

The analysis shows that both positioning coordinate systems are to a first approximation orthogonal. The implemented controller will be capable to tolerate the neglected error. Furthermore, we can set the rotational angle $\alpha_c = 2.24$ and $\alpha_f = 11.35$. The angle $\beta_f$ can be set by the user and allows one to rotate the coordinate system of the fine positioning mechanism.

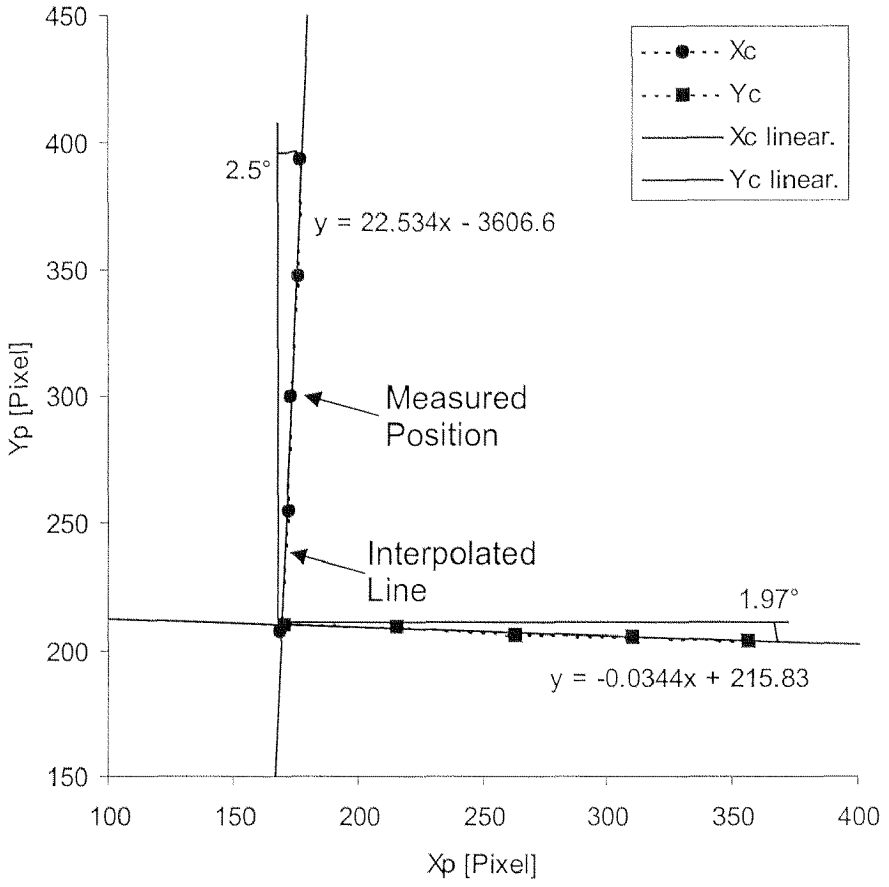


**Fig. 4.6:** *Displacement characteristic of coarse positioning device*

We can now define the transformations $\underline{T}_i$ (eq. 4.3 - eq. 4.5) between the different coordinate systems (fig. 4.3) using a homogenous matrix description [Craig89]. The translations $\underline{v}_1$ and $\underline{v}_2$ depend on the initialization of the positioning devices and have to be determined at each startup using the video sensor (see section 4.2.9).

$$\underline{x}_p = \begin{bmatrix} x_p \\ y_p \\ 1 \end{bmatrix} = \begin{bmatrix} \sin\alpha_c & \cos\alpha_c & v_{1,x} \\ -\cos\alpha_c & \sin\alpha_c & v_{1,y} \\ 0 & 0 & 1 \end{bmatrix} \begin{bmatrix} x_c \\ yc \\ 1 \end{bmatrix} = \underline{\underline{T}}_1 \underline{x}_c \tag{4.3}$$

$$\underline{x}_p = \begin{bmatrix} x_p \\ y_p \\ 1 \end{bmatrix} = \begin{bmatrix} \sin(\alpha_f+\beta_f) & \cos(\alpha_f+\beta_f) & v_{2,x} \\ -\cos(\alpha_f+\beta_f) & \sin(\alpha_f+\beta_f) & v_{2,y} \\ 0 & 0 & 1 \end{bmatrix} \begin{bmatrix} x_f \\ yf \\ 1 \end{bmatrix} = \underline{\underline{T}}_2 \underline{x}_f \tag{4.4}$$

$$\underline{x}_f = \begin{bmatrix} \cos(\alpha_c-\alpha_f-\beta_f) & -\sin(\alpha_c-\alpha_f-\beta_f) & v_{1,x}-v_{2,x} \\ \sin(\alpha_c-\alpha_f-\beta_f) & \cos(\alpha_c-\alpha_f-\beta_f) & v_{1,y}-v_{2,y} \\ 0 & 0 & 1 \end{bmatrix} \begin{bmatrix} x_c \\ y_c \\ 1 \end{bmatrix} = \underline{\underline{T}}_3 \underline{x}_c \tag{4.5}$$

*Scaling*

In a final step all coordinate systems have to be scaled to the same units (e.g. nm). This can easily be done with the transformation eq. 4.6 where $i$ denotes one of the coordinate system indices $p$, $c$ or $f$ [Gonzales93].

$$\underline{x}_{nm} = \begin{bmatrix} x_{nm} \\ y_{nm} \\ 1 \end{bmatrix} = \begin{bmatrix} S_x & 0 & 0 \\ 0 & S_y & 0 \\ 0 & 0 & 1 \end{bmatrix} \begin{bmatrix} x_i \\ y_i \\ 1 \end{bmatrix} = \underline{\underline{S}} \underline{x}_i \tag{4.6}$$

In our case both scaling factors $S_x$ and $S_y$ of each direction are identical. The fine positioning device is already scaled to nm units by the hysteresis compensation. From measurements, the scaling factor of the coarse positioning mechanism was determined to be 37.2 nm/step compared to a theoretical value of 39 nm/step. The scaling factor of the vision sensor is 410 nm/pixel.

### 4.2.2 Startup Procedure

The tracking controller must first locate the structure to be tracked (functional block 'startup' in fig. 4.2). Fig. 4.7 shows the signals that are used to calculate an start point (fig. 4.8 a) for the local control loop.

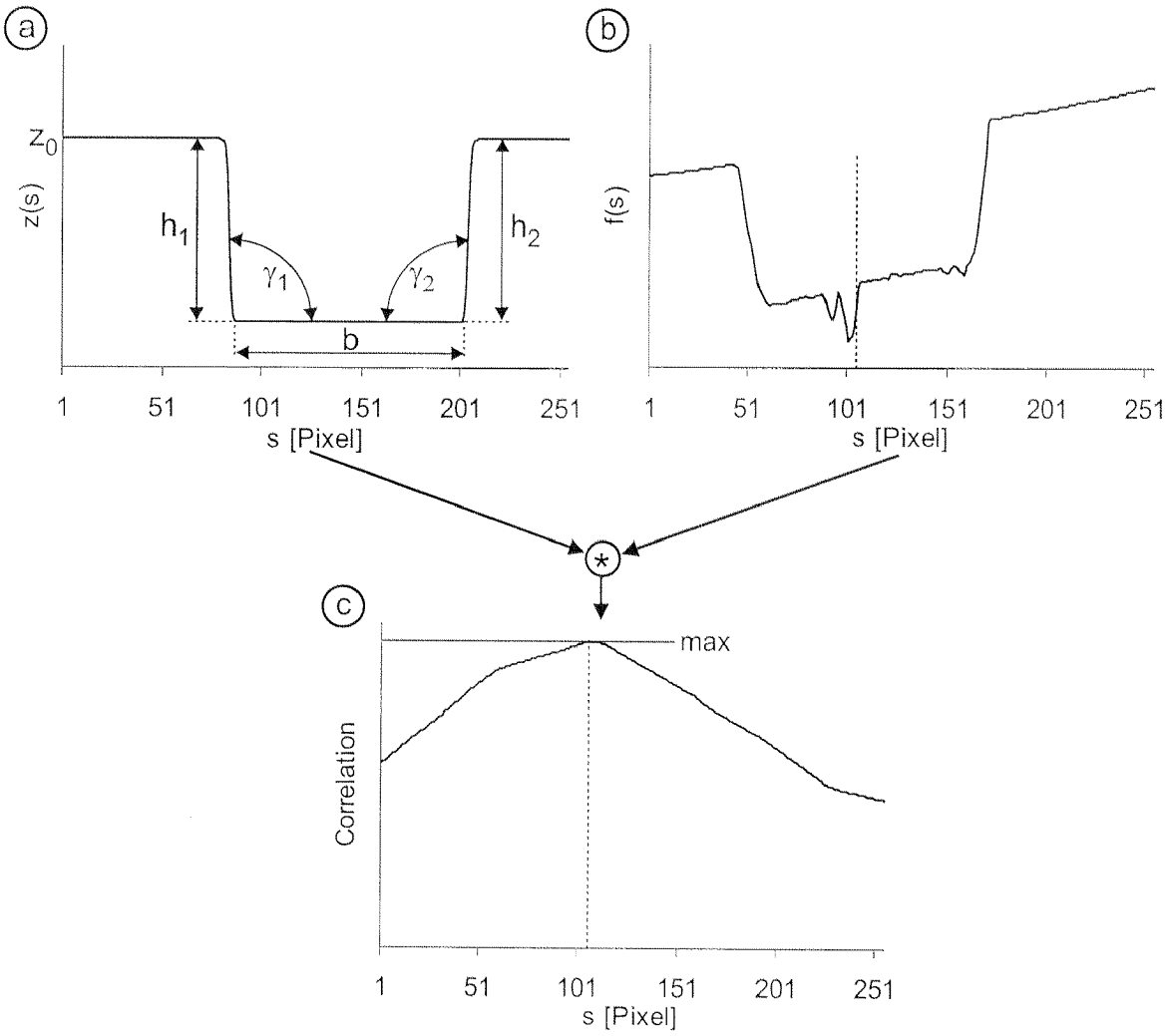


**Fig. 4.7:** *Calculation of starting point based on measured data and a user-specified model*

The operator has to specify a region where to search for the structure (i.e. the start and the end point of the search scan) and the approximate shape of the structure. This is done by defining the parameters for a mathematical representation of the contour e.g. the width $b$, the slopes $\gamma_i$ or the heights $h_i$. As an example, eq. 4.7 represents a line structure shown in fig. 4.7 (a). The advantage of using smooth and steady functions instead of piece-wise linear functions is the fact that the derivative of the mathematical model is a continuous function that can be compared to other signals e.g. the amplitude error of the height controller (fig. 3.18) which resembles the first derivative of the topography signal.

$$z(s) = \frac{h_1}{2}\tanh\left(2\frac{\gamma_1}{h_1}\left(s+\frac{b}{2}\right)\right) + \frac{h_2}{2}\tanh\left(2\frac{\gamma_2}{h_2}\left(s-\frac{b}{2}\right)\right) + 2z_0 + \frac{h_1+h_2}{2} \quad (4.7)$$

The system then preforms search scans (fig. 4.7 (b)) and compares these data $f(s)$ with the calculated shape $z(s)$ (eq. 4.7) [Nalwa86].

$$f(s) \bullet z(s) = \int_{-\infty}^{\infty} f(\alpha)z(s+\alpha)d\alpha \quad (4.8)$$

Finding of the maximum value in the correlation of both signals (eq. 4.8) [Gonzales93, Faugeras93, Ritter96] leads to the best fit of the defined structure inside the region of interest and thus is used as a starting point for the following tracking algorithm.

The concept of searching a feature by calculating a correlation between a measured signal and a model can be applied to any physical data which mainly are topography and surface potential in the current implementation. Combining several signals increases the probability of correct detection. By changing the model (table 4.1), any feature (e.g. edges etc.) can be located. Although all parameters have to be specified by the user, the feature localization produces good results over a large range of values and hence they can usually be approximated by estimates known from the circuit layout or etching process (see section 5.1).

| $h_1$ | $\gamma_1$ | $h_2$ | $\gamma_2$ | $b$ | Feature Shape $z(s)$ |
|---|---|---|---|---|---|
| <0 | >0 | >0 | <0 | >0 | 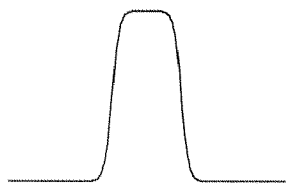 Line Structure |

**Tab. 4.1:** *Different feature shapes and their corresponding parameters*

| $h_1$ | $\gamma_1$ | $h_2$ | $\gamma_2$ | $b$ | Feature Shape $z(s)$ |
|---|---|---|---|---|---|
| <0 | >0 | any | 0 | 0 | 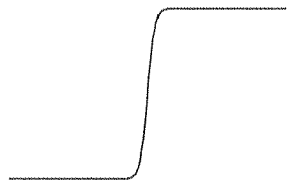 Edge Structure |
| <0 | <0 | any | 0 | 0 | 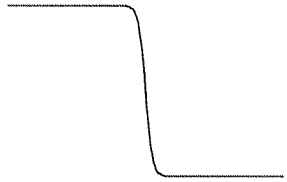 Edge Structure |
| <0 | <0 | >0 | <0 | >0 | 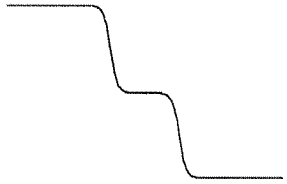 Structure Consisting of Two Edges |

**Tab. 4.1:** *Different feature shapes and their corresponding parameters*

### 4.2.3 Data Acquisition

All SPMs work in a scanning mode by moving a local sensor in line scans across the sample to acquire data. We extend this line scan functionality by allowing free choice of start and end point of each line scan. Fig. 4.8 shows the principle procedure for data acquisition. In a search scan, the structure under investigation (e.g. a IC path) is located. Then, line scans perpendicular to the tracking direction are performed under control of the local control loop to acquire data (functional unit 'data acquisition' in fig. 4.2). This information is stored for further analysis.

Depending on the AFM measurement method, several different signals can be obtained within one line scan. In tapping mode a line scan includes the topography and the controller error signal. When running the system in Kelvin mode, a

line scan contains topography, error signal as well as the surface potential. Consequently we are talking of a vector of local data.

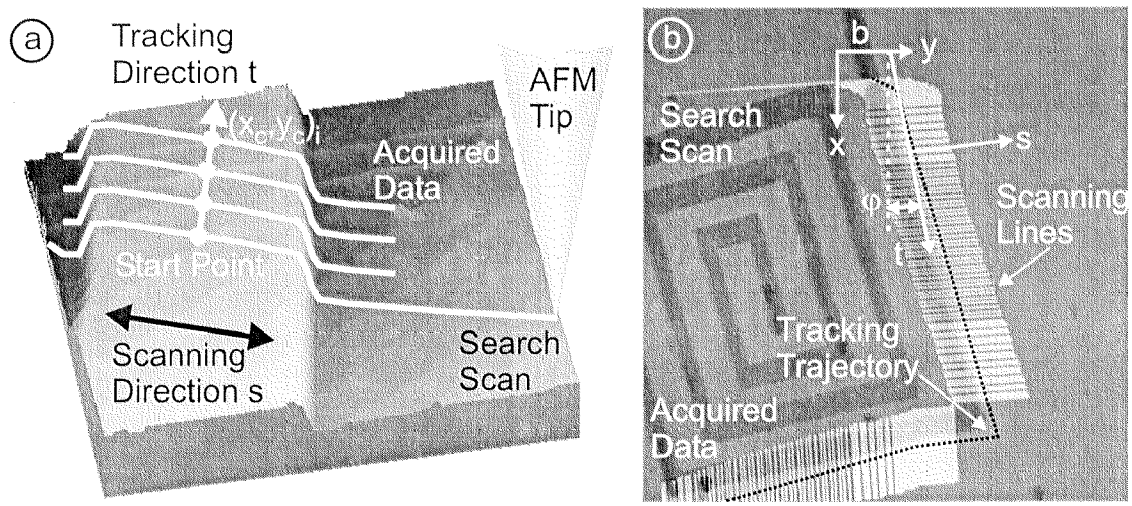


**Fig. 4.8:** *3-dimensional AFM image showing the data acquisition during searching and tracking of a line structure (a). Topography image displaying the feature tracking (b) while s represents the scanning direction and t the perpendicular tracking direction*

### 4.2.4 Signal Checking

Whereas sensitivity and noise of far-field sensors normally are smoothly varying functions with time and, hence, behave in a fairly predictable manner, near-field sensors like our AFM tip may exhibit large variations in performance since their signal transfer characteristics may change suddenly due to alternations of the tip during scanning. For instance, lose adsorbates or dirt particles on the surface affect the resolution of the probe and increase signal noise. Therefore, the sensor data are first checked (module 'signal check' in fig. 4.2) according to a-priori knowledge, i.e. we weighted the amplitude error signal as less reliable than the topography and potential information due to its very strong dependence on noise and system parameters like feedback gains. In detail, the weighting of the amplitude error is normally between 0 - 5 %, whereas the remaining range will be assigned to the topography or in equal parts to topography and surface potential when considering both signal types.

Furthermore, the signals are preprocessed to perform noise reduction and plane offset corrections which are necessary to improve the result of the following

steps. Depending on the applied signal filter, both noise reduction and feature extraction can be combined in one calculation step to reduce computing time and, hence, speed up the system (see section 4.2.5).

The static method actually implemented to describe the signal confidence is based on experience gained during setup and testing of the current platform. This method can easily be adapted to dynamic algorithms like a detector that can find an outlier inside the sensor signal [Pearson98, Menold99] and correct it with a suitable value or algorithm that compares the trace and retrace data signals to derive a value for its confidence.

### 4.2.5 Signal Processing

The sensor-guided nanorobot must automatically track microstructures according to user-made specifications. To compensate possible errors (e.g. drift, etc.), the actual feature position is located at each cycle loop. This feature position is contained in the line scans and an on-line signal processing is used to extract this information of interest (functional block 'signal processing' in fig. 4.2).

Different strategies can be applied to extract a position from a feature inside a measured signal shape. The method of calculating a correlation has already been mentioned. Considering the nature of SPM sensor signals we further need a noise reduction before computing the correlation. Canny proposed a filter design which performs noise reduction and feature detection in one step [Canny86, Accame97]. No further knowledge about the feature is needed. Such Canny filters were employed to reduce the computing effort of the sensor signals considering the fact that the signal evaluation runs in real-time.

To find a filter that has a good detection behavior, i.e. whose localization of the edge is good and that produces only one response to a single edge, Canny uses numerical optimization to derive the shape of such an edge detection filter. An efficient approximation for such filters is described with a first order derivative of a Gaussian function. In other words, a simple Gaussian curve (fig. 4.9 a) (eq. 4.9) will smooth the signal, whereas the first derivative (b) (eq. 4.10) will detect edges and the second derivative (c) (eq. 4.11) will find lines (see table 4.1).

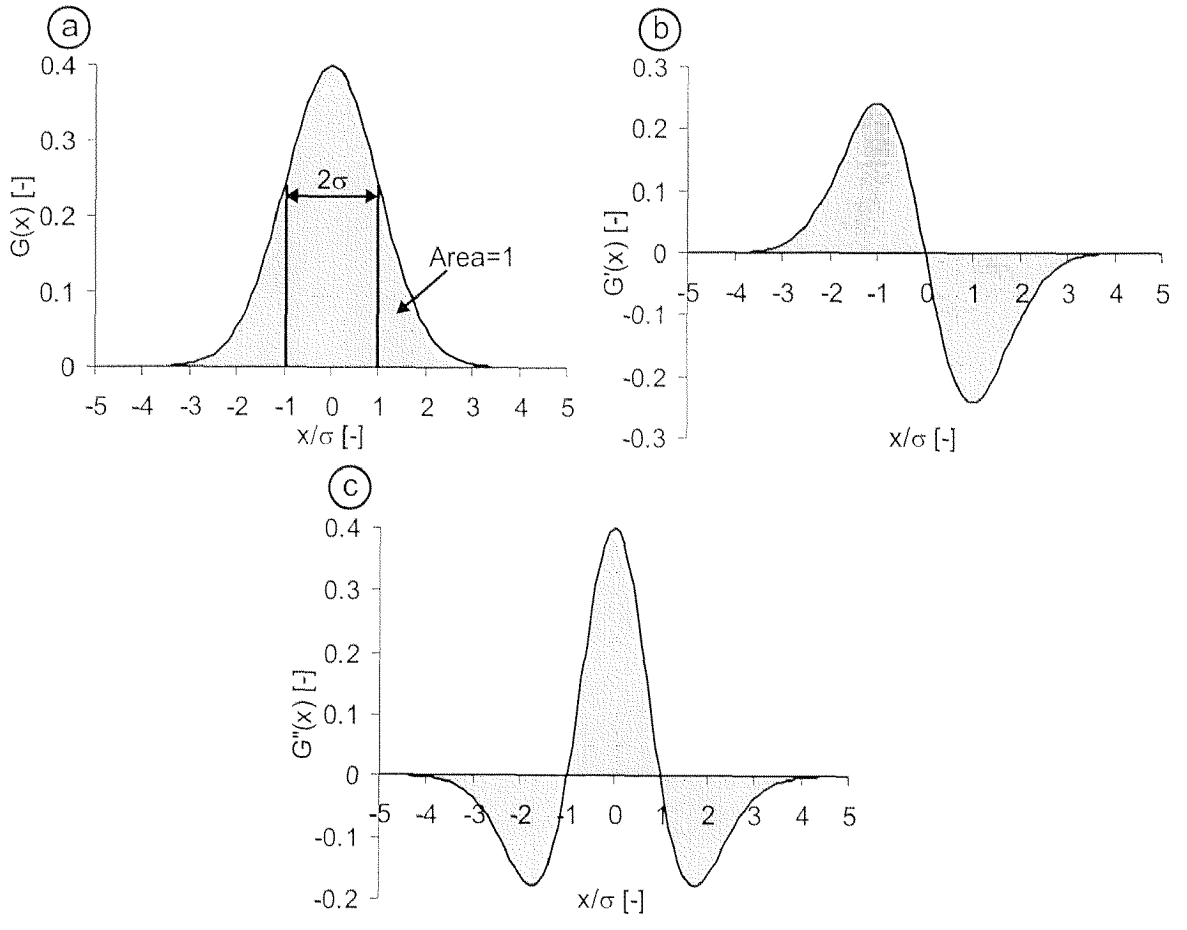


**Fig. 4.9:** *Gaussian curve (a) and its first (b) and second (c) derivative used for Canny filters*

$$G(x) = \frac{1}{\sqrt{2\pi\sigma^2}} e^{-\left(\frac{x^2}{2\sigma^2}\right)} \tag{4.9}$$

$$G'(x) = \frac{dG(x)}{dx} = -\frac{x}{\sqrt{2\pi\sigma^6}} e^{-\left(\frac{x^2}{2\sigma^2}\right)} \tag{4.10}$$

$$G''(x) = \frac{d^2G(x)}{dx^2} = \frac{\sigma^2 - x^2}{\sqrt{2\pi\sigma^{10}}} e^{-\left(\frac{x^2}{2\sigma^2}\right)} \tag{4.11}$$

Fig. 4.10 illustrates the working principle of the filter: the measured signal $f(s)$ (a) is convoluted with filter $g(s)$ (b) resulting in an output (c) (eq. 4.12) [Gonzales93].

$$f(s) \otimes g(s) = \int_{-\infty}^{\infty} f(\alpha) g(s-\alpha) d\alpha \qquad (4.12)$$

The extremum in the output signal indicates the location of the line. Depending on the type of extremum a circuit path on a surface (maximum) or a groove (minimum) is detected.

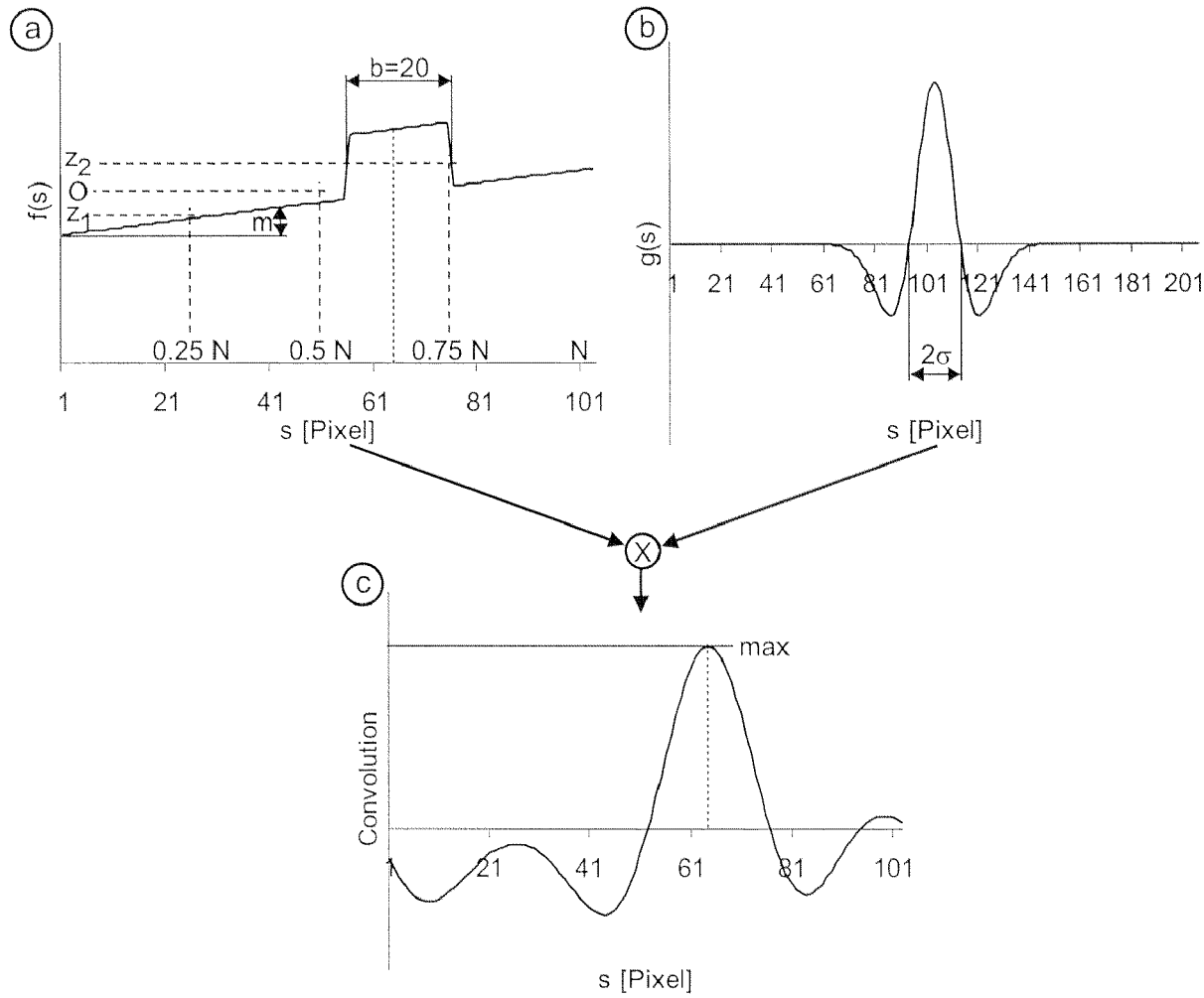


**Fig. 4.10:** *Edge detection according to Canny: The input signal (a) is convoluted with the filter (b) resulting in the output (c)*

Two parameters influence the precision of the filter result. First, the measured signal is superimposed with a slope and an offset which can deteriorate the filter result. Second, the filter parameter $\sigma$ controls the feature size to detect. Fig. 4.11 illustrates the resulting position of the convolution discussed in fig. 4.10 as a function of the slope $m$ of the measured signal and the filter parameter $\sigma$. We can see that the signal processing calculates a good answer in a wide range which can be seen in a flat plane (dark shading). The correct answer of 63 pixel can be found by setting the parameter $\sigma$ to about the half width $b$ of the feature (eq. 4.13).

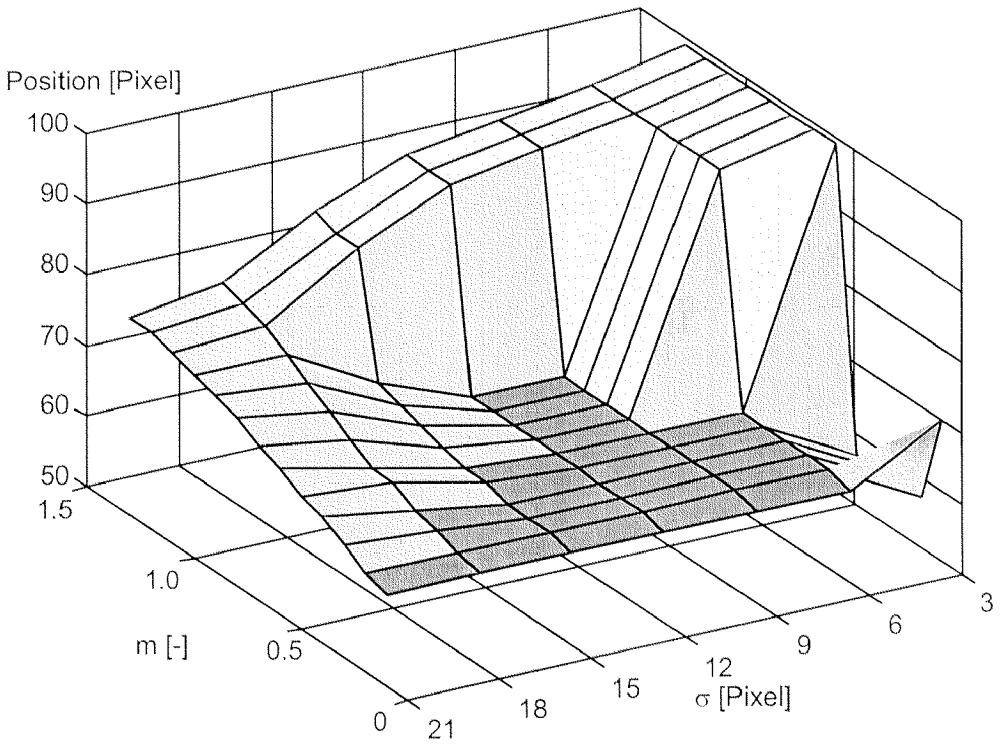


**Fig. 4.11:** *Filter response in function of the input slope m and the filter parameter σ for the example shown in fig. 4.10*

$$\sigma \cong 2b \tag{4.13}$$

Furthermore, it can be seen that the filter result does not vary much for small slopes. We, therefore, suggest a rather simple way to compensate the offset and the slope of the sensor signal. We calculate the mean values of the first ($z_1$) and the second ($z_2$) half of the $N$ data points $z_k$ ($k = 1 \ldots N$) within one line scan. The offset $O$ and the slope $m$ for the compensation is calculated according to eq. 4.14 and eq. 4.15.

$$O = \frac{z_1 + z_2}{2} \tag{4.14}$$

$$m = 2\frac{z_1 + z_2}{N} \tag{4.15}$$

Based on these values the compensated data points $z_{k,\,c}$ are computed (eq. 4.16).

$$z_{k,\,c} = z_k - O - k \cdot m \tag{4.16}$$

We discussed the signal processing step based on the topography information. The proposed concept can easily be adapted to other signals like the surface potential, the deflection of the cantilever or amplitude error of the tip-sample distance controller (fig. 3.18 a). The signal processing step results in a vector of potential feature positions.

### 4.2.6 Fusion

In this step, the potential feature positions $p_{i,\,j}$ of each signal $j$ in every cycle $i$ of the local control loop have to be merged to a single result $p_{i,\,0}$ (module 'fusion' in fig. 4.2). Considering the fact that SPM signals may contain imperfections, not all filter responses have the same quality. Thus, the fusion is performed by evaluating a weighted sum (eq. 4.17).

$$p_{i,\,0} = \sum_j a_{i,\,j} p_{i,\,j} \tag{4.17}$$

The weighting factor $a_{i,\,j}$ is composed of two factors which estimate the quality of the position $p_{i,\,j}$. On the one hand, we consider the signal confidence $c_{i,\,j}$ calculated in the signal checking step (see section 4.2.4) and on the other hand we assume that results that are far away from the tracking trajectory $p_{i,\,c}$ are less reliable than those who are close. Hence, the weighting factor calculates according to eq. 4.18 and eq. 4.19 considering that the sum of all weighting factors must be equal 1.

$$\tilde{a}_{i,\,j} = \frac{c_{i,\,j}}{\left| p_{i,\,j} - p_{i,\,c} \right|} \tag{4.18}$$

$$a_{i,j} = \frac{\tilde{a}_{i,j}}{\sum_j \tilde{a}_{i,j}} \tag{4.19}$$

The fusion result is then transferred to the knowledge base for further calculations. In return, we get the parameters for the actual trajectory.

### 4.2.7 Knowledge Base

To get stability of the local control loop against short-time signal blackouts, we implemented a knowledge base (functional unit 'knowledge base' in fig. 4.2) that stores feature positions extracted from the last $M$ control cycles of the local loop. Based on these data a regression algorithm is applied to extrapolate the future path trajectory. In the current setup, we assume that the trajectory is a line (fig. 4.12). This does not limit the system because we only store the last $M$ data points and, therefore, a direction change will sufficiently be detected. With the parameter $M$ the behavior of the knowledge base can be controlled. The larger the value is chosen, the longer it takes to update a direction. Experiments have shown that a good value of $M$ is 20. However, the interpolation could easily be expanded to a higher order by using splines or polynoms if needed.

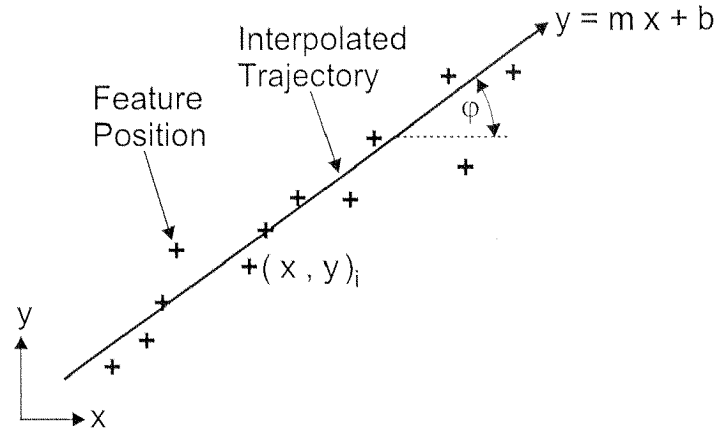


**Fig. 4.12:** *Linear interpolation of found feature positions*

The mathematical problem is to find the parameters of the line $m$ and $b$ which best fit the feature positions $(x, y)_i$ (eq. 4.20).

$$\underline{y} = \begin{bmatrix} y_1 \\ \dots \\ y_i \\ \dots \\ y_M \end{bmatrix} = \begin{bmatrix} x_1 & 1 \\ \dots & 1 \\ x_i & 1 \\ \dots & 1 \\ x_M & 1 \end{bmatrix} \begin{bmatrix} m \\ b \end{bmatrix} = \underline{X} \begin{bmatrix} m \\ b \end{bmatrix} \tag{4.20}$$

The problem is known as least square fit. The solution for $m$ and $b$ can be calculated using the pseudo inverse matrix $\tilde{\underline{X}}^{-1}$ defined in eq. 4.21 [Stoer79].

$$\begin{bmatrix} m \\ b \end{bmatrix} = \tilde{\underline{X}}^{-1} \underline{y} = (\underline{X}^T \underline{X})^{-1} \underline{X}^T \underline{y} \tag{4.21}$$

Besides the parameters $m$ and $b$ for the interpolated trajectory, the knowledge base also stores the actual position of the feature $p_{i,0}$ (see section 4.2.6), the step size $u$, the scan line length as well as the weights for the signal fusion.

The calculated tracking parameters can now be passed on to the fusion module for further tracking based on local information. The knowledge base can also interact with overlaid processes, namely the user or the global image processing. Both the operator and the vision sensor subsystem can communicate with the knowledge base to get the actual values of the parameters or to change them.

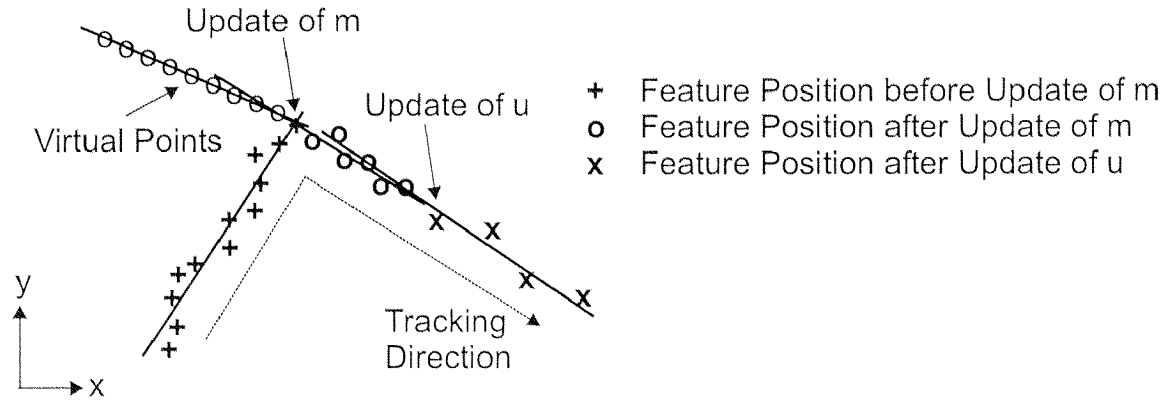


**Fig. 4.13:** *Updating of parameters namely the tracking direction m and the step size u*

Fig. 4.13 displays the situation during the update of parameters in the knowledge base. If the global image processing unit or the operator changes the tracking

direction $m$, the knowledge base is updated by calculating $M$ virtual points lying on the trajectory of the new direction. These points are then modified with the newly found positions in the local control loop to correct changes in direction. The step size $u$ is modified at less critical sections of the trajectory to speed up data acquisition and can be done without calculating new virtual points in the knowledge base.

### 4.2.8 Step Controller

The step controller (functional block 'step controller' in fig. 4.2) completes the local control loop and is designed to transform the actual set of tracking parameters into a new position for the next line scan. We define a scanning direction $\underline{s}_i$ (eq. 4.22) perpendicular to the tracking direction $\underline{t}_i$ (eq. 4.23) (fig. 4.14) based on the calculated parameters of the knowledge base (eq. 4.24).

$$\underline{s}_i = \begin{bmatrix} \cos\theta_i \\ \sin\theta_i \end{bmatrix} = \begin{bmatrix} -\sin\varphi_i \\ \cos\varphi_i \end{bmatrix} \tag{4.22}$$

$$\underline{t}_i = \begin{bmatrix} \cos\varphi_i \\ \sin\varphi_i \end{bmatrix} \tag{4.23}$$

$$m_i = \tan\varphi_i \tag{4.24}$$

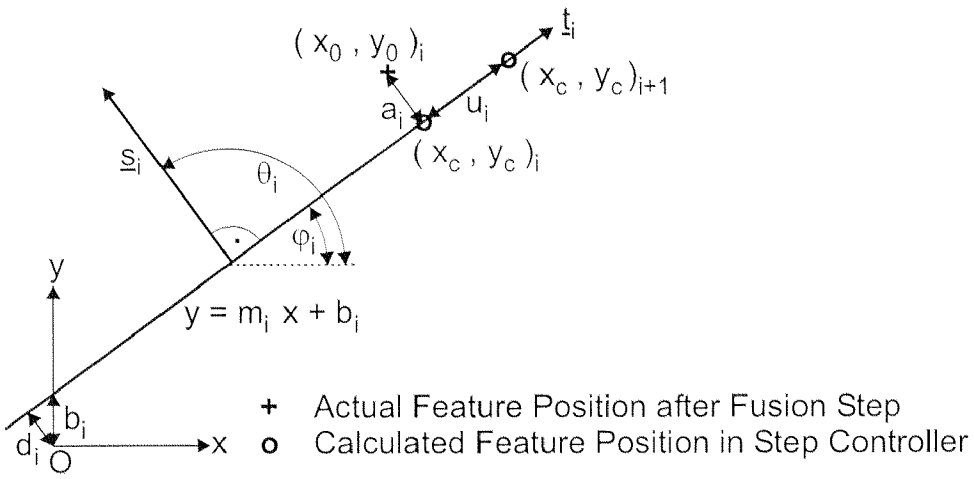


**Fig. 4.14:** *Tracking trajectory and calculated steps for data acquisition (fig. 4.8)*

We then compute the distance $a_i$ of the last feature position $(x_0, y_0)_i$ determined in the fusion step (see section 4.2.6) from the interpolated trajectory obtained from the knowledge base (see section 4.2.7) (eq. 4.25 and eq. 4.26) where $d_i$ denotes the distance of the interpolated trajectory to the origin.

$$a_i = \begin{bmatrix} x_0 \\ y_0 \end{bmatrix}_i \underline{s}_i - d_i \tag{4.25}$$

$$d_i = \begin{bmatrix} 0 \\ b_i \end{bmatrix} \underline{s}_i = b_i \sin\theta_i = b_i \cos\varphi_i \tag{4.26}$$

Once the trajectory point $(x_c, y_c)_i$ has been determined (eq. 4.27), the next step $u_i$ can be performed. This new position $(x_c, y_c)_{i+1}$ (eq. 4.28) is passed to the data acquisition module (see section 4.2.3) to generate the next line scan.

$$\begin{bmatrix} x_c \\ y_c \end{bmatrix}_i = \begin{bmatrix} x_0 \\ y_0 \end{bmatrix}_i - a_i \underline{s}_i \tag{4.27}$$

$$\begin{bmatrix} x_c \\ y_c \end{bmatrix}_{i+1} = \begin{bmatrix} x_c \\ y_c \end{bmatrix}_i + u_i \underline{t}_i \tag{4.28}$$

Apart from the step calculation, the step controller is also responsible for the coordination of fine and coarse positioning device. After calculating the new position, the module compares the coordinates with the overall working range of the fine positioning device. If the new position is outside the working range, the offset in the transformation matrix is recalculated and a coarse position step is performed in order to move the new position into the middle of the fine positioning range. In the current setup, the coarse positioning step is done in open-loop mode which has proved to be precise enough to run the robot system properly. The precision of the stepper motors is sufficient not to lose the tracked feature during repositioning. With different coarse positioning devices, problems may arise by losing the feature to track. In such cases, a search scan (see section 4.2.2) could automatically be initiated to relocate the structure and get a new start point for tracking.

### 4.2.9 Image Processing

To run the sensor-guided nanorobot without any user interaction during tracking, additional information about the feature trajectory lying ahead of the local sensor is needed. Image processing algorithms are applied to extract the necessary data from the video microscope sensor (module 'image processing' in fig. 4.2). The goal of such algorithms is to support the local control loop at critical points (i.e. crossings of two paths, junctions, 90° change in direction and steady direction changes exceeding a predefined angle) where it is not possible to get enough information about the future path trajectory from the local sensor only. Fig. 4.15 displays some test structures used to check the capabilities of the global sensor to detect critical points such as crossings of circuit paths, junctions or changes in the direction.

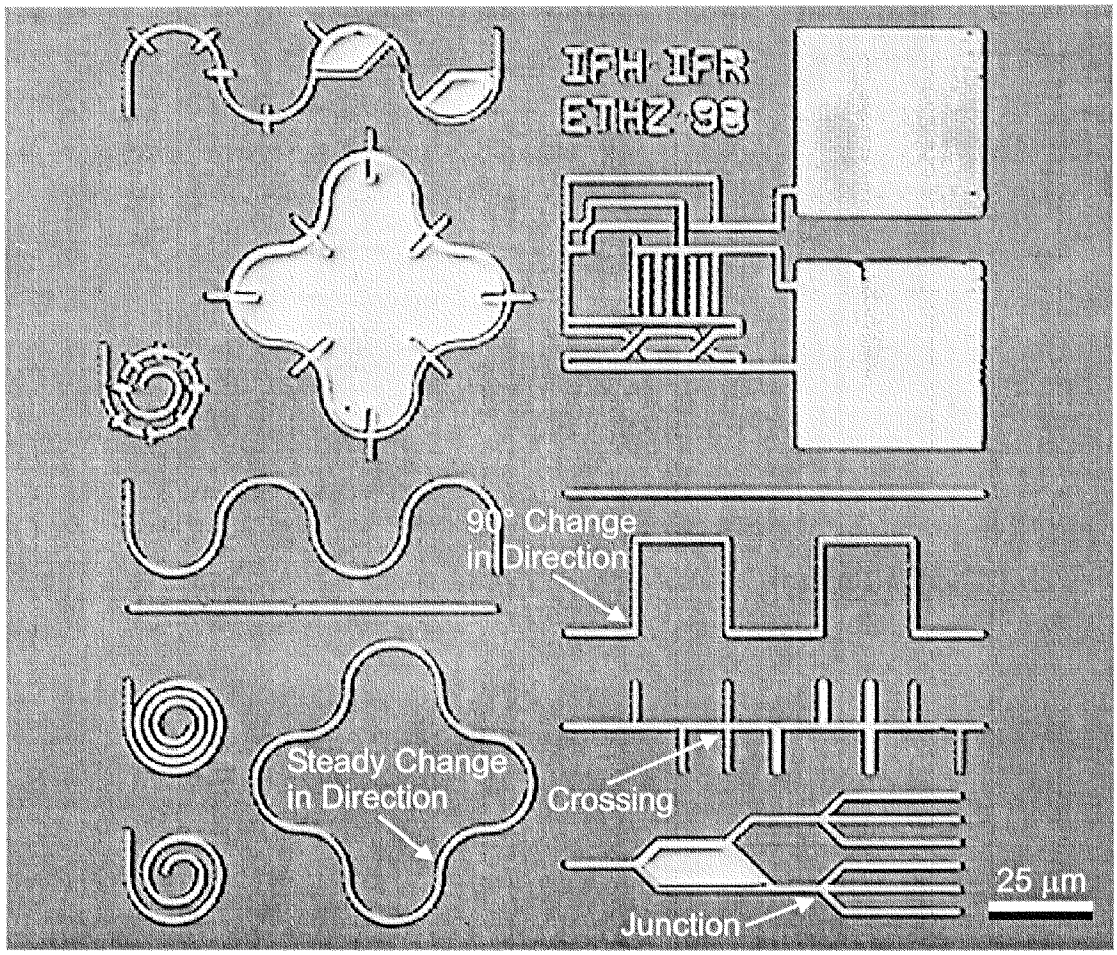


**Fig. 4.15:** *Test structures with different critical points to detect*

This tracking algorithm is integrated in the GUI of the nanorobot which allows the user to interact with the system by choosing the direction at junctions to define the path to investigate. Then tracking can be started and the nanorobot acquires the data along the user-defined path.

In addition to the analysis of the path trajectory, the global sensor also has to measure the translation vectors of the transformation matrix discussed in section 4.2.1. The tip has to be found inside the CCD image which is equivalent to the determination of the translation vector between the fine positioning and vision coordinate systems. Furthermore, the structure of interest (e.g. the HEMT) has to be located. This requires the calculation of the translation between the coarse positioning and vision coordinate systems.

*Feature Detection*

To generate a list of all critical points, first the edges and lines in the image have to be detected. This is done using Canny filters [Canny86] (see section 4.2.5). Compared to Sobel, Prewitt or Roberts edge detector filters [Gonzales93, Ritter96], the computational effort is slightly higher but the result images benefit from the smoothing character of the Canny filter. To extend Canny filters to two dimensions (fig. 4.16) we use a Gaussian surface $G(x, y)$ according to eq. 4.29 with a unit volume.

$$G(x, y) = \frac{1}{2\pi\sigma^2} e^{-\left(\frac{x^2 + y^2}{2\sigma^2}\right)} \tag{4.29}$$

Similar to the one dimensional case, we can calculate the first derivative to detect edges and the second derivative to find lines. Because of the two dimensions of the function, the derivative can be calculated in different directions. Therefore, the resulting filter is strongly sensitive to edges and lines lying along or close to the direction of the calculated derivative. To reduce the computational load for detecting features over the full 360°, the algorithm only uses four filters with the direction of 0° $G'_0(x, y)$ (eq. 4.30), 45° $G'_{45}(x, y)$ (eq. 4.31), 90° $G'_{90}(x, y)$ (eq. 4.32) and 135° $G'_{135}(x, y)$ (eq. 4.33).

$$G'_0(x, y) = -\frac{x}{2\pi\sigma^4} e^{-\left(\frac{x^2 + y^2}{2\sigma^2}\right)} \tag{4.30}$$

$$G'_{45}(x,y) = -\frac{(x+y)}{2\sqrt{2}\pi\sigma^4} e^{-\left(\frac{x^2+y^2}{2\sigma^2}\right)} \tag{4.31}$$

$$G'_{90}(x,y) = -\frac{y}{2\pi\sigma^4} e^{-\left(\frac{x^2+y^2}{2\sigma^2}\right)} \tag{4.32}$$

$$G'_{135}(x,y) = -\frac{(x-y)}{2\sqrt{2}\pi\sigma^4} e^{-\left(\frac{x^2+y^2}{2\sigma^2}\right)} \tag{4.33}$$

The four line filters with the direction of 0° $G''_0(x,y)$, 45° $G''_{45}(x,y)$, 90° $G''_{90}(x,y)$ and 135° $G''_{135}(x,y)$ are represented mathematically by eq. 4.34 - eq. 4.37. In all filters, the parameter $\sigma$ controls the noise-filtering performance and the feature dimensions to be detected. Furthermore, the computing time of the filter depends linearly on the parameter $\sigma$ i.e. with an image size of 768 x 576 pixels and $\sigma = 1$ we have to perform about $1.6 \cdot 10^7$ arithmetic operations.

$$G''_0(x,y) = \left(\frac{x^2}{2\pi\sigma^6} - \frac{1}{2\pi\sigma^4}\right) e^{-\left(\frac{x^2+y^2}{2\sigma^2}\right)} \tag{4.34}$$

$$G''_{45}(x,y) = \left(\frac{(x+y)^2}{4\pi\sigma^6} - \frac{1}{2\pi\sigma^4}\right) e^{-\left(\frac{x^2+y^2}{2\sigma^2}\right)} \tag{4.35}$$

$$G''_{90}(x,y) = \left(\frac{y^2}{2\pi\sigma^6} - \frac{1}{2\pi\sigma^4}\right) e^{-\left(\frac{x^2+y^2}{2\sigma^2}\right)} \tag{4.36}$$

$$G''_{135}(x,y) = \left(\frac{(x-y)^2}{4\pi\sigma^6} - \frac{1}{2\pi\sigma^4}\right) e^{-\left(\frac{x^2+y^2}{2\sigma^2}\right)} \tag{4.37}$$

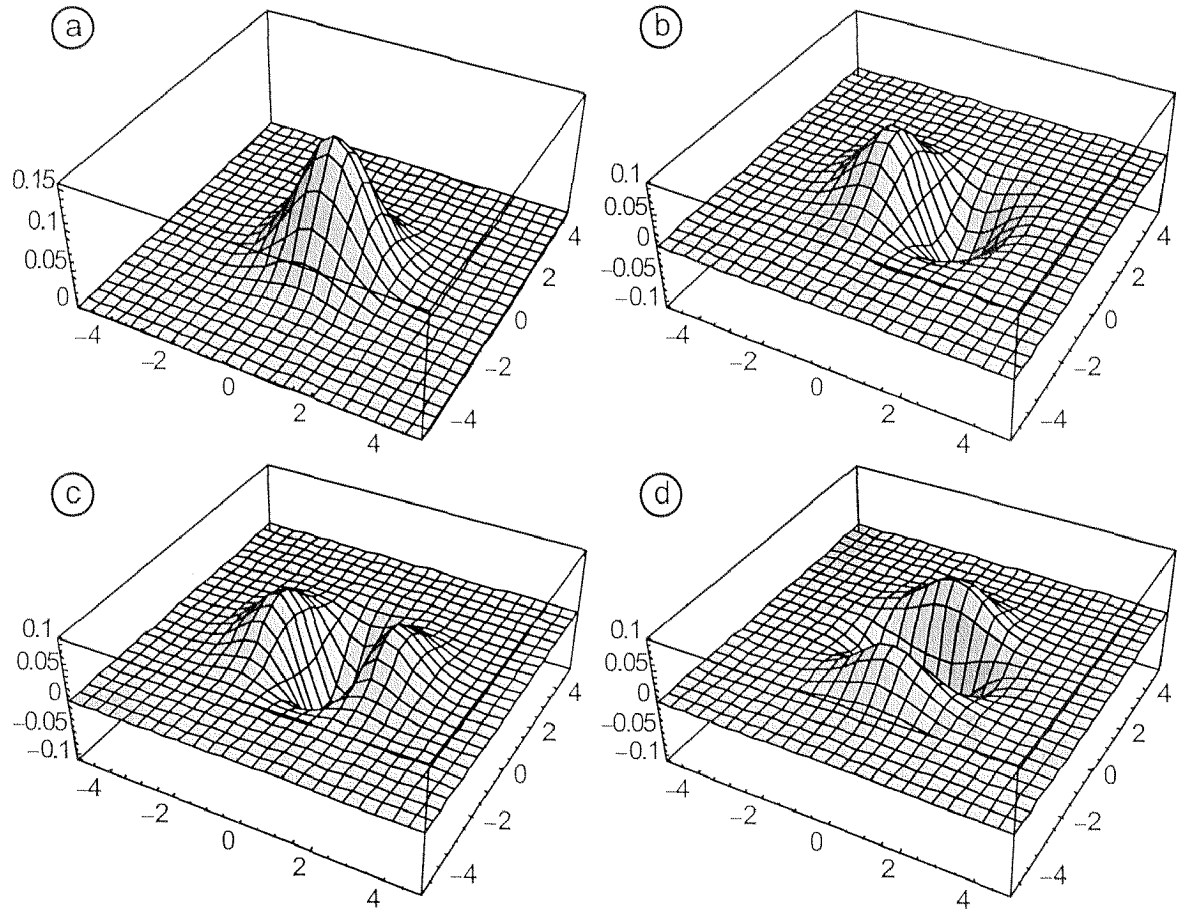


**Fig. 4.16:** *2D Gauss curve $G(x, y)$ (a) and its first derivation in x-direction $G'_0(x, y)$ (b) as well as its second derivation in x-direction $G''_0(x, y)$ (c) and y-direction $G''_{90}(x, y)$ (d) used as Canny filters*

Depending on the feature to be detected, the source image from the CCD camera is convoluted with either the four edge or line filters. Fig. 4.17 (a) displays a test image in which the edges have to be detected. After having convoluted the source image (a) with the edge filters, four temporary images result describing the found edges close to each filter direction. These four images can be merged into one

single image in which the gradients are contained independent of their directions (c).

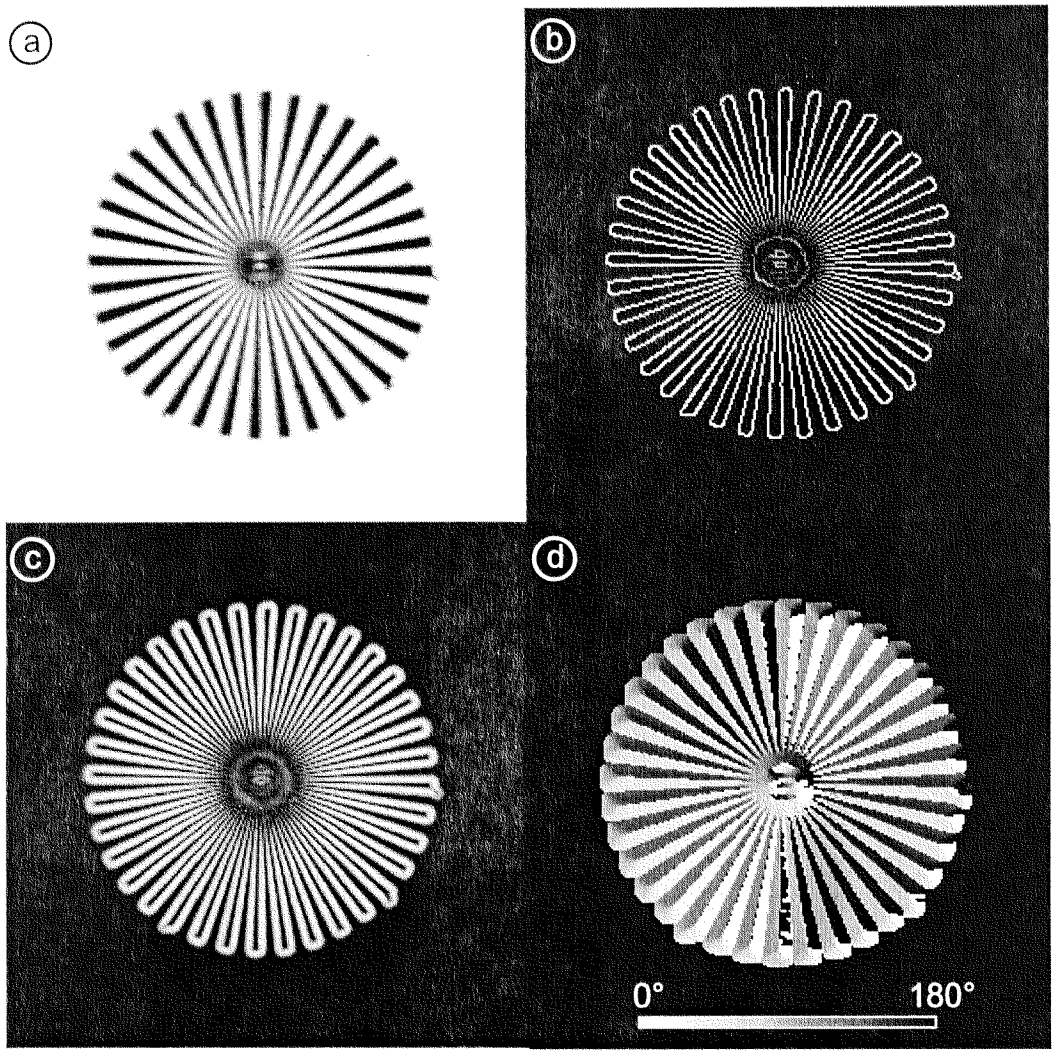


**Fig. 4.17:** *The siemens star used as test sample for edge detection (a) with the found edges (b), the gradient image (c) and the corresponding edge direction (d) using a σ of 1*

In a next step, the edges are extracted applying an algorithm called non-maximum suppression [Gerig96]. Due to the fact that an edge is represented by a high filter output (in the image represented by brighter color values) and that the filter response is the stronger the closer the filter direction is to the edge direction, this algorithm runs through all image pixels and compares the color values of all four filter results. By finding the maximum and skipping the other values, this extremum can be stored in an image including all edge positions (fig. 4.17 b). Furthermore, the direction of the filter with the maximum response can be stored in a

second result image (d). In this way, two new images are generated with the information of the edge position in the image as well as the best prediction of the edge direction. Fig. 4.17 shows these result images and proves that the limitation to four filter directions is not very restrictive.

*Extraction of Critical Points along a Tracking Trajectory*

After the feature detection (i.e. detection of lines or edges), an additional step of image processing must be added to extract the critical points from the found edges or lines. For this reason, the bitmap image (fig. 4.17 b) has to be transformed into a vector image where lines are represented by their parameters and not as a sequence of pixel points. This is a well known problem in computer vision. Hough [Duda72, Illingworth88] proposed a transformation which allows one to convert a pixel image to a vector image in order to get the parameters of the lines in the image. The problem with the Hough transformation is its high computational load and large memory use that scales with the number of parameters. Due to this, we decided to take a different approach to extract the feature trajectory parameters and especially their crossing points, start and end positions. In the following the critical points are called 'event' due to fact that all events are laying in sequence along the path trajectory. We distinguish *start* (beginning of trajectory), *stop* (end of trajectory), *curve* (direction change exceeding a predefined value) and *junction* (two and more possible new directions) events.

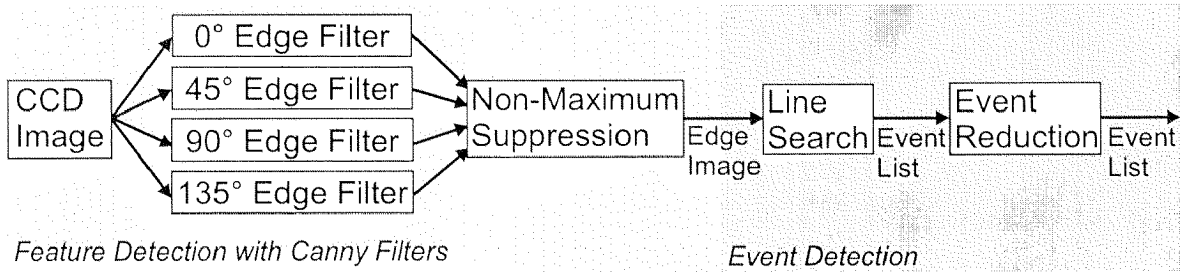


**Fig. 4.18:** *Schematic overview of image processing algorithm to extract critical points in circuit paths*

Fig. 4.18 displays the basic working scheme of our image processing algorithm. First, the CCD image is convoluted with the four edge detecting filters. After fusion to one resulting image including the edges and their orientation, this output image is fed to a line tracking algorithm which searches for critical points along an edge line such as crossings of circuit paths, junctions or changes in the direction. In the end, this list is reduced to avoid double entries of the same event.

The tracking begins either at a user-defined starting point selected through the GUI or it is calculated based on the start point of the local loop automatically found by the system (see section 4.2.2). As shown in fig. 4.19, the algorithm first checks if the edge trajectory goes straight on. If this is not the case, the existence of a curve is tested. The tracking either stops by generating a stop event entry, if no curve is found, or it puts a event 'curve' into the event list. Finally, the tracking mechanism examines the edge trajectory for a junction event and performs a next step starting the whole event-search over again. This method is similar to the working principle of the local control loop where the local sensor (i.e. the AFM tip) is guided along the feature based on actually measured data.

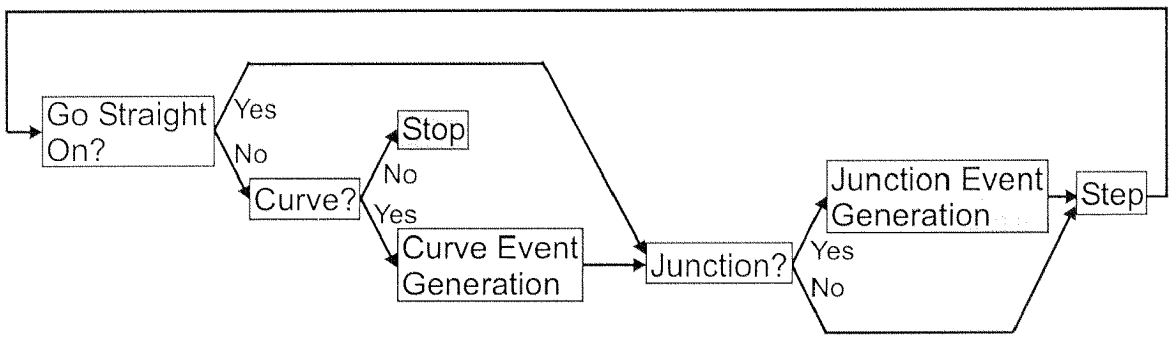


**Fig. 4.19:** *Flow chart for event detection in global sensor information*

In general, the algorithm runs along a line by looking at the adjacent pixels in the edge image to decide whether a feature is present or not (fig. 4.20). To detect a straight line, the pixel values along a set direction are added. This is done with several directions in a limited sector around the working direction. The largest sum of pixel values of these directions represents a possible new direction (see fig. 4.20). Hence, the algorithm tracks along the direction with the smallest edge gradient meaning it follows the strongest response of the edge filter. Thus, the algorithm finds the middle line of the feature trajectory. Applying a threshold to this sum minimizes the detection faults of new directions. For the definition of the angular range antagonistic demands have to be considered. On the one hand, the range should be as small as possible to avoid false detection of junctions or curves. On the other hand, it should be reasonably large to allow for modest curvatures of the trajectory. In our setup an angular range of ±5° has shown to be a good compromise.

A similar working principle is used for the detection of curves and junctions. The only difference is that the pixel values are added in the whole range of 360°

around the actual position (see fig. 4.20). If there are several possible answers, the one closest to the actual working direction is chosen. To distinguish junctions a minimal angular difference between evaluation direction and trajectory direction has to be distinguished. In our implementation this value is set to 30°. After these checks the algorithm moves a step further in the identified direction and repeats all the calculations. The step size is set to 3 pixels in the current setup.

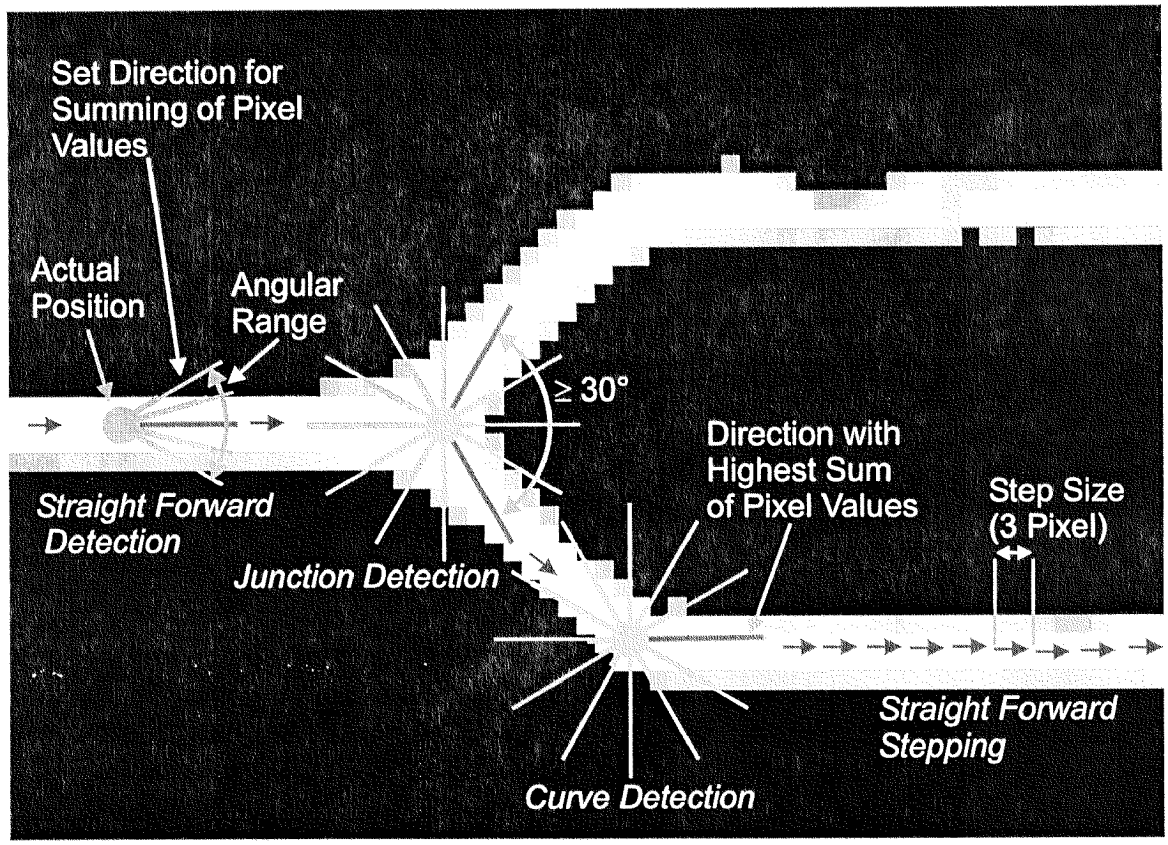


**Fig. 4.20:** *Working principle for event detection*

*Reduction of Extracted Events*

After the event extraction, a list is generated containing all information about critical points along the trajectory. In this event list, the type of event (i.e. curve, junction, start or stop point) is stored together with its position in pixel coordinates. Depending on the event type, additional information is available (e.g. the new trajectory direction at a curve event or the alternative directions at junctions). The number of events in the list depends on the source image, the shape of the path trajectory and its length and often there is more than one entry for the

same event. Therefore, in a next step these list entries have to be analyzed and checked for duplicates (fig. 4.21).

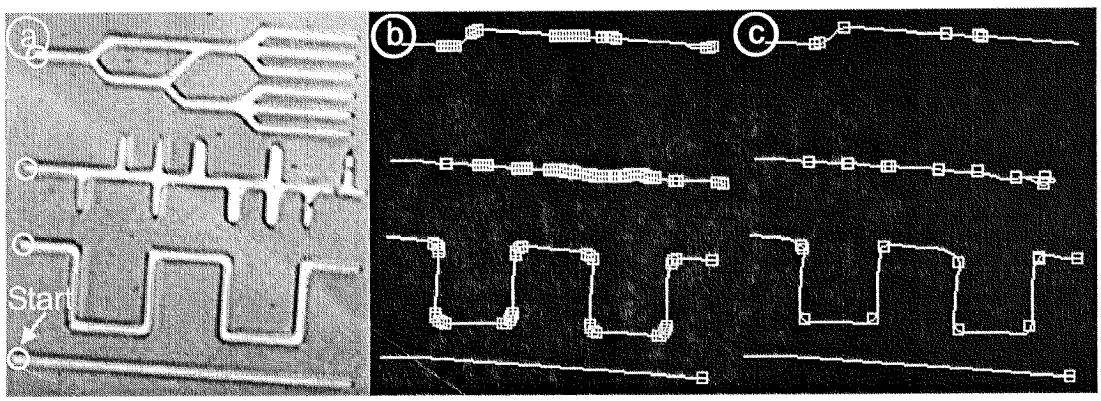


**Fig. 4.21:** *Source image (a) with detected critical points before (b) and after (c) event reduction*

The first criteria for a reduction of two events of the same type is the distance between their positions $(x_1, y_1)$ and $(x_2, y_2)$ (fig. 4.22). If the distance is smaller than a given threshold $d_{max}$ the fusion of these events is possible (eq. 4.38). A good value for this threshold is 10 - 15 pixels which is sensor-dependent and in the current setup (see section 3.2.3) equivalent to 4 - 6 µm.

$$\sqrt{(x_1 - x_2)^2 + (y_1 - y_2)^2} < d_{max} \tag{4.38}$$

In addition, for junctions, the angles of the alternative direction may not differ more than a maximum angle $\chi_{max}$ (eq. 4.39). As already mentioned, this angle is set to 30°. Therefore, two trajectories will only be distinguished by the algorithm if their directions differ by more than 30° as can be seen in fig. 4.22 where event 1 and 2 are not fused. This is not a real limitation because we are working primarily on integrated circuits where wires usually cross at 90° or 45°. Nevertheless, these parameters can be adapted to other needs.

$$|\chi_1 - \chi_2| < \chi_{max} \tag{4.39}$$

If these criteria are met the two list elements will be deleted and a new event entry is generated with the new position according to eq. 4.40 and eq. 4.41.

$$x_n = \frac{x_1 + x_2}{2} \tag{4.40}$$

$$y_n = \frac{y_1 + y_2}{2} \tag{4.41}$$

Furthermore, the direction is set according to eq. 4.42 for a curve event (event 4 and 5 in fig. 4.22) and according to eq. 4.43 for a junction event (event 2 and 3 in fig. 4.22).

$$\chi_n = \chi_1 + \chi_2 \tag{4.42}$$

$$\chi_n = \frac{\chi_1 + \chi_2}{2} \tag{4.43}$$

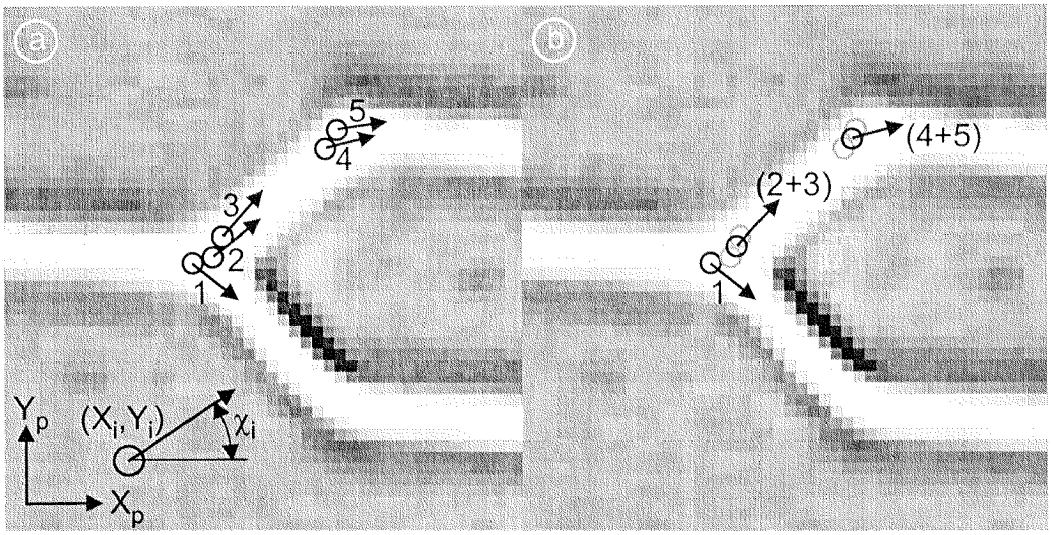


**Fig. 4.22:** *Principle working scheme for event reduction before (a) and after fusion of events (b)*

Fig. 4.23 shows the capabilities of the implemented tracking algorithm on the test structures. The results are very good and all critical points at which an interaction with the local control loop is required are detected. Compared to the Hough transformation, the computational load is much lower. We measured an average calculation time of about 150 ms for one trajectory search. This value depends linearly on the length of the path.

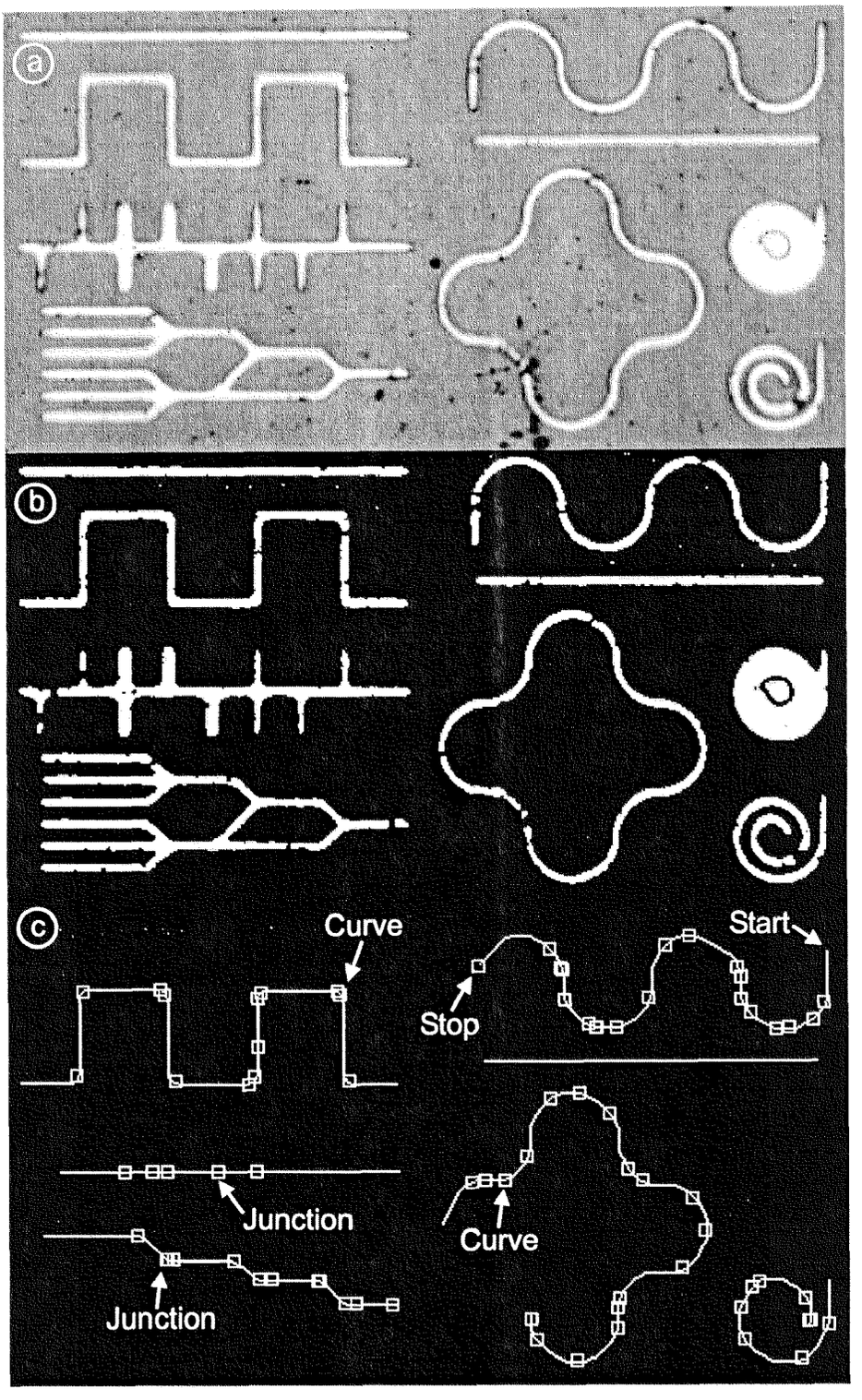


**Fig. 4.23:** *Result of event detection with source image (a), image of detected lines (b) and trajectory image with critical points (c)*

All thresholds and setting values mentioned above depend on the microscope magnification, the size of the CCD pixels and the structure under investigation as well as the illumination and are valid for the current platform (see section 3.2.3). Obviously, all parameters can be changed by the operator and hence the system performance can be adapted to different setups.

After extraction of the event list, the global image processing is ready to support the local control loop. After starting the tracking the actual feature position calculated in the fusion step (see section 4.2.6) is compared with the entries in the event list. If one entry is matching, a critical point (see fig. 4.15) is reached and the local loop needs assistance. Through the knowledge base (see section 4.2.7) the tracking parameters (e.g. the new tracking direction) are updated (see fig. 4.13). In this way the AFM tip is guided through critical points along the path trajectory.

*Feature Localization*

Beside the extraction of critical points, the video sensor is needed to locate structures (i.e. the feature to investigate or the AFM tip) inside the image and hence to derive the translations between the coordinate systems (see section 4.2.1). The problem of finding a feature in a CCD image is well known in image processing and can be solved by calculating the correlation between a template and the image [Gonzales93, Castleman96]. Fig. 4.24 displays the result of finding an AFM tip inside an image. The mask can be derived from a real image in a unprocessed (c) or processed (d) representation as well as from a drawn version (e) based on the theoretical and geometrical data.

A template representing the feature to be located (fig. 4.24 c, d, e) is correlated with a taken image (fig. 4.24 a) from the CCD camera. Finding the maximum value inside the resulting image (fig. 4.24 b) leads to the best fitting point of mask and image. After that, a given offset is added to the coordinate which describes the point of interest inside the mask. Calculating both AFM tip $(x, y)_T$ and HEMT position $(x, y)_S$ leads to the resulting translation vector $\underline{v}$ that enables the system to move the tip to the HEMT for further investigation (fig. 4.25).

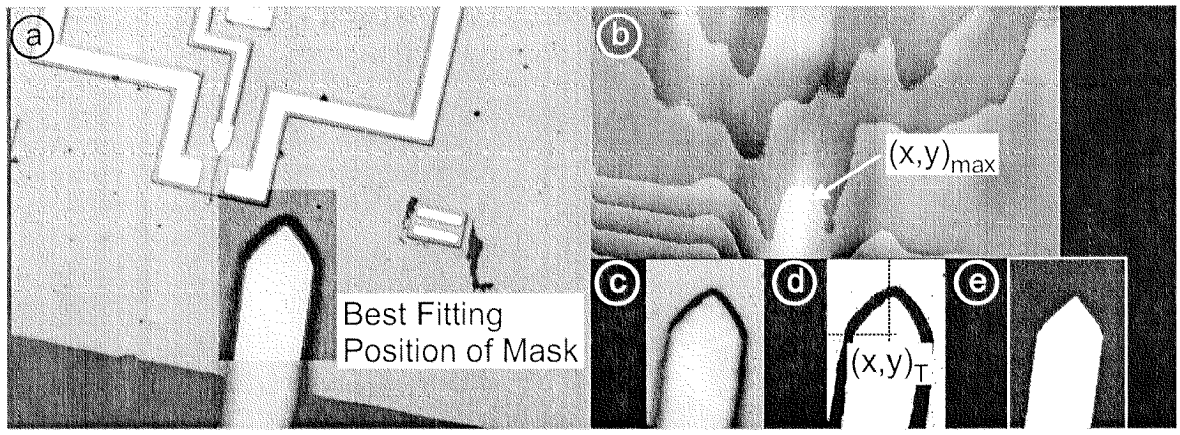


**Fig. 4.24:** *CCD image with best fitting mask position (a) as well as the correlation image (b) and three possible masks such as real image (c), processed real image (d) and theoretical (e)*

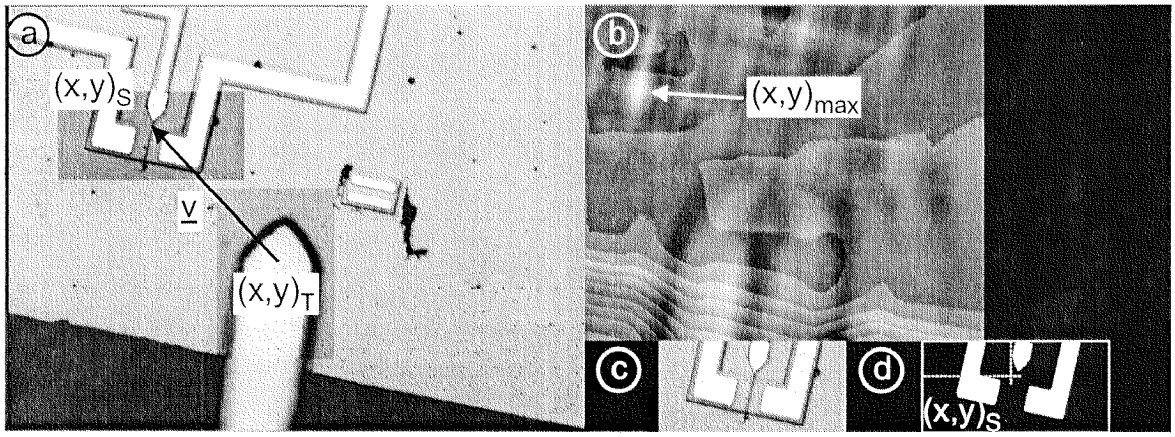


**Fig. 4.25:** *Measuring of translation vector between AFM tip and HEMT structure (a) with correlation (b) and different masks (c and d)*

The main problem of this calculation is the high computational load. Fig. 4.26 shows the antagonistic behavior of calculation time and localization error of the correlation as a function of the considered mask points. A value of one means that all mask points are considered in the correlation whereas a value of ten means that only every tenth mask pixel in a regular raster is considered. On the one hand, the more mask pixels are ignored the faster the correlation is calculated. On the other hand, the less information that is considered, the higher the localization error will be. Therefore, a good compromise between these two ten-

dencies has to be found. Experiments showed that a value between 5 to 9 leads to good results while keeping computation time at a minimum. The precision of this correlation calculation is good enough to fit the actual needs. In case higher precision is required, the image processing can easily be replaced by other algorithms, e.g. a program module that can calculate subpixel resolution [Brandstein95, Danuser97, Danuser00].

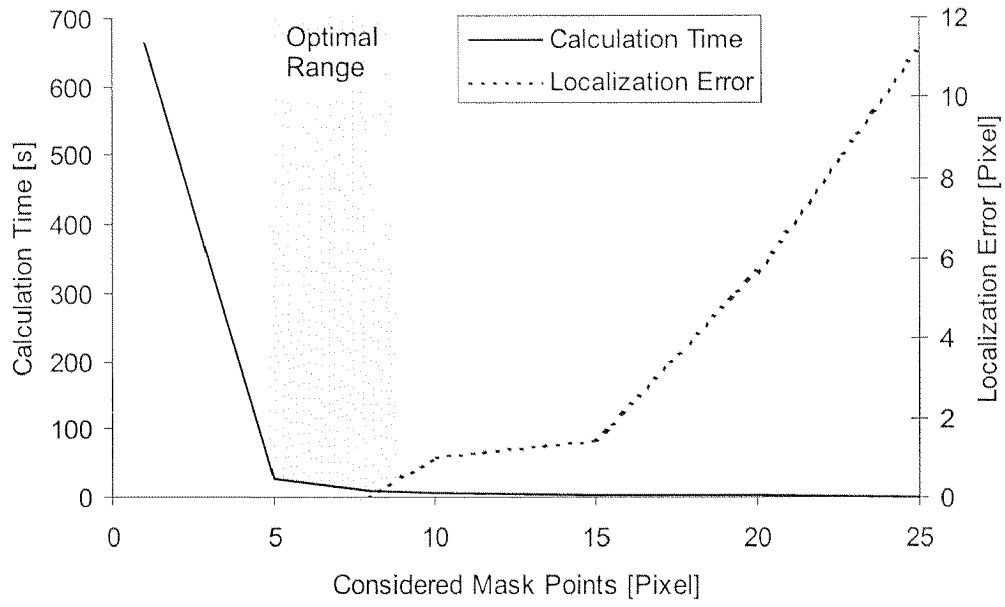


**Fig. 4.26:** *Relationship between calculation time and localization error from the considered mask points of a source image (757 x 546 pixels) correlated with a mask (152 x 219 pixels)*

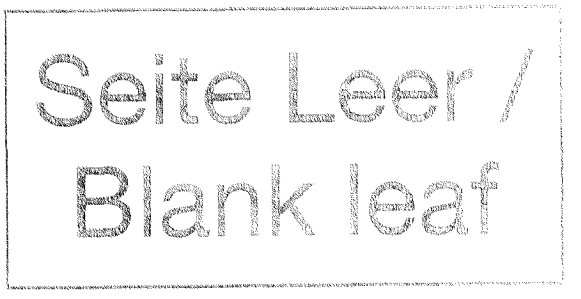
Seite Leer /
Blank leaf

# 5 Benchmark Tests and Applications

In this chapter, the performance of the controller structure introduced in chapter 4 is evaluated using different benchmark tests. First, the primary tracking strategy based only on local sensor inputs is investigated. In a second step, the system is tested on microstructures where local as well as global sensor data have to be used to follow the user-defined structure over a long distance. Finally, the system has to prove its capabilities on ICs, namely on field effect transistors. Here the electric field along the gate finger will be calculated based on the data acquired during tracking along the structure.

## 5.1 Tracking Based on Local Information

The system is first tested in the *local control* and the *semi-automated* mode as introduced in section 4.1.2. The structure under investigation is a micro fabricated heating coil (fig. 5.1) with a width of 10 µm and a length of 12 mm [Bächi99]. The coil is mounted on a glass plate and consists of a 300 nm chrome layer and a 200 nm aluminum layer. The sensor-guided nanorobot has to track along the coil to acquire the topography. This information is required to judge whether there are faults in the structure or not.

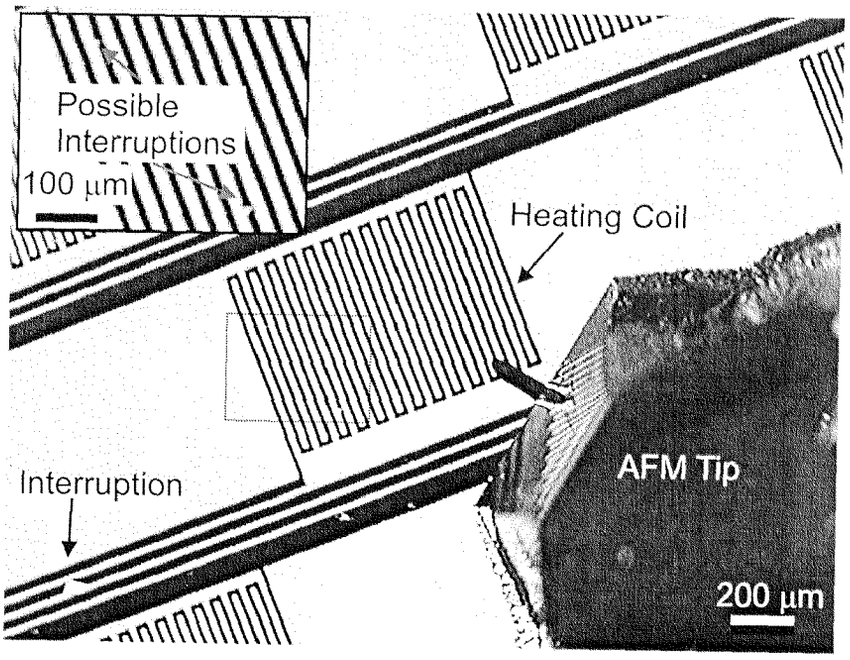


**Fig. 5.1:** *Top view image of the heating structure and the local sensor of the sensor-guided nanorobot*

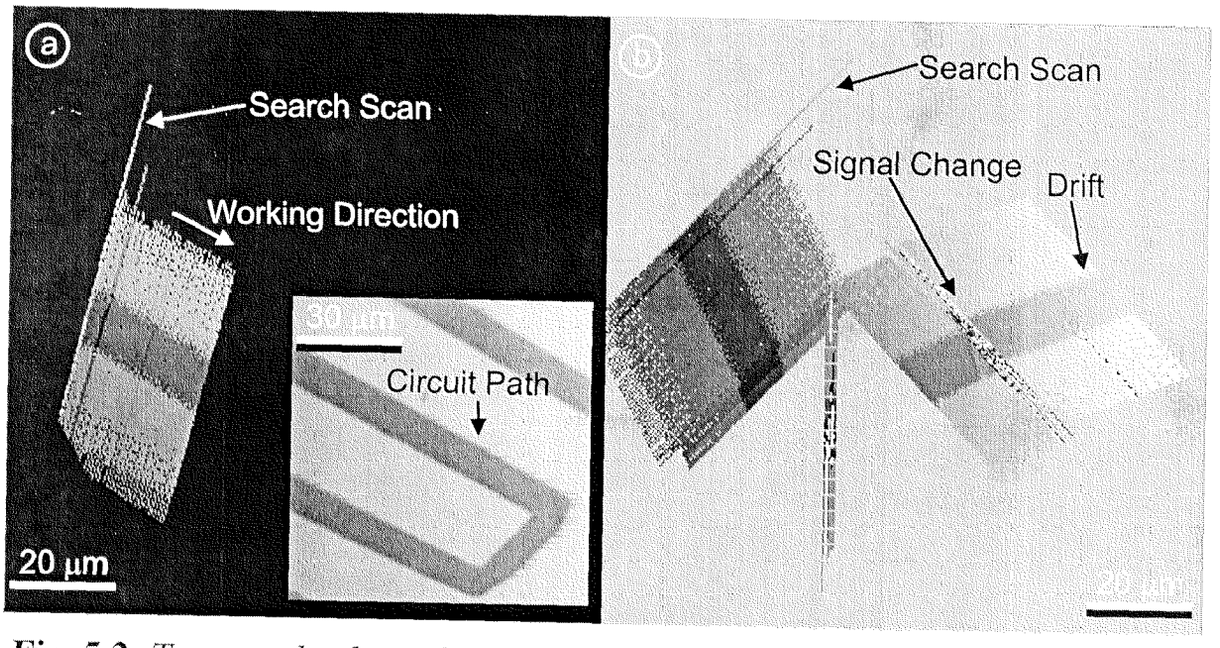


**Fig. 5.2:** *Topography data of circuit path (b) as well as different phases during tracking along the circuit path (b)*

Fig. 5.2 shows the result of this analysis. The system first is taught the approximate shape of the structure (see section 4.2.2). Based on the above mentioned geometric properties, we set the parameters for the analytic model to a structure width of 10 µm, the height to 500 nm and the angles to 90°. After defining a search range the system starts in a search scan to locate the structure. Following localization the structure is automatically tracked while acquiring the topography information. The tracking parameters are set to 300 nm as step size and 65 µm as scan line length. At the 90° bends, the operator has to change the tracking parameters manually because tracking around such edges is difficult for the AFM tip which relies on local information only. To run the system in the fully automated mode, these manual changes are replaced by the global vision control.

It clearly can be seen that the implemented controller strategy easily finds and follows microstructures (fig. 5.2 b). It is also possible to interact with the running controller and change e.g. the tracking direction. Furthermore, the nanorobot can handle signal changes due to short sensor break-downs without losing the trajectory of the path. These data are acquired without any hysteresis compensation of the fine positioning device. This proves that the nanorobot is flexible enough to deal with drift and non-linearities of the piezo tube and can compensate these effects during tracking the structure of interest.

To further check the abilities of the system microstructures with a width of 1 µm have been manufactured. The parameters for feature localization are determined based on the manufacturing data and set to 1 µm for the structure width, 30 nm for the its height and 90° for the angles. The scan line width is 3 µm while the step size is changed by the user during tracking. Fig. 5.3 (a) shows a rectangular structure on which the nanorobot can be tested. The system is able to find and track along the structure (b). The operator can interact with the local control loop during execution e.g. by manually changing the step size at less critical locations (c) in order to speed up data acquisition.

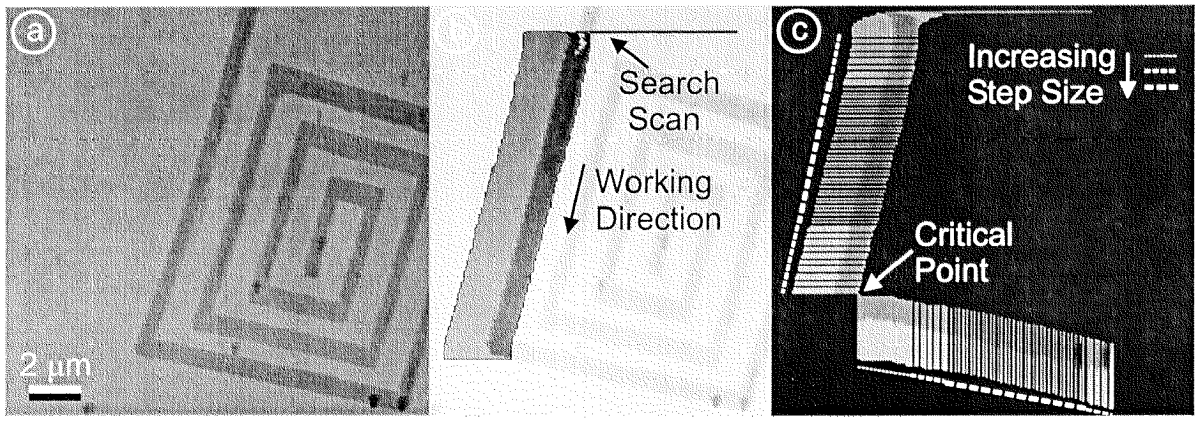


**Fig. 5.3:** *Test structure with 90° bends (a), results of structure localization and tracking (b) as well as interaction with the control loop by changing the step size (c)*

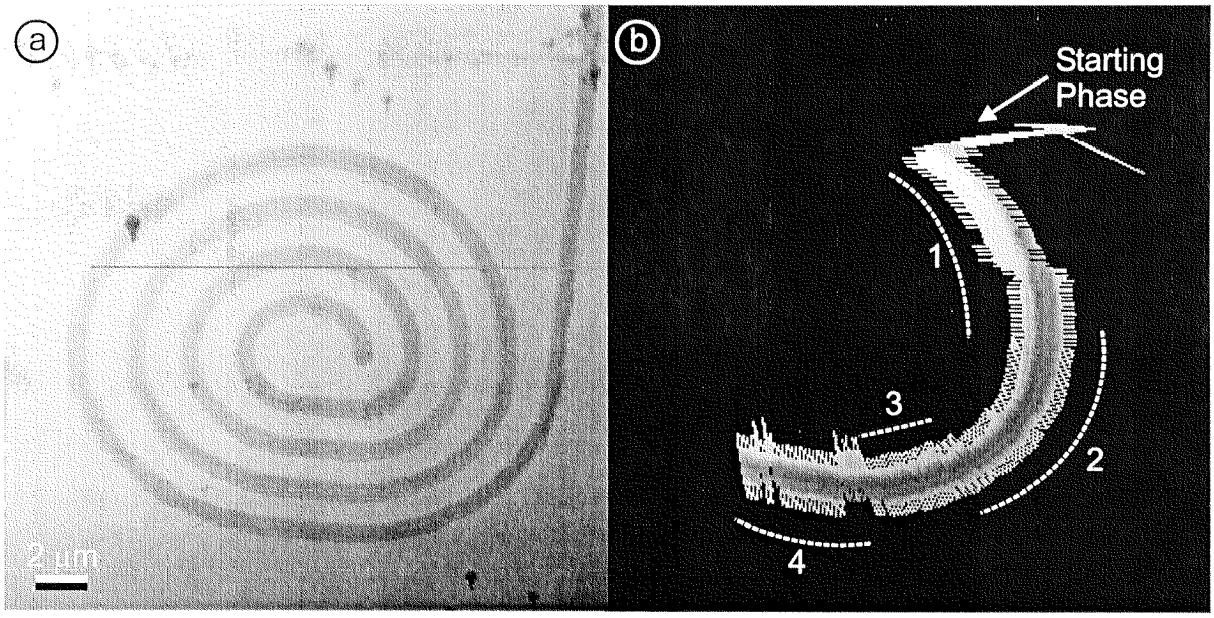


**Fig. 5.4:** *Swirl structure (a) and tracking result along the path (b)*

Fig. 5.4 (a) displays a swirl structure with similar geometric properties as the rectangular structure in fig. 5.3. For this reason, the tracking parameters are kept from the previous experiment. The system first missed the starting point (b) due to an incorrect set of starting range parameters. However, after some tracking scans, the nanorobot hits the structure and follows it. The controller is able to

compensate the plane offset and the slope of the sample that can be seen in the grading of the background from white to black (a). Furthermore, the operator can change the tracking angle during execution which is done between each phase of the tracking sequence (b).

## 5.2 Tracking with Local and Global Information

After having proved the capabilities of the local control loop, the sensor-guided nanorobot is tested in the *automatic* mode including the global image data as well as the coarse positioning. This is done on the microstructures already introduced in section 4.2.9 (fig. 4.15). The feature width is 1.5 µm and the structure height is approximately 150 nm. In addition, a value of 90° for the angles, 5 µm for the scan width and 100 nm for the step size are used as tracking parameters.

Fig. 5.5 shows the principle working scheme. After definition of the region of interest and the input of the a-priori knowledge of the structure by the operator, the global image processing acquires data (a) to extract an event list of critical points (b). Then, the system starts to search for the structure and tracks it while changing the tracking direction at the critical points (c). Thus, the sensor-guided nanorobot is able the use global (from the video microscope) as well as local information (from the AFM tip) to find and follow user-defined structures automatically.

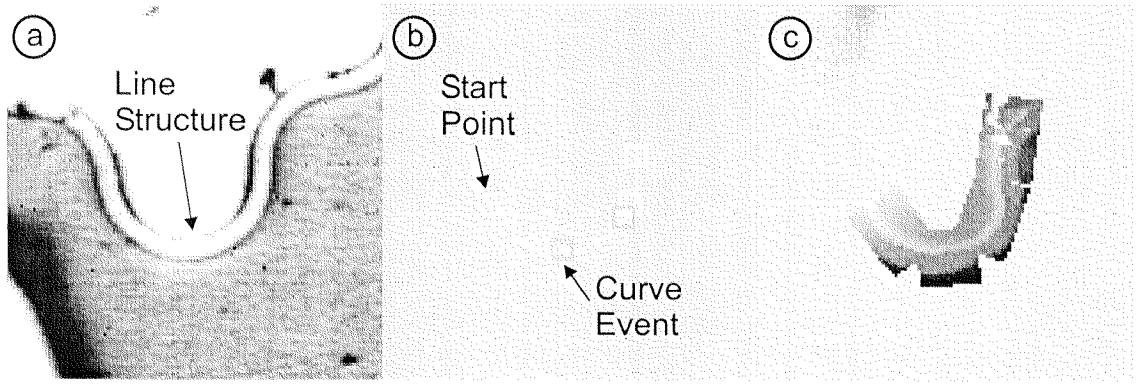


**Fig. 5.5:** *CCD image of line structure (a) and critical points found by global vision sensor (b) as well as the AFM topography data (c) of tracking sequence*

Fig. 5.6 (a) shows an image of a structure with 90° direction changes after applying the edge detector filter. The system is capable of following the path without any further interactions by the operator. Furthermore, the system is able to reposition the sample in case the fine positioning device has reached its working range limits (c). In this case the tip is moved to the center of its working range and the coarse positioning device is repositioned by the distance between the actual measuring point and the center of the fine positioning device.

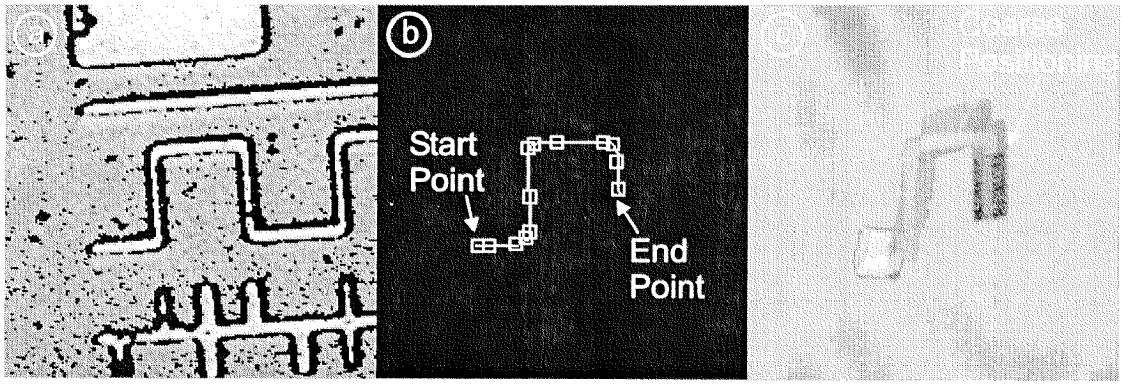


**Fig. 5.6:** *Result image of global edge detection (a) as well as critical points along the path (b) and tracking data of AFM topography (c)*

The sensor-guided nanorobot can also detect junctions of paths. Fig. 5.7 (a) shows such an example. The global image processing applies the edge detector filter (b) to detect the events (c). In case of a junction event the system makes a suggestion for possible further direction (e). The operator can interactively change this to an alternative direction (f) via the GUI. After the definition of the desired path, the system starts to acquire the topography information of the structure (d).

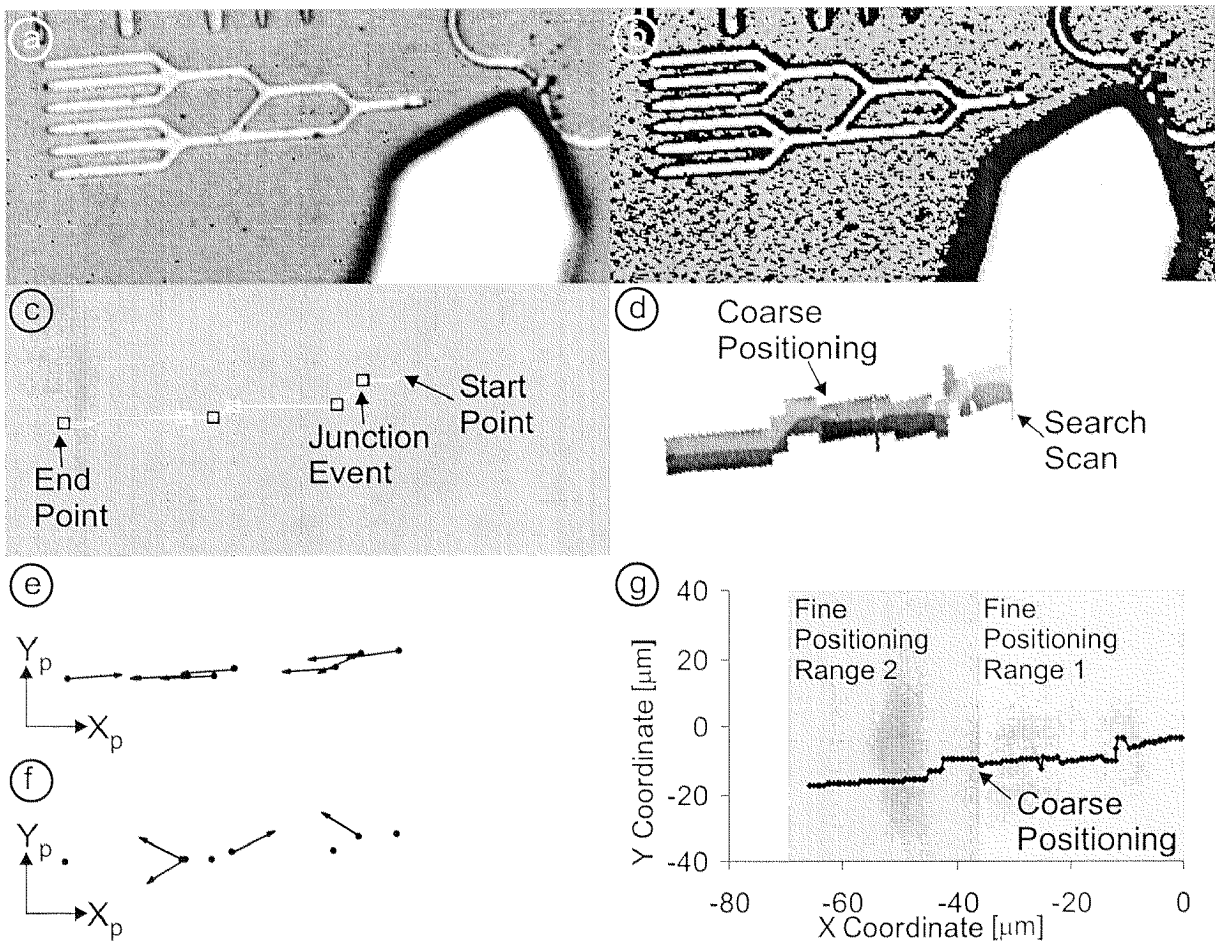


**Fig. 5.7:** *CCD image of test structure (a) with result image after edge detection (b) as well as critical points along the path (c). AFM topography data (d) as well as suggested direction for tracking (e) with possible alternatives (f). Furthermore, (x,y) coordinates calculated by the local control loop during tracking*

Due to the fact that the path trajectory is larger than the working range of the fine positioning device, the controller first guides the AFM tip to the end of the working range (range 1 in g) and initiates a coarse positioning step. After that the tracking can be resumed in the new working range (range 2 in g). In the current implementation, the AFM data before and after repositioning are recorded without any further corrections because the precision of the coarse positioning device is high enough for the size of the structure under investigation. This leads to a small offset in the acquired image. To compensate this offset in the measured data, an overlap of both ranges could be programmed and a correlation

[Gonzales93, Castleman96] of both image overlaps could be calculated to match both parts.

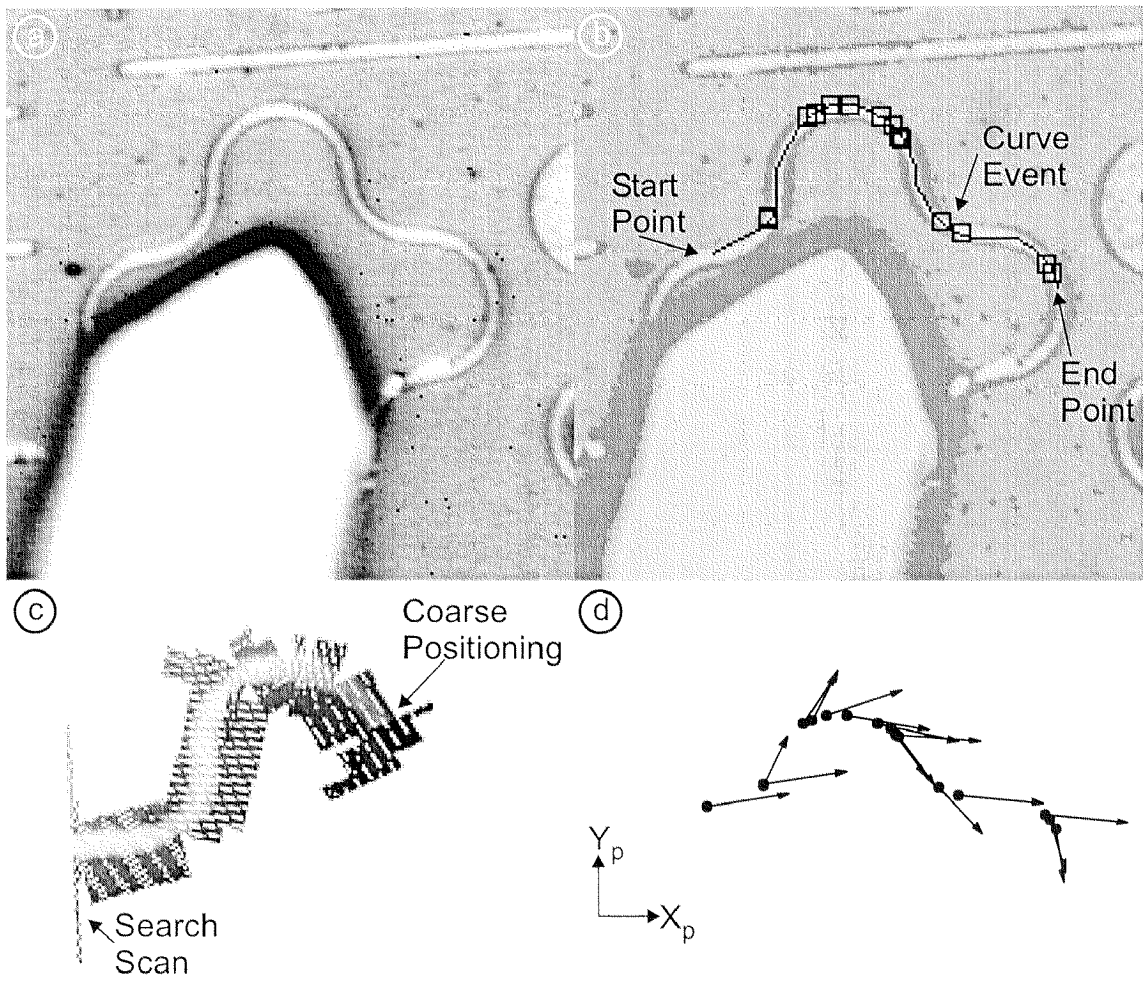


**Fig. 5.8:** *CCD image of the test structure (a) with the result image of edge detection and critical point detection (b) as well as AFM topography information (c) and curve events with new tracking direction (d)*

The sensor-guided nanorobot can automatically track along trajectories with bends and junctions using local as well as global information. Taking advantage of the information about stages lying ahead of the local sensor's actual position the step size is increased during tracking (fig. 5.8). Furthermore, the vision data improve the stability of the system.

To summarize, the sensor-guided nanorobot has proved its capabilities to track user-defined structures relying on local AFM and global CCD image data. In a

next step, the introduced system will be used for investigating transistor structures.

## 5.3 Tracking on Transistor Structure

During the design of integrated circuits, information about the quality of the structures and their electrical performance are important to derive criteria for optimization. The task-oriented working principle of the sensor-guided nanorobot supports such investigations by automatically acquire the required data.

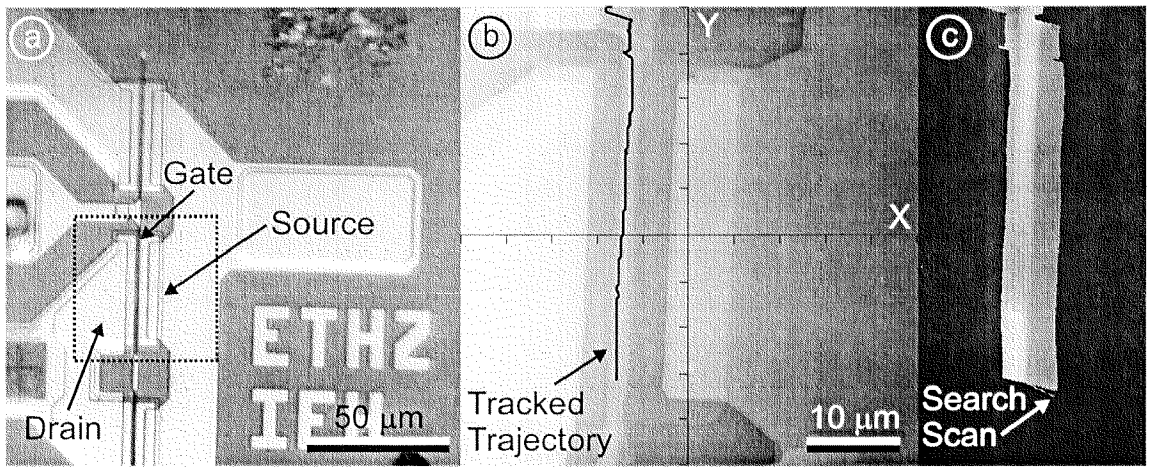


**Fig. 5.9:** *Video microscope image of the transistor structure (a) with AFM topography image (b) boundaries as well as tracked trajectory data (c)*

Fig. 5.9 shows the analysis of a transistor structure. To judge the quality of the structure and especially the gate finger, the light microscope image (a) is used for far-field observation of the specimen. Apparently, the micro fabrication process was successful and all elements seem to be reproduced very well. Unfortunately, the resolution of the light microscope is not high enough to view details of the gate finger. To gain local high resolution data, near-field information could be obtained with a AFM system in a conventional way, i.e. by acquiring a topography image (b) of the gate area. A much more efficient way on the other hand makes use of the abilities of the presented system by allowing the operator to define the approximate shape of the gate finger and start the automatic data acquisition along it (c). Based on this information, it can be seen that indeed the

gate finger has no damages. The result proves that the nanorobot can perform this task and hence speed up and simplify such investigations of gate areas.

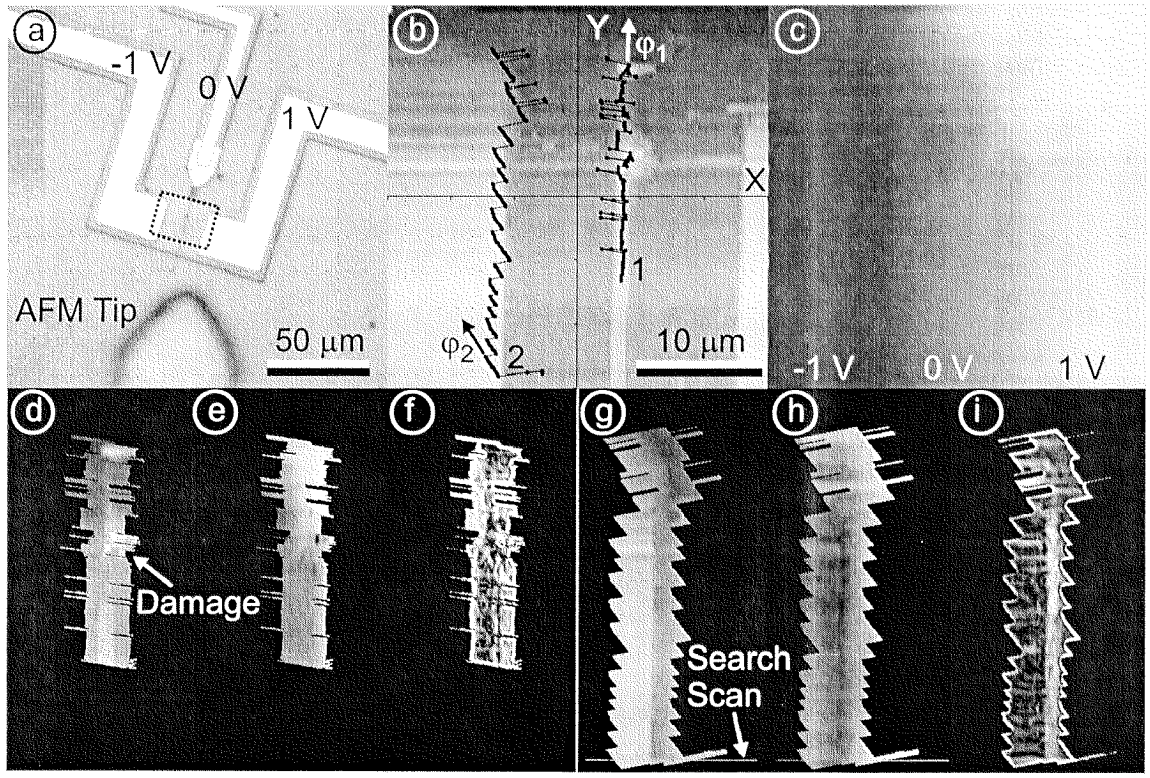


**Fig. 5.10:** *Light microscope image (a) with boundaries of AFM topography (b) and surface potential image (c) as well as tracking of the gate finger (trajectory 1) and a transistor edge (trajectory 2). Acquire data of topography (d, g) and surface potential (e, h) during tracking and the calculated electric field (f, i)*

The multifunctional characteristic of the local sensor can be used to derive information about the electric performance of a transistor structure. Fig. 5.10 displays a transistor specimen where the performance will be examined. The far-field observation (a) reveals no serious damage of the structure. First, the gate finger is tracked (trajectory 1 in (b)) and a damage gets exposed (d). Based on the acquired surface potential (e), the electric field (f) can be calculated. It has to be remarked that the apparently high electric field at the edges of the tracked data region is due to the calculation algorithm that produces high values at the transition of the data region to the background. Hence, these results do not correspond to an existing field on the specimen.

Whereas the first trajectory points in the correct direction $\varphi_1$, the second trajectory (trajectory 2 in (b)) is intentionally set to a direction $\varphi_2$ differing from the structure under investigation. The controller was not allowed to adapt this direction and hence adjusts the remaining tracking parameters (i.e. the offset of the interpolated line) according to the extracted feature positions. It clearly can be seen that the local control loop is capable of handling inaccurate settings and nevertheless can perform the task of tracking an edge. The analysis of the strength of the electric field (i) calculated based on the topography (g) and the surface potential (h) shows no high regions where disruptive discharges could occur.

It has been shown that the presented sensor-guided nanorobot is a powerful and flexible tool for an automated analysis of integrated circuits. The task-based working scheme relieves the operator from acquiring image by image by just defining the task the system has to perform.


Seite Leer /
Blank leaf

# 6 Conclusions and Outlook

## 6.1 Conclusions

As already pointed out in the introduction, the goal of this thesis was the design of a control strategy to meet the requirements of an automatic machine working in the (sub)micro world. The system must combine local information accessed by e.g. SPMs, global information e.g. from a video microscope and a-priori knowledge to perform predefined tasks. This fusion allows one to obtain high resolution data from a multi-functional sensor as well as far-field information of the specimen.

First, a new generation of tools was developed allowing the micro world to be accessed in order to manipulate micro objects. These manipulators are equipped with an integrated sensor to measure the tool-object distance. Based on this sensor automated tasks can be implemented in a robot environment, e.g. collision avoidance to prevent tool damage or automatic approach to a micro particle.

In a next step a test platform was designed to evaluate control strategies for the nano world. The actual setup relies on an AFM tip as local tool. The multifunctional characteristics allows the topography as well as the surface potential to be measured. These data are needed to optimize IC structures. To extend the current system to other applications (e.g. automated assembly of micro fabricated parts with the glass pipette) special emphasis was laid on a modular design of the whole robot system. Based on this platform the controller is implemented. An

easy-to-understand interface to the system enables the application in industrial environments where users most often are not familiar with AFM measurement techniques. For this reason, the sensor-guided nanorobot supports the operator with automated routines to set up the measurement modes.

A control loop processes the actually acquired data from the local sensor in real-time. This on-line data processing enables the robot to use the AFM tip not only as very sensitive measurement tool with high resolution but also as sensor to obtain information about the actual situation on the sample surface. Hence, the operator does not have to acquire images as with a microscope to get the needed data about the structure but defines the feature of interest based on his a-priori knowledge to start the automatic data acquisition along the desired feature trajectory. This task oriented operation principle leads to a reduction of the data acquisition time because only the necessary information is measured. It offers the possibility of employing this sensor-guided nanorobot in a fully automated environment.

The presented setup is very well suited to implement behavior concepts for the (sub)micro world. Compared to commercially available systems the robot platform can be freely programmed and extended to actual needs. Thus, behavior concepts of systems working in the nano world can be implemented, tested and optimized. The presented setup demonstrates a powerful way to combine local high resolution and global far-field information to perform given tasks automatically, e.g. the analysis of transistor structures.

## 6.2 Outlook

In the current setup some modifications could be made to improve the system performance. First, the hysteresis compensation of the piezo scanner can be replaced by a hardware linearization based on a closed-loop control with an adequate position sensor [Barrett91]. The implemented software linearization is sufficient for the testing of behavior concepts, but a hardware realization would relieve the DSP of computational load. The available machine time can be used to speed up the other running tasks. In order to further speed up the data acquisition, new controllers are needed for the AFM measurement modes that allow higher scan rates, e.g. implementation of $H_\infty$-controllers [Morari89] instead of PID-controllers. Furthermore, the setup can be extended to rotational DOF, e.g.

using of a Steward platform with 6 DOF. This may be interesting in setups with integrated micro manipulators.

The presented glass pipette can handle object sizes above 10 µm. The idea of using an additional control loop to flexibly acquire local information or to manipulate micro objects can be extended to object sizes smaller than 1 µm. With such particle dimensions tools are required that, similar to the presented glass pipette, combine sensing and actuating skills in one device to gain access to local properties with high resolution. Different possible tools have already been suggested, e.g. AFM tips [Junno95, Sheehan96, Hartmann96, Baur98, Resch99] or STM tips [Stroscio91, Jung96]. These tools have proved their ability to manipulate atoms and molecules. Nevertheless, the control of the tool during manipulation is difficult and often done in an open-loop mode. Hence, a local control loop that processes the actual data to control the tool position would be of great value.

Apart from applications in IC analysis or manipulation of micro and nano particles, the presented concept of a sensor-guided nanorobot can be applied to other domains, e.g. minimal invasive surgery. In this field, scalpels with an integrated force sensor or biochemical sensor could support the surgeon by getting more information from the scalpel tip than with vision alone and hence reduce the risk of damage of adjacent structures. Furthermore, with suitable control loops the tool can find its way along a nerve tract or a blood vessel.

The presented concept of a sensor-guided nanorobot is a first step towards systems that can execute user-defined tasks in the nano regime automatically. By combining information from the micro and macro world they overcome the resolution limits of macro sensors and can work on microstructures with high precision. The high level of automatization allows the tasks to be analyzed more quickly and productivity to be increased due to automated execution without user assistance. Ultimately, it may allow nano structures to be built automatically by robot systems.

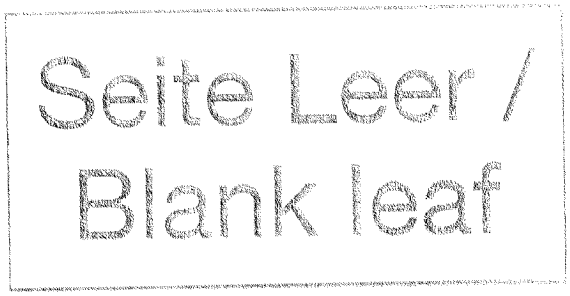
Seite Leer /
Blank leaf

# 7 References


[Accame97] M. Accame and F. G. B. De Natale: Edge Detection by Point Classification of Canny Filtered Images. *Signal Processing*, vol. 60, pp. 11-22, 1997

[Arai95] F. Arai, D. Ando, T. Fukuda, Y. Nonoda and T. Oota: Micro Manipulation Based on Micro Physics - Strategy Based on Attractive Force Reduction and Stress Measurement. *IEEE/RJE Conference on Intelligent Robots and Systems*, vol. 2, pp. 236-241, Pittsburgh, Aug. 1995

[Arai97] F. Arai and T. Fukuda: Adhesion-type Micro Endeffector for Micromanipulation. *Proceedings of the 1997 IEEE International Conference on Robotics and Automation*, pp. 1472-1477, Albuquerque, New Mexico, April 1997

[Arai98] F. Arai, D. Andou, Y. Nonoda, T. Fukuda, H. Iwata and K. Itoigawa: Integrated Microendeffector for Micromanipulation. *IEEE/ASME Transactions on Mechatronics*, vol. 3, no. 1, pp. 17-23, March 1998

[Ashkin86] A. Ashkin, J. M. Dziedzic, J. E. Bjorkholm and S. Chu: Observation of a Single-Beam Gradient Force Optical Trap for Dielectric Particles. *Optics Letters*, vol. 11, no. 5, pp. 288-290, May 1986

[Bächi99] D. Bächi and R. Buser: Suspension Handling System. *CD-ROM Proceedings of Eurosensors XIII*, 10C03, Den Haag, Netherlands, 1999

[Barenz96] J. Barenz, O. Hollricher and O. Marti: An Easy-to-Use Non-Optical Shear-Force Distance Control for Near-Field Optical Microscopes. *Review of Scientific Instruments*, vol. 67, no. 5, pp. 1912-1916, May 1996

[Barrett91] R. C. Barrett and C. F. Quate: Optical Scan-correction System Applied to Atomic Force Microscopy. *Review of Scientific Instruments*, vol. 62, no. 6, pp. 1393-1399, June 1991

[Baur98] C. Baur, A. Bugacov, B. E. Koel, A. Madhukar, N. Montoya, T. R. Ramachandran, A. A. G. Requicha, R. Resch and P. Will: Nanoparticle Manipulation by Mechanical Pushing: Underlying Phenomena and Real-time Monitoring. *Nanotechnology*, vol. 9, pp. 360-364, 1998

[Besocke87] K. Besocke: An Easily Operable Scanning Tunneling Microscope. *Surface Science*, vol. 181, pp. 145-153, 1997

[Betzig92] E. Betzig, P. L. Finn and J. S. Weiner: Combined Shear Force and Near-Field Scanning Optical Microscopy. *Applied Physics Letters*, vol. 60, no. 20, pp. 2484-2486, May 1992

[Binnig82] G. Binnig, H. Rohrer, Ch. Gerber and E. Weibel: Surface Studies by Scanning Tunneling Microscopy. *Physical Review Letter*, vol. 49, no. 1, pp. 57-61, July 1982

[Binnig86] G. Binnig and C. F. Quate: Atomic Force Microscope. *Physical Review Letters*, vol. 56, no. 9, pp. 930-933, March 1986

[Block92] S. M. Block: Making Light Work with Optical Tweezers. *Nature*, vol. 360, pp. 493-495, Dec. 1992

[Brandstein95] M. S. Brandstein, J. E. Adcock and H. F. Silverman: A Practical Time-Delay Estimator for Localizing Speech Sources with a Microphone Array. *Computer Speeck and Language*, vol. 9, pp. 153-169, 1995

[Brown86] K. T. Brown and D. G. Flaming: *Advanced Micropipette Techniques for Cell Physiology*. John Wiley & Sons, New York, 1986

[Brunner97] R. Brunner, A. Bietsch, O. Hollricher and O. Marti: Distance Control in Near-Field Optical Microscopy with Piezoelectrical Shear-Force Detection Suitable for Imaging in Liquids. *Review of Scientific Instruments*, vol. 68, no. 4, pp. 1769-1772, April 1997

[Brunner98] M. Brunner and A. Stemmer: Design and Control of a Sensor-Guided Nanorobot. *The Fourth International Conference on Motion and Vibration Control MOVIC*, vol. 3, pp. 1157-1162, Zurich, Switzerland, Aug. 1998

[Büchi95] R. Büchi, W. Zesch, A. Codourey and R. Siegwart: Inertial Drives for Micro- and Nanorobots: Analytical Study. *SPIE Microrobotics and Micromechanical Systems*, vol. 2593, pp. 89-97, Philadelphia, Pennsyslavnia, Oct. 1995

[Bugacov99] A. Bugacov, R. Resch, C. Baur, N. Montoya, K. Woronowicz, A. Papson, B. E. Koel, A. A. G. Requicha and P. Will: Measuring the Tip-Sample Separation in Liquid Dynamic Force Microscopy. *Probe Microscopy*, in press, 1999

[Burnham97] N. A. Burnham, O. P. Behrend, F. Oulevey, G. Gremaud, P.-J. Gallo, D. Gourdon, E. Dupas, A. J. Kulik, H. M. Pollock and G. A. D. Briggs: How Does a Tip Tap? *Nanotechnolgy*, vol. 8, pp. 67-75, 1997

[Canny86] J. Canny: A Computational Approach to Edge Detection. *IEEE Transactions on Pattern Analysis and Machine Intelligence*, vol. PAMI-8, no. 6, pp. 679-698, Nov. 1986

[Castleman96] K. R. Castleman: *Digital Image Processing*. Prentice Hall, New Jersey, 1996

[Chen92] C. J. Chen: Electromechanical Deflections of Piezoelectric Tubes with Quartered Electrodes. *Applied Physical Letters*, vol. 60, no. 1, pp. 132-134, 1992

[Chen94] J. Chen, R. K. Workman, D. Sarid and R. Höper: Numerical Simulations of a Scanning Force Microscope with a

Large-Amplitude Vibrating Cantilever. *Nanotechnology*, vol. 5, pp. 199-204, 1994

[Colton98] R. J. Colton, A. Engel, J. E. Frommer, H. E. Gaub, A. A. Gewirth, R. Guckenberger, J. Rabe, W. M. Heckl and B. Parkinson: *Procedures in Scanning Probe Microscopies*. John Wiley & Sons, Chichester, 1998

[Craig89] J. J. Craig: *Introduction to Robotics, Mechanics and Control*. Addison-Wesley Publishing Company, Reading MA, Second Edition, 1989

[Danuser97] G. Danuser: *Quantitative Stereo Vision for the Stereo Light Microscope: An Attempt to Provide Control Feedback for a Nanorobot System*. Diss. ETH no. 12191, April 1997

[Danuser00] G. Danuser, P. T. Tran and E. D. Salmon: Tracking Differential Interference Contrast Diffraction Line Images with Nanometre Sensitivity. *Journal of Microscopy*, vol. 198, pt. 1, pp. 34-53, April 2000

[Drexler91] K. E. Drexler and C. Peterson, with G. Pergamit: *Unbounding the Future, The Nanotechnology Revolution*. William Morrow and Company, Inc., New York, 1991

[Dubbel90] W. Beitz and K.-H. Küttner: *Dubbel, Taschenbuch für den Maschinenbau*. Springer-Verlag, Berlin, 17. Auflage, 1990

[Duda72] R. O. Duda and P. E. Hart: Use of the Hough Transformation To Detect Lines and Curves in Pictures. *Graphics and Image Processing*, vol. 15, no. 1, pp. 11-15, Jan. 1972

[Faugeras93] O. Faugeras: *Three-Dimensional Computer Vision: A Geometric Viewpoint*. The MIT Press, Cambridge, Massachusetts, 1993

[Fearing95] R. S. Fearing: Survey of Sticking Effects for Micro Parts Handling. *IEEE/RSJ Conference on Intelligent Robots and Systems*, vol. 2, pp. 212-217, Pittsburgh, Aug. 1995

[Feynman59] R. P. Feynman: There's Plenty of Room at the Bottom. *Transcipt of talk given at the American Physical Society*, http://www.zyvex.com/nanotech/feynman.html, 1959

[Ge97] P. Ge and M. Jouaneh: Generalized Preisach Model for Hysteresis Nonlinearity of Piezoceramic Actuators. *Precision Engineering*, vol. 20, no. 2, pp. 99-111, 1997

[Geering90] H. P. Geering: *Mess- und Regeltechnik, Mathematische Grundlagen, Entwurfsmethoden, Beispiele.* Springer-Verlag, Berlin, 2. Auflage, 1990

[Gerig96] G. Gerig und O. Kübler: *Bilddatenanalyse und Computer Vision I.* Skript zur Vorlesung and der ETH Zürich, Institut für Kommunikationstechnik, Fachgruppe Bildwissenschaft, Okt. 1996

[Gheber98] L. A. Gheber, J. Hwang and M. Edidin: Design and Optimization of a Near-Field Scanning Optical Microscope for Imaging Biological Samples in Liquid. *Applied Optics*, vol. 37, no. 16, pp. 3574-3581, June 1998

[Gonzales93] R. C. Gonzales and R. E. Woods: *Digital Image Processing*. Addison-Wesley Publishing Company, Reading MA, 1993

[Greitmann96] G. Greitmann and R. A. Buser: Tactile Microgripper for Automated Handling of Microparts. *Sensors and Actuators*, vol. 53, pp. 410-415, 1996

[Hansma94] P. K. Hansma, B. Drake, D. Grigg, C. B. Prater, F. Yashar, G. Gurley, V. Elings, S. Feinstein and R. Lal: A New, Optical-Lever Based Atomic Force Microscope. *Journal of Applied Physics*, vol. 76, no. 2, pp. 796-799, July 1994

[Hartmann96] E. Hartmann, M. Enachescu, P. Radojkovic, M. Schwartzkopff: Imaging and Manipulation Properties of Nanoparticles in Scanning Tunneling Microscopy. *Nanotechnology*, vol. 7, pp. 376-380, 1996

[Hecht90] E. Hecht: *Optics*. Addison-Wesley Publishing Company, Reading MA, Second Edition, 1990

[Higuchi90] T. Higuchi, Y. Yamagata, K. Furutani and K. Kudoh: Precise Positioning Mechanism Utilizing Rapid Deformations of Piezoelectric Elements. *Proceedings of the IEEE Conference on Micro Electro Mechanical Systems*, pp. 222-226, Napa Valley, California, Feb. 1990

[Hollricher98] O. Hollricher, R. Brunner and O. Marti: Piezoelectrical Shear-Force Distance Control in Near-Field Optical Microscopy for Biological Applications. *Ultramicroscopy*, vol. 71, pp. 143-147, 1998

[Hsu95] J. W. P. Hsu, M. Lee and B. S. Deaver: A Nonoptical Tip-Sample Distance Control Method for Near-Field Scanning Optical Microscopy Using Impedance Changes in an Electromechanical System. *Review of Scientific Instruments*, vol. 66, no. 5, pp. 3177-3181, May 1995

[Hsu97] J. W. P. Hsu, A. A. McDaniel and H. D. Hallen: A Shear-Force Feedback Control System for Near-Field Scanning Optical Microscopes without Lock-In Detection. *Review of Scientific Instruments*, vol. 68, no. 8, pp. 3093-3095, Aug. 1997

[Hughes97] D. Hughes and J. T. Wen: Preisach Modeling of Piezoceramic and Shape Memory Alloy Hysteresis. *Smart Materials and Structures*, vol. 6, pp. 287-300, 1997

[Illingworth88] J. Illingworth and J. Kittler: A Survey of the Hough Transform. *Computer Vision, Graphics, and Image Processing*, vol. 44, pp. 87-116, 1988

[Inoué97] S. Inoué and K. R. Spring: *Video Microscopy, The Fundamentals*. Plenum Press, New York, 1997

[Israelachvili92] J. N. Israelachvili: *Intermolecular and Surface Forces*. Academic Press, London, Second Edition, 1992

[Jacobs97] H. O. Jacobs, H. F. Knapp, S. Müller and A. Stemmer: Surface Potential Mapping: A Qualitative Material contrast In SPM. *Ultramicroscopy*, vol. 69, pp. 39-49, 1997

[Jacobs98] H. O. Jacobs, H. F. Knapp and A. Stemmer: Practical Aspects of Kelvin Probe Force Microscopy. *Review of Scientific Instruments*, vol. 70, no. 3, pp. 1756-1760, 1998

[Jacobs99] H. O. Jacobs and A. Stemmer: Measuring and Modifying the Electric Surface Potential Distribution on a Nanometre Scale: a Powerful Tool in Science and Technology. *Surface and Interface Analysis*, vol. 27, pp. 361-367, 1999

[Jung96] T. A. Jung, R. R. Schlittler, J. K. Gimzewski, H. Tang and C. Joachim: Controlled Room-Temperature Positioning of Individual Molecules: Molecular Flexure and Motion. *Science*, vol. 271, pp. 181-184, Jan. 1996

[Junno95] T. Junno, K. Deppert, L. Montelius and L. Samuelson: Controlled Manipulation of Nanoparticles with an Atomic Force Microscope. *Applied Physical Letters*, vol. 66, no. 26, pp. 3627-3629, June 1995

[Karrai95] K. Karrai and R. D. Grober: Piezoelectric Tip-Sample Distance Control for Near-Field Optical Microscopes. *Applied Physical Letters*, vol. 66, no. 14, pp. 1842-1844, April 1995

[Kasaya98] T. Kasaya, H. Miyazaki, S. Saito and T. Sato: Micro Object Handling under SEM by Vision-based Automatic Control. *SPIE Conference on Microrobotics and Micromanipulation*, vol. 3519, pp. 181-192, Boston, Massachusetts, Nov. 1998

[Kim99] Ph. Kim and Ch. M. Lieber: Nanotube Nanotweezer. *Science*, vol. 286, pp. 2148-2150, Dec. 1999

[Knapp95] H. F. Knapp, W. Wiesgräbe, M. Heim, R. Eschricht and R. Guckenberger: Atomic Force Microscope Measurements and Manipulation of Langmuir-Blodgett Films with Modified Tips. *Biophysical Journal*, vol. 69, pp 708-715, Aug. 1995

[Knapp98a] H. F. Knapp, A. Tami, M. Brunner and A. Stemmer: Hydrophobic Surface Coatings on Tools Used for Handling of Micro-Particles. *The Fourth International Conference on Motion and Vibration Control MOVIC*, vol. 3, pp. 1151-1156, Zurich, Switzerland, Aug. 1998

[Knapp98b] H. F. Knapp, R. Guckenberger and A. Stemmer: AFM Imaging of Biological Samples Using Hydrophobic Tips. *Probe Microscopy*, vol. 1, pp. 247-257, 1998

[Knapp99] H. F. Knapp and A. Stemmer: Preparation, Comparison and Performance of Hydrophobic AFM Tips. *Surface and Interface Analysis*, vol. 27, pp. 324-331, 1999

[Koyano96] K. Koyano and T. Sato: Micro Object Handling System with Concentrated Visual Fields and New Handling Skills. *Proceeding of SPIE*, vol. 2906, pp. 130-140, 1996

[Kraus91] N. Kraus: *Kalibrierung von Piezo-Stellgliedern für die Rastersondenmikroskopie.* Bericht des Forschungszentrums Jülich, vol. 2483, 1991

[Kuo74] B. C. Kuo: *Theory and Applications of Step Motors.* West Publishing Co., St. Paul, 1974

[Kuo79] B. C. Kuo: *Step Motors and Control Systems.* SRL Publishing Company, Champaign, Illinois, USA, 1979

[Lippitz99] M. Lippith, M. Schüttler, H. Giessen, M. Born and W. W. Rühle: Bandwidth Enhancement of a Shear-Force-Controlled Distance Regulation in Near-Field Microscopy. *Journal of Applied Physics*, vol. 86, no. 1, pp. 100-106, July 1999

[Mayergoyz91] I. D. Mayergoyz: *Mathematical Models of Hysteresis.* Springer-Verlag, New York, 1991

[Menold99] P. H. Menold, R. K. Person and F. Allgöwer: Online Outlier Detection and Removal. *Proceedings of the 7th Mediterranean Conference on Control and Automation MED 99*, pp. 1110-1113, Haifa, Israel, 1999

[Miyazaki97] H. Miyazaki and T. Sato: Mechanical Assembly of Three-Dimensional Microstructures from Fine Particles. *Advanced Robotics*, vol. 11, no. 2, pp. 169-185, 1997

[Morari89] M. Morari and E. Zafiriou: *Robust Process Control.* Prentice Hall, Englewood Cliffs, New Jersey, 1989

[Mosher92] R. A. Mosher, D. A. Saville and W. Thormann: *The Dynamics of Electrophoresis.* VCH Verlagsgesellschaft mbH, Weinheim, Germany, 1992

[Nalwa86] V. S. Nalwa and Th. O. Binford: On Detecting Edges. *IEEE Transactions on Pattern Analysis and Machine Intelligence*, vol. PAMI-8, no. 6, pp. 699-714, Nov. 1986

[Nicoud95] J.-D. Nicoud: Microengineering: when is small too small? Nanoengineering: when is large too large? *Proceeding of*

*the Sixth Intern. Symposium on Micro Machines and Human Science*, Nagoya Municipal Industrial Research Institute, pp. 1-6, 1995

[Oldenburg96] R. Oldenburg, S. Inoué, R. Tiberio, A. Stemmer, G. Mei and M. Skvarla: Standard Test Targets for High-Resolution Light Microscopy. *Nanofabrication and biosystems: integrating materials science, engineering and biology*, pp. 123-138, Cambridge University Press, New-York, 1996

[Pearson98] R. K. Person: The Hampel Filter: A Nonlinear Data-Cleaner. in press, 1998

[Pohl78] H. A. Pohl: *Dielectrophoresis, The Behavior of Neutral Natter in Nonuniform Electric Fields*. Cambridge University Press, Cambridge, 1978

[Pohl88] D. W. Pohl and R. Möller: Tracking Tunneling Microscopy. *Review of Scientific Instruments*, vol. 59, no. 6, pp. 840-842, June 1988

[Prautzsch88] F. Prautzsch: *Schrittmotor-Antriebe.* Franzis-Verlag GmbH, München, 1988

[Preisach35] F. Preisach: Ueber die magnetische Nachwirkung. *Z. Phys.*, vol. 94, pp. 227-302, 1935

[Requicha99] A. A. G. Requicha: Nanorobotics. Ed. Handbook of Industrial Robotics, John Wiley & Sons, New York, 2nd Ed., pp. 199-210, 1999

[Resch99] R. Resch, D. Lewis, S. Meltzer, B. E. Koel, A. Madhukar, A. A. G. Requicha and P. Will: Manipulation of Gold Nanoparticles in Liquid Environments Using Scanning Force Microscopy. *Ultramicroscopy*, in press, 1999

[Ritter96] G. X. Ritter and J. N. Wilson: *Handbook of Computer Vision Algorithms in Image Algebra.* CRC Press, New York, 1996

[Ruiter98] A. G. T. Ruiter, K. O. van der Werf, J. A. Veerman, M. F. Garcia-Parajo, W. H. J. Rensen and N. F. van Hulst: Tuning Fork Shear-Force Feedback. *Ultramicroscopy*, vol. 71, pp. 149-157, 1998

[Salim97] R. Salim, H. Wurmus, A. Harnisch and D. Hülsenberg: Microgrippers Created in Microstructurable Glass. *Microsystem Technologies*, vol. 4, pp. 32-34, 1997

[Saleh91] B. E. A. Saleh and M. C. Teich: *Fundamentials of Photonics*. John Wiley & Sons, Inc., New York, 1991

[Salvi98] J. Salvi, P. Chevassus, A. Mouflard, S. Davy, M. Spajer, D. Courjon, K. Hjort and L. Rosengren: Piezoelectric Shear Force Detection: A Geometry Avoiding Critical Tip/Tuning Fork Gluing. *Review of Scientific Instruments*, vol. 69, no. 4, pp. 1744-1746, April 1998

[Segovia98] R. Segovia, S. Schweizer, P. Vischer and H. Bleuler: Contact Free Manipulation of MEMS-Devices with Aerodynamic Effects. *The Fourth International Conference on Motion and Vibration Control MOVIC*, vol. 3, pp. 1129-1132, Zurich, Switzerland, Aug. 1998

[Self83] S. A. Self: Focusing of Spherical Gaussian Beams. *Applied Optics*. vol. 22, no. 5, pp. 658-661, 1983

[Sheehan96] P. E. Sheehan and Ch. M. Lieber: Nanomachining, Manipulation and Fabrication by Force Microscopy. *Nanotechnology*, vol. 7, pp. 236-240, 1996

[Stemmer95] A. Stemmer: A Hybrid Scanning Force and Light Microscope for Surface Imaging and Three-Dimensional Optical Sectioning in Differenctial Interference Contrast. *Journal of Microscopy*, vol. 178, no. 1, pp. 28-36, April 1995

[Stemmer96] A. Stemmer, H. O. Jacobs and H. F. Knapp: Approaching the Nanoworld. SPIE *Proceedings on Microrobotics: Components and Applications*, vol. 2906, pp. 80-85, Boston, 1996

[Stemmer97] A. Stemmer and M. Brunner: Sensor-Guided Nanorobots. *SPIE Microrobotics and Microsystem Fabrication*, vol. 3202, pp. 222-227, Pittsburgh, Pennsylvania, Oct. 1997

[Stoer79] J. Stoer: *Einführung in die Numerische Mathematik*. Springer Verlag, Berlin, dritte Auflage, 1979

[Stroscio91] J. A. Stroscio and D. M. Eigler: Atomic and Molecular Manipulation with the Scanning Tunneling Microscope. *Science*, vol 254, pp. 1319-1326, Nov. 1991

[Vohnsen95] B. Vohnsen, S. Bozhevolnyi and R. Olesen: Study of Shear Force Technique for Near-Field Microscopy with an Uncoated Fiber Tip. *Ultramicroscopy*, vol. 61, pp. 207-213, 1995

[Wei98] P. K. Wei and W. S. Fann: Determination of the Shear Force Magnitude in Near-Field Scanning Optical Microscopy. *Ultramicroscopy*, vol. 71, pp. 159-163, 1998

[Zesch95] W. Zesch, R. Büchi, A. Codourey and R. Siegwart: Inertial Drives for Micro- and Nanorobots: Two Novel Mechanisms. *SPIE Conf. on Microrobots and Micromechanical Systems*, pp. 80-88, Philadelphia, USA, Oct. 1995

[Zesch97a] W. Zesch, M. Brunner and A. Weber: Vacuum Tool for Handling Microobjects with a Nanorobot. *Conference on Robotics and Automation ICRA*, pp. 1761-1766, Albuquerque, NM, USA, April 1997

[Zesch97b] W. Zesch: *Multi-Degree-of-Freedom Micropositioning Using Stepping Principles*. Diss. ETH no. 12318, 1997

[Zhong93] Q. Zhong, D. Inniss, K. Kjoller and V. B. Elings: Fractured Polymer Silica Fiber Surface Studied by Tapping Mode Atomic-Force Microscopy. *Surface Science*, vol. 290, no. 1-2, pp. 688-692, June 1993

# *Appendix*

On the following pages the circuit diagrams of the electronic components introduced in section 3.3 are presented.

**Fig. A.1:** *Schematic of signal processing of the 4-quadrant detector output (A, B, C, D). The circuit builds the differences between the left and the right half as well as the top and the bottom half of the detector and divides both results by the sum of all elements.*

**Fig. A.2:** *Circuit diagram of the lock-in amplifier. The signal ($U_{def}$) is first multiplied by the reference signal ($U_{ref}$) and then fed into a 4th order Bessel-type low pass filter.*

**Fig. A.3:** *Connection diagram of the RMS element and the PI controller. The RMS value of the input signal ($U_{def\,RMS}$) is built and transferred to the PI controller to generate the low-voltage z signal (LVZ).*

**Fig. A.4:** *Schematic of the high-voltage amplifier. The z offset ($Z_{offset}$) is added to the low-voltage signal ($X_{in}$) and is then amplified by a factor of 22 to apply it to the piezo tube.*

**Fig. A.5:** *Circuit diagram of the synthesizer running with a clock frequency of 32 MHz*

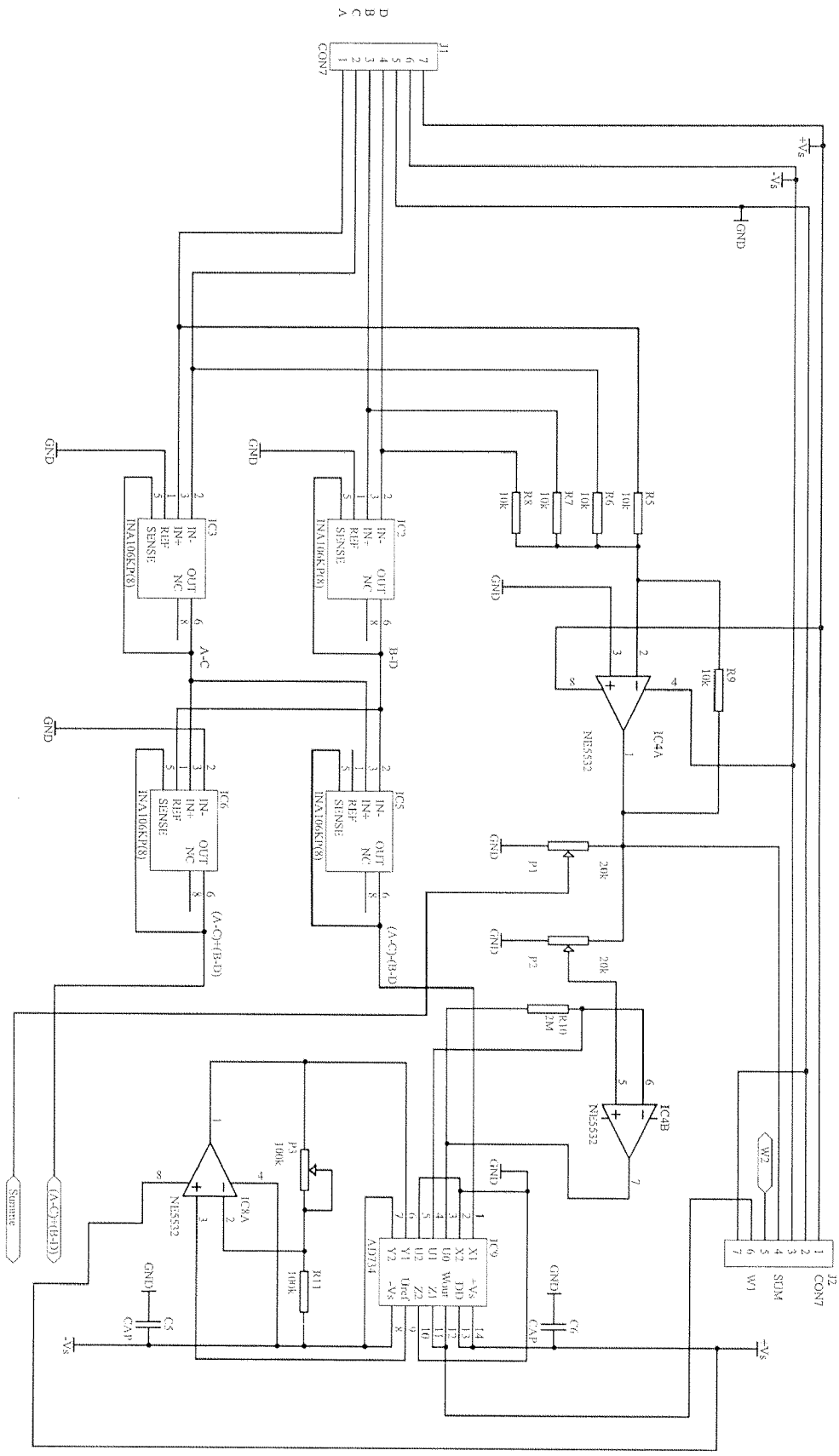
J1
CON7
D
B
C
A
+Vs
-Vs
GND
IC3
IC2
IC6
IC5
INA106KP(8)
IN-
IN+
REF
SENSE
OUT
NC
A-C
B-D
(A-C)+(B-D)
R5
R6
R7
R8
10k
R9
10k
IC4A
NE5532
P1
P2
20k
R10
2M
IC4B
IC8A
P3
100k
R11
100k
IC9
AD734
X1
X2
U0
U1
U2
Y1
Y2
Vref
Z1
Wout
Z2
C5
C6
CAP
W2
W1
SUM
J2
CON7
Summe

Fig. A.1:

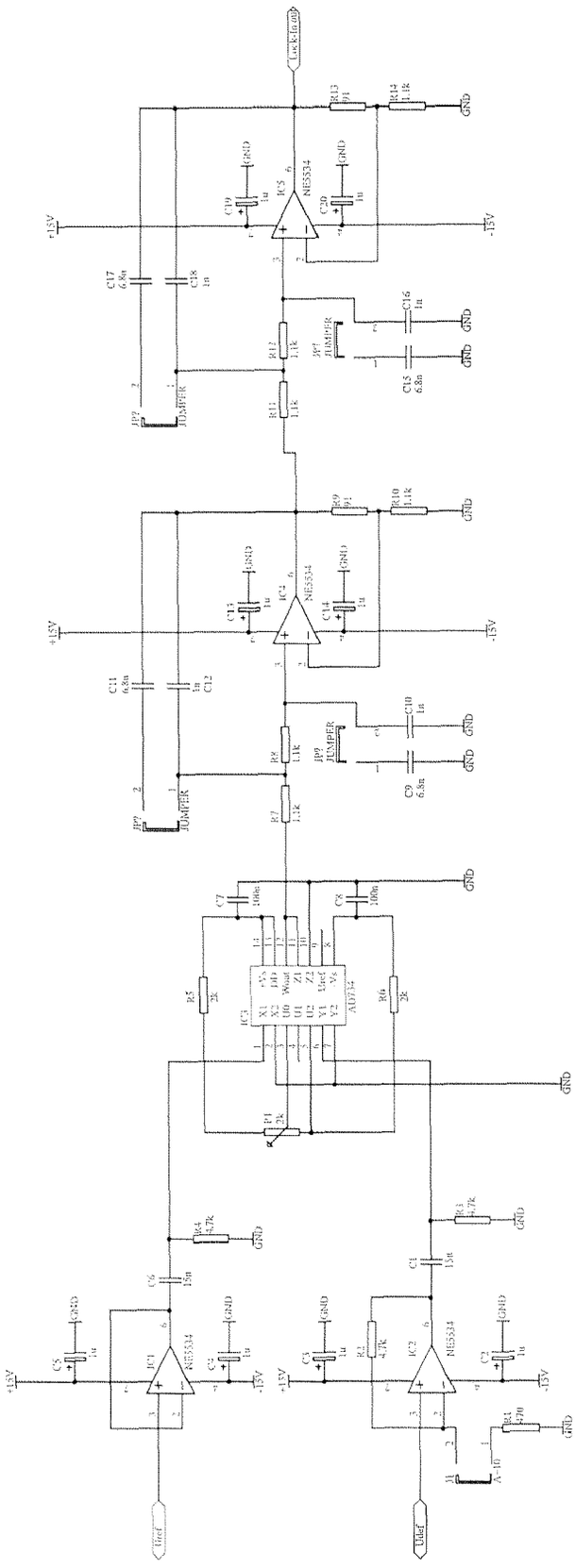

Fig. A.2:

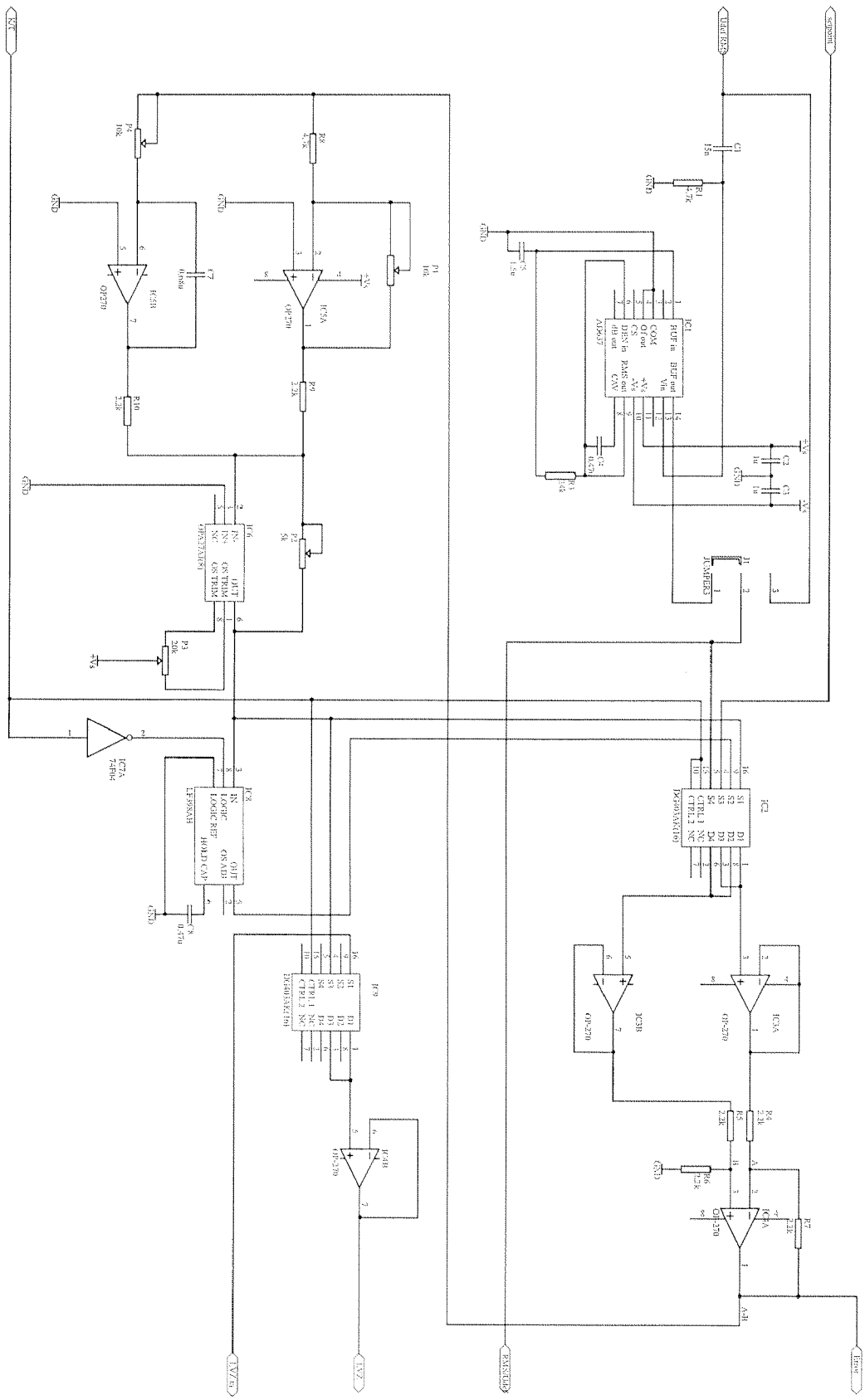

Fig. A.3:

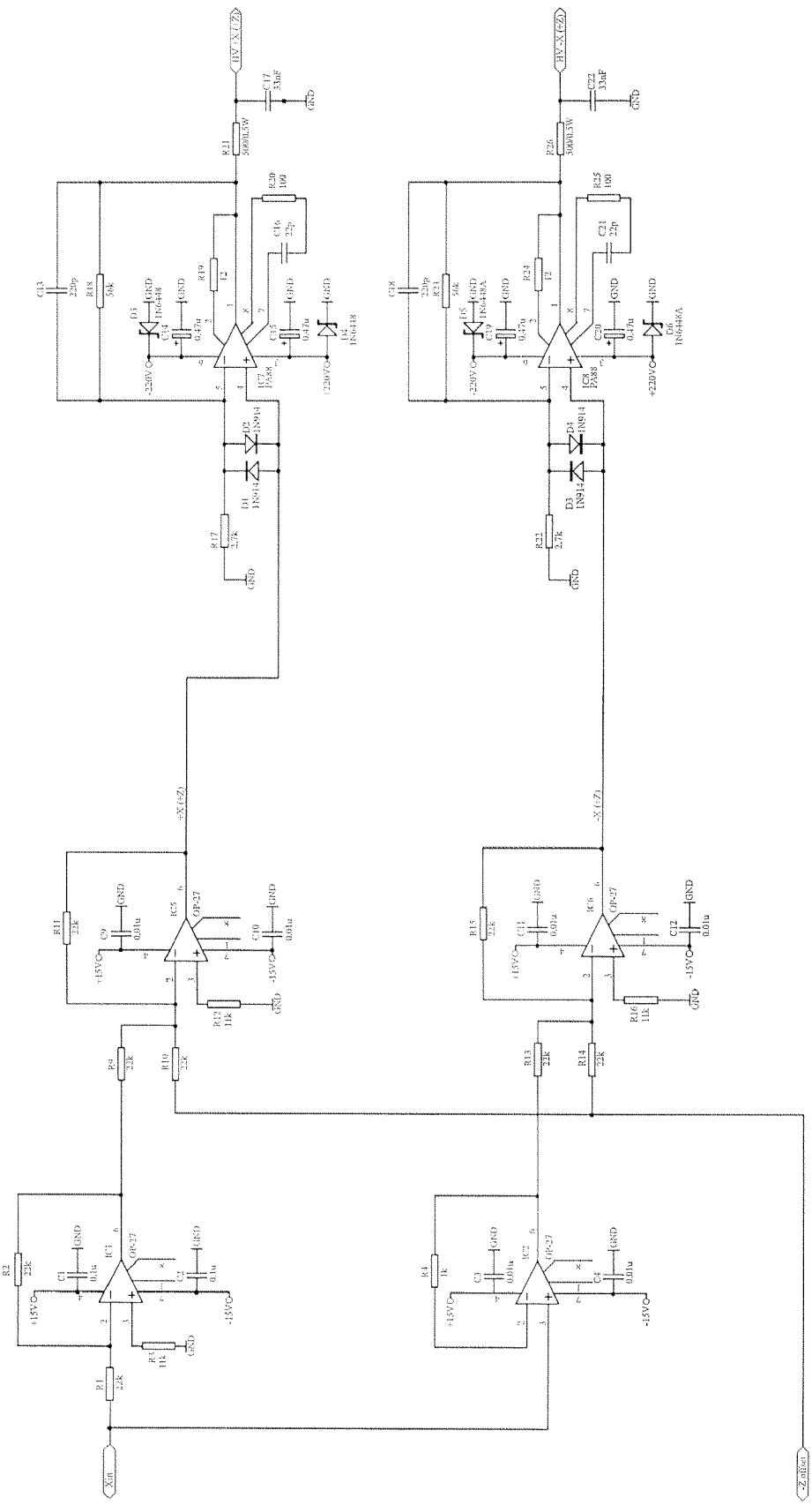

Fig. A.4:

Fig. A.5:

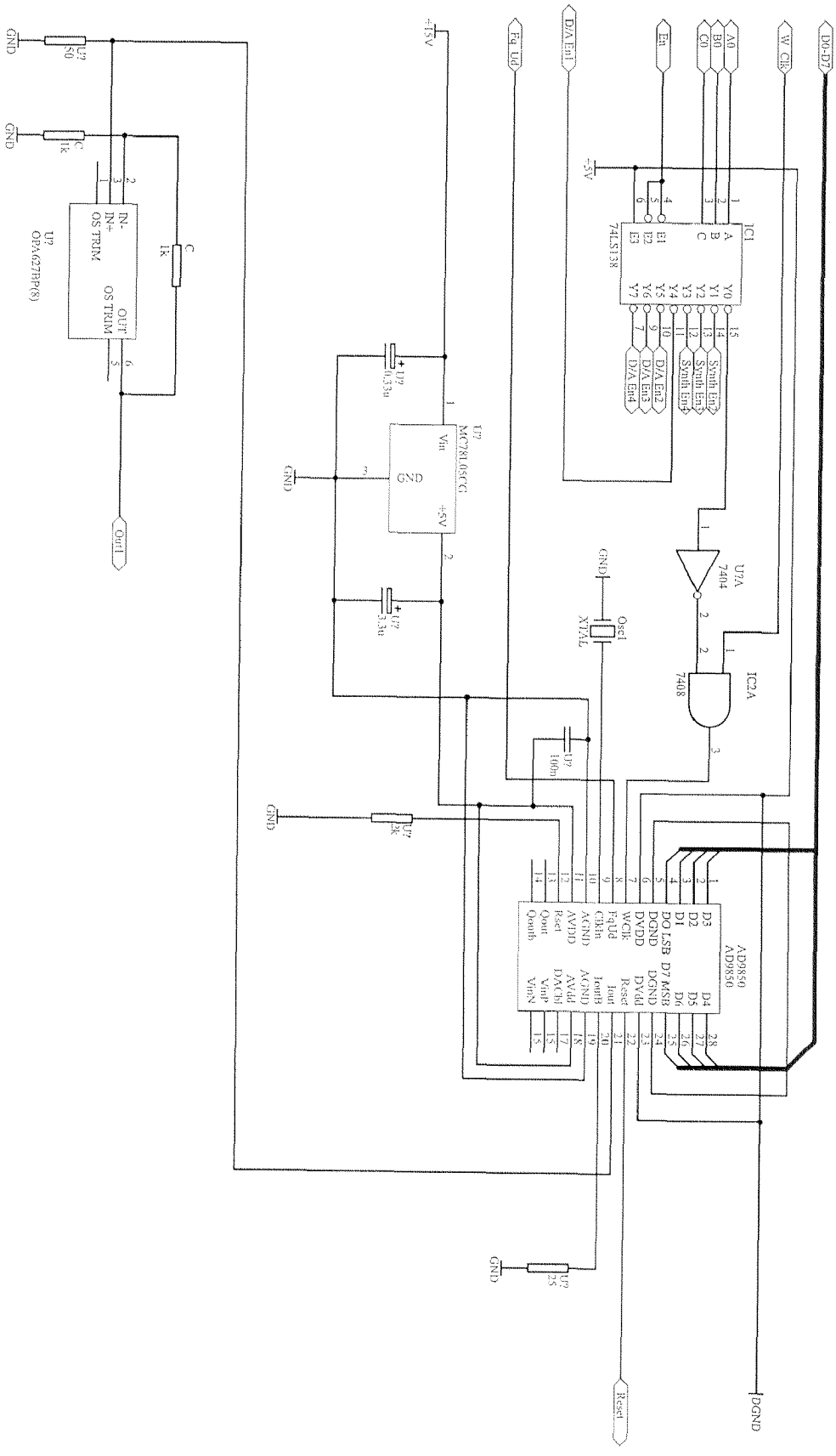
D0-D7
W Clk
A0
B0
C0
En
D/A En1
Fq Ud
+5V
GND
IC1
74LS138
Synth En2
Synth En3
Synth En4
D/A En2
D/A En3
D/A En4
U7A
7404
IC2A
7408
Osc1
XTAL
U7
100n
U7
2k
U7
25
U7
0.33u
U7
3.3u
U7
MC78L05CG
Vin
GND
+5V
U7
50
C
1k
U7
OPA627BP(8)
IN-
IN+
OS TRIM
OUT
Out1
AD9850
D3
D2
D1
D0 LSB
DGND
DVDD
WClk
FqUd
CIkIn
AGND
AVDD
Reset
Qout
Qbarb
D4
D5
D6
D7 MSB
DGND
DVdd
Reset
IoutB
AGND
AVdd
DACbl
VinP
VinN
Reset
DGND

# Curriculum Vitae

## Personal Data:

| | |
|---|---|
| Name: | Markus Brunner |
| Date of Birth: | 22nd of February, 1971 |
| Place of Origin: | Laupersdorf, Switzerland |
| Nationality: | Swiss |

## Education:

| | |
|---|---|
| 1978-1982 | Elementary School, Meltingen SO |
| 1983-1990 | High School (Gymnasium), Laufen BL<br>Degree: Matura Type B |
| 1991-1996 | Swiss Federal Institute of Technology (ETH), Zurich<br>Degree: Diploma in Mechanical Engineering<br>(Dipl. Masch.-Ing. ETH) |
| 1997-2000 | Nanotechnology Group, Institute of Robotics, ETH, Zurich<br>Ph.D. research and supervision of student projects in the field of nano science<br>Thesis advisors: Prof. Dr. A. Stemmer, ETH, Zurich and Prof. Dr. H. Bleuler, EPFL, Lausanne |

## Projects:

| | |
|---|---|
| Semester Project: | Modelling and Simulation of Precise Human Arm Movements |
| Student Project: | Participation in the Swiss SmartRob Championships of the Institute of Robotics, ETH, Zurich |
| Semester Project: | Feasibility Analysis and Design of an Airplane Wing Grid |
| Diploma Thesis: | Micro Vacuum Gripper for a Nanorobot |
| Ph.D. Thesis: | Design and Control of Sensor-Guided Nanorobots |

Seite Leer /
Blank leaf